Doctoral Thesis

Theory of phonons and thermal transport in moiré superlattices

Department of Physics, Osaka University

Lukas Primahatva Adhitya Krisna

2024

Abstract

In this thesis, we investigate the in-plane acoustic phonons and thermal transport properties in moiré superlattices, focusing on twisted bilayer systems. Moiré pattern holds an important role in the physical properties of van der Waals materials. A well-known example is twisted bilayer graphene (TBG), where the long-wavelength moiré potential modulates the original Dirac fermions of graphene and various correlated phases were observed due to the emergence of nearly flat bands at some specific twist angles. Novel electronic phenomena were also observed in other twisted bilayer materials, such as hexagonal boron nitride or twisted bilayer transition metal dichalcogenides (TMD).

The interlayer moiré potential in twisted bilayer systems also induces a structural change which is expected to strongly renormalize of the vibrational properties. In TBG, in-plane acoustic phonons were shown to be reconstructed into superlattice mini-bands with a notable flattening of some particular bands. These phonons behave as a vibration of the effective triangular structure of the moiré superlattice with a different mechanical characteristic to the original graphene honeycomb lattice. However, the moiré effect on the in-plane acoustic phonons of twisted bilayer materials beyond TBG was not understood. Furthermore, changes in the band structure of the acoustic phonons would have an immediate impact on the thermal transport properties, particularly at low temperature.

In the first part of this thesis, we investigate in-plane acoustic phonons in twisted bilayer systems beyond TBG, including twisted graphene / hexagonal boron nitride (t-G / hBN), and twisted bilayer molybdenum disulfide (t-MoS2) as a representative of TMD systems. We utilize the continuum approach, where the interlayer potential is a continuous function of the local stacking configurations which changes smoothly across the moiré superlattice unit cell. We show that there is a strong correspondence between the relaxed lattice structure and the phonon band structure which leads to the appearance of universal features across different twisted bilayer systems. To elucidate this correspondence, we develop

an effective mass-spring model that can perfectly reproduce the original phonon bands at low frequency. One particular characteristic of the band structures is the presence of multiple flat bands that can be understood as independent oscillations of a collection of isolated strings. Furthermore, we also show that the moiré phonons can also exhibit chiral properties for systems with no inversion symmetry in the moiré potential, such as t-G/hBN.

In the second part of this thesis, we calculate the thermal conductivity of twisted bilayer systems using the semi-classical transport equation. We focus on the low-temperature regime, where the mean free path of phonons is roughly constant, and the energy of the reconstructed phonons is the most relevant. We show that significant flattening of the phonon bands leads to a reduction in thermal conductivity for up to 40% at a particular temperature. Furthermore, we show that these changes are also manifested in the temperature dependence of the thermal conductivity, where a characteristic deviation from the usual T^2 of in-plane acoustic phonons is found for every twisted bilayer system with a notable moiré effect.

Our results hold an important role in the study of moiré materials. We expect that the electron-phonon interactions are enhanced by the moiré effect, which could help explain the mechanism behind various transport phenomena observed in twisted bilayer systems. The flat phonon bands are also expected to entail novel physics, such as localized excitations that was previously realized in photonic lattices. Lastly, the characteristic changes in thermal conductivity should be useful for the definitive verification of the presence of moiré phonons as well as for the future of thermal device engineering.

Table of Contents

Chapter 1

Introduction

1.1 Purpose of study

In recent years, two-dimensional (2D) moiré materials have attracted significant research interest. The most well-known example is twisted bilayer graphene (TBG), where a relative twist angle θ between two stacked graphene layers introduces a lattice mismatch and creates an interference pattern, i.e., the moiré pattern. In small-θ TBG, the emerged long-periodic moiré superlattice modulates the graphene's Dirac electrons into an effective superlattice mini bands [1, 2, 3, 4, 5, 6, 7, 8, 9, 10, 11, 12, 13], which become nearly flat for $\theta \sim 1°$, also known as the magic angle. This leads to the observation of various strong correlated phenomena in magic angle TBG, such as superconductivity and correlated insulators [14, 15]. The study of moiré superlattice have also been extended to other van der Waals multilayers involving hexagonal boron nitride (hBN) [16, 17, 18, 19, 20, 21, 22, 23, 24, 25, 26, 27, 28] and transition metal dichalcogenides (TMD) [29, 30, 31, 32, 33, 34, 35, 36, 37], where various exotic phenomena were also observed.

Moiré effect does not only influence the electronic properties but also the phonons. The phonon bands of the monolayer are folded into the mini superlattice Brillouin zone, which then used to characterize the twist angle assuming that phonon dispersion are largely unchanged by the interlayer potential [38, 39, 40, 41, 42, 43]. However, when the moiré period is much larger than the atomic scale, spontaneous relaxation gives significant lattice deformation that leads to a strong renormalization of lattice vibrations as various features emerge at the moiré scale

[44, 45, 46, 47, 48, 49, 50, 51, 52, 53, 54]. In small-θ TBG, for example, the in-plane acoustic phonons of graphene are reconstructed into a group of superlattice mini bands separated by spectral gaps with a notable flattening of some particular bands [45, 55, 56]. These reconstructed bands are represented as oscillations of an effective triangular structure of relaxed TBG moiré superlattice. Despite these results, little is known about the description of phonons in moiré superlattices beyond TBG, particularly, on the relation to the effective relaxed lattice structure.

In this thesis, we aim to investigate the effect of moiré pattern in the phonon properties of twisted bilayer systems, which includes twisted graphene/hexagonal boron nitride (t-G/hBN) as the first example of hetero bilayers, and twisted bilayer molybdenum disulfide (t-MoS_2) as a representative of TMD systems. We focus specifically on the hybridization of in-plane acoustic modes of the monoalayers, where siginificant moiré effect was previously demonsrated in the case of TBG [45, 46]. Here, we show that the reconstructed phonon bands converges towards a particular structure at low-θ limit, that is strongly related to the geometry of the relaxed state of the given system. To demonstrate this relation, we develop an effective mass-bond model to reproduce the original band structure and elucidate the origin of notable features, such as flat phonon bands, that are universally found across different systems. We also show that the reconstructed phonon modes in graphene/hBN can also exhibit chirality due to the absence of inversion symmetry in the moiré potential [55]. We further calculate the thermal conductivity to demonstrate the moiré effect in the thermal transport properties. We show that the flattening of the low-energy phonons bands leads to a significant suppression of thermal conductivity up to 40%, resulting in a characteristic deviation from the generic quadratic temperature dependence of thermal conductivity in two-dimensional system.

This thesis is organized as follows. For the rest of this chapter, we briefly review previous works on graphene and 2D moiré materials, lattice relaxation, and phonon properties. In Chapter 2, we provide a theoretical basis for perform-

ing lattice relaxation and for describing phonons in a variety of twisted bilayer systems. In Chapter 3, we discuss the calculated phonon modes and elucidate the special features introduced by the moiré effects. In Chapter 4, we explore the observable properties of the moiré effect on phonons in terms of thermal transport by calculating the thermal conductivity at the low-temperature regime. Finally, this thesis is concluded in Chapter 5.

1.2 Graphene and 2D materials

Graphene is a one-atom-thick material that is composed of carbon atoms arranged in a two-dimensional honeycomb lattice [Fig. 1.1 (a)]. Naturally, graphene can be abundantly found as a single layer component of graphite, which is the same material that is commonly found as pencil leads. In graphite, a large number of graphene layers are stacked and held together by the van der Waals force, which is significantly weaker than the in-plane chemical bonds between the carbon atoms. In fact, the most common way to obtain graphene is by the exfoliation method, i.e., repeatedly peeling a graphite flake using adhesive tapes [57]. Interestingly, graphene has significantly different physical properties compared to graphite. One of them is that charge carriers in graphene behave as massless Dirac fermions that travel with around 1/300 of the light velocity. These are evident from the linear energy-momentum dispersion of the conduction and valence bands in the vicinity of K and K' points of the momentum space, where the two bands become degenerate [Fig. 1.1 (b)]. This unusual feature gives a variety of exceptional electronic properties, such as very high carrier mobility [57, 58, 59] and the observation of a integer quantum Hall effect at room temperature [60].

Since the graphene boom era in the 2010s, many other single-layered materials have become widely available. These include a variety of metals (e.g., $NbSe_2$), semiconductors (e.g., MoS_2), and insulators (e.g., hexagonal boron nitride (hBN)]. Each of these materials have notably different properties from their 3D counterparts. While the search for other atomically thick crystals is considered to be in

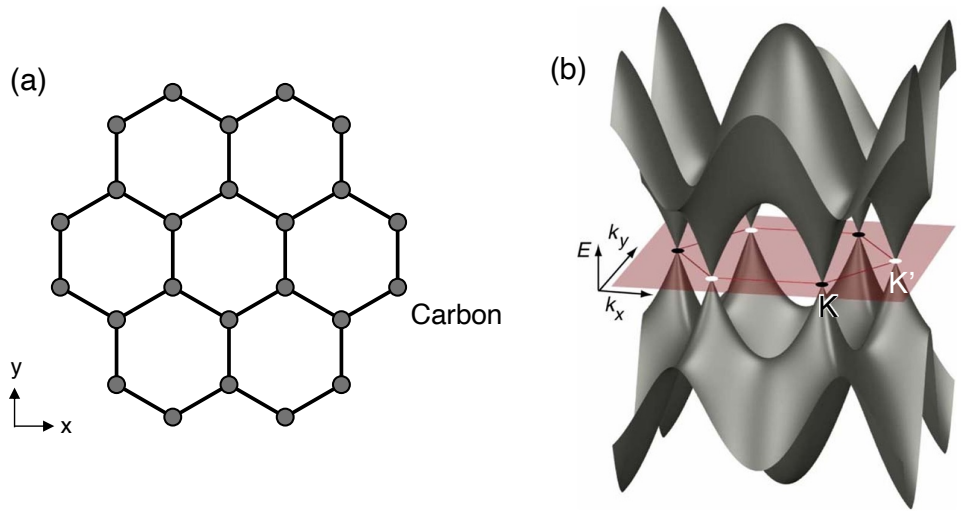

Figure 1.1: (a) Atomic structure of graphene. (b) The valence band and conduction band of graphene [61].

its maturity, a new path of exploration emerged: stacking different single-layered crystals in a similar way to building Lego blocks [Fig. 1.2 (a)] [62]. In this approach, each layer acts like a block with a particular function that is combined with other layers to produce a heterostructure with the desired property. For example, placing a transition metal dichalcogenides (TMD) close to graphene can greatly enhance the spin-orbit interaction in graphene, which would otherwise be negligibly small [63, 64, 65]. However, the importance of relative orientation between the constituent layers have been largely overlooked in the early study of van der Waals (vdW) heterostructures. It was later revealed that various properties are very sensitive to the relative rotation angle θ, and controlling θ would prove to be a crucial tool in the discovery of new physics in these systems [66]. The emergence of novel phenomena is intimately tied to a geometric pattern known as the moiré pattern, which appears when two or more overlapping periodic structures are misaligned. In vdW multilayers, these pattern generally exists when the stacked layers have different lattice constants [Fig. 1.2 (b)] or lattice orientations [Fig. 1.2 (c)]. In the following section, we take a closer look on how the moiré pattern influences the physical properties of layered materials.

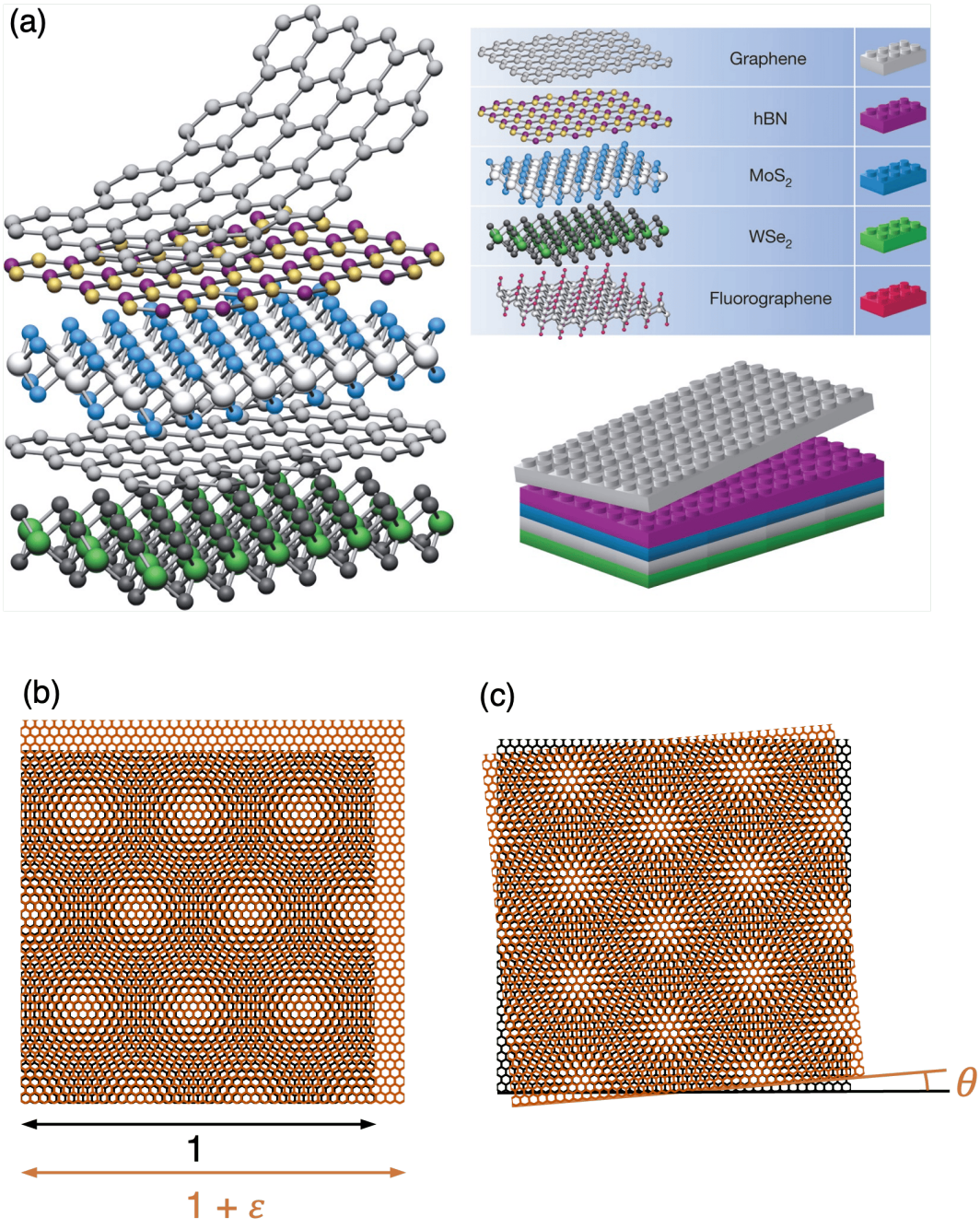

Figure 1.2: (a) Construction of van der Waals heterostructure from a variety of single-layered crystals that act like Lego blocks. Moiré pattern in bilayer system can appears due to (b) lattice constant mismatch, $\varepsilon = a'/a - 1$, where a and a' are the two lattice constans, or (c) relative twist angle θ.

1.3 Moiré superlattice in twisted bilayer graphene (TBG)

Twisted bilayer graphene (TBG), a rotationally-stacked pair of graphene, is the first and most studied example of two-dimensional materials with moiré pattern. Here, we begin with providing an overview on how the presence of long-periodic moiré pattern in TBG affects the electronic, mechanical, and phononic properties and leads to a variety of novel phenomena.

1.3.1 Electronic properties

When two graphene are stacked on top of each other with a relative twist angle θ, mismatch of the two lattices creates the moiré pattern. The moiré period is inversely proportional to $\sin(\theta/2)$, so it becomes much longer than the atomic scale when the twist angle is small. Here, the moiré pattern acts as a long-wavelength potential that significantly alters the electronic properties of TBG depending on the twist angle [1, 2, 3, 4, 5, 6, 7, 8, 9, 10, 11, 12, 13, 67]. Figure 1.3 (e) shows the electronic band structure of TBG at three different θ, calculated by a continuum approach [8]. One of the important features is the reduction of Fermi velocity that becomes nearly zero at some specific set of twist angles, which are also known as the magic angle. The emergence of nearly-flat bands at the charge neutrality point suggests the presence of a strong electron-electron interaction and a likely appearance of correlated phases. Indeed, transport measurement in magic-angle TBG reveals the existence of superconducting and correlated insulating states which occurs at different filing factors of the narrow bands [Fig. 1.3 (f)] [15, 14, 68, 69, 70]. On top of that, further studies observe the presence of other correlated phenomena, such as strange metallic behavior [71, 72, 73] and ferromagnetism [74, 75, 76]. These exceptional discoveries instigated intense research to elucidate the various correlated phenomena in TBG, as well as using it

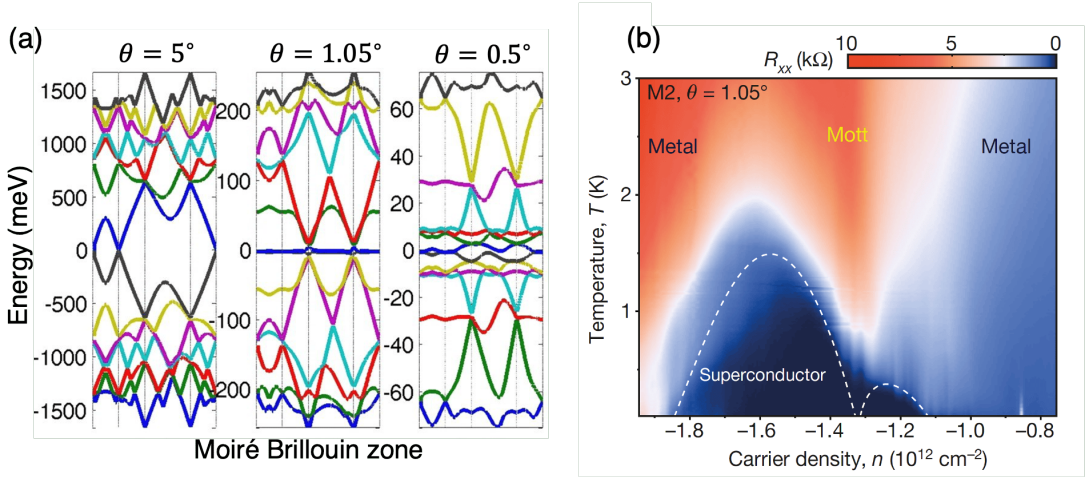

Figure 1.3: (a) Electronic band structure of TBG at three different twist angle [8]. (b) Phase diagram of magic-angle TBG [14].

as a platform to search for new physical properties.

1.3.2 Lattice relaxation

In the early theoretical studies of twisted bilayer graphene, scientists assume that the graphene remains rigid and undistorted when they are stacked together and twisted. This assumption was partly justifiable due to the immense in-plane mechanical strength of graphene [77] and the widely-used hBN substrate that is able to maintain the integrity of the two-dimensional structure of graphene [78]. However, as we will see below, significant lattice reconstruction occurs, particularly when the twist angle is small, and this has significant influence in the electronic properties.

In small-θ TBG, the local structure at a given position resembles a certain stacking configuration of the non-twisted bilayer graphene that changes continuously across a single moiré unit cell [Fig. 1.4 (a)]. Each stacking configuration corresponds to a different binding energy which then defines the landscape of interlayer interaction across the moiré superlattice [Fig. 1.4 (b)] [79, 80, 81, 82]. For instance, the lowest energy are given by the AB and BA stacking configurations where for AB (BA) the A (B) sublattice of the top layer is right above the

B (A) sublattice of the bottom layer, and the highest energy is given by the AA configurations where the two layers are perfectly aligned. When the moiré period is long, the energy gained by maximizing the area of AB/BA configurations becomes large enough to overcome the elastic energy cost required to locally distort the honeycomb lattices. As a result, the whole system spontaneously relaxes to form a large commensurate regions of AB/BA stacking structure separated by domain walls [79, 83, 84, 85, 86]. These AB/BA domain structures are well observed in various measurements of bilayer graphene in the experiments [Fig. 1.4 (c) and (d)] [87, 88, 89, 90].

Theoretically, the lattice relaxation in TBG has been studied through density functional theory (DFT) calculations [67], molecular dynamics [83, 84], and continuum model [91, 85]. Due to the large number of atoms within a single moiré unit cell, the usual atomistic calculations are computationally challenging, particularly for small-θ TBG. In such a case, continuum model is often utilized in which the relevant physics are assumed to be continuous and varying smoothly at the atomic scale. Figure 1.4 (e) show the relaxed structure of TBG at four different twist angle ranging from $\theta = 2.65^\circ$ to 0.547°, calculated using the continuum model [85]. Here, the enlargement of AB/BA stacking regions becomes more noticable at smaller twist angle and eventually forms an effective triangular domain pattern that follows the periodicity of the moiré superlattice.

The relaxation of the lattice structure also has a strong influence on the electronic bands of TBG [85, 92, 93, 94, 90]. Figure 1.4 (f) shows the electronic bands in both case of the relaxed (black line) and non-relaxed (red-dashed line) of TBG for $\theta = 2.65^\circ$ and 1.05° [85]. For the 1.05° case (around the magic angle), lattice relaxation isolates the group of narrow bands near the charge neutrality from the higher and lower bands with a gap of around 15 meV, as well as introduces an electron-hole asymmetry. In the real space, electronic states corresponding to the flat bands are highly localized within the constricted AA-stacking regions [95]. This, along with the topological characteristics of the bands, aids the devel-

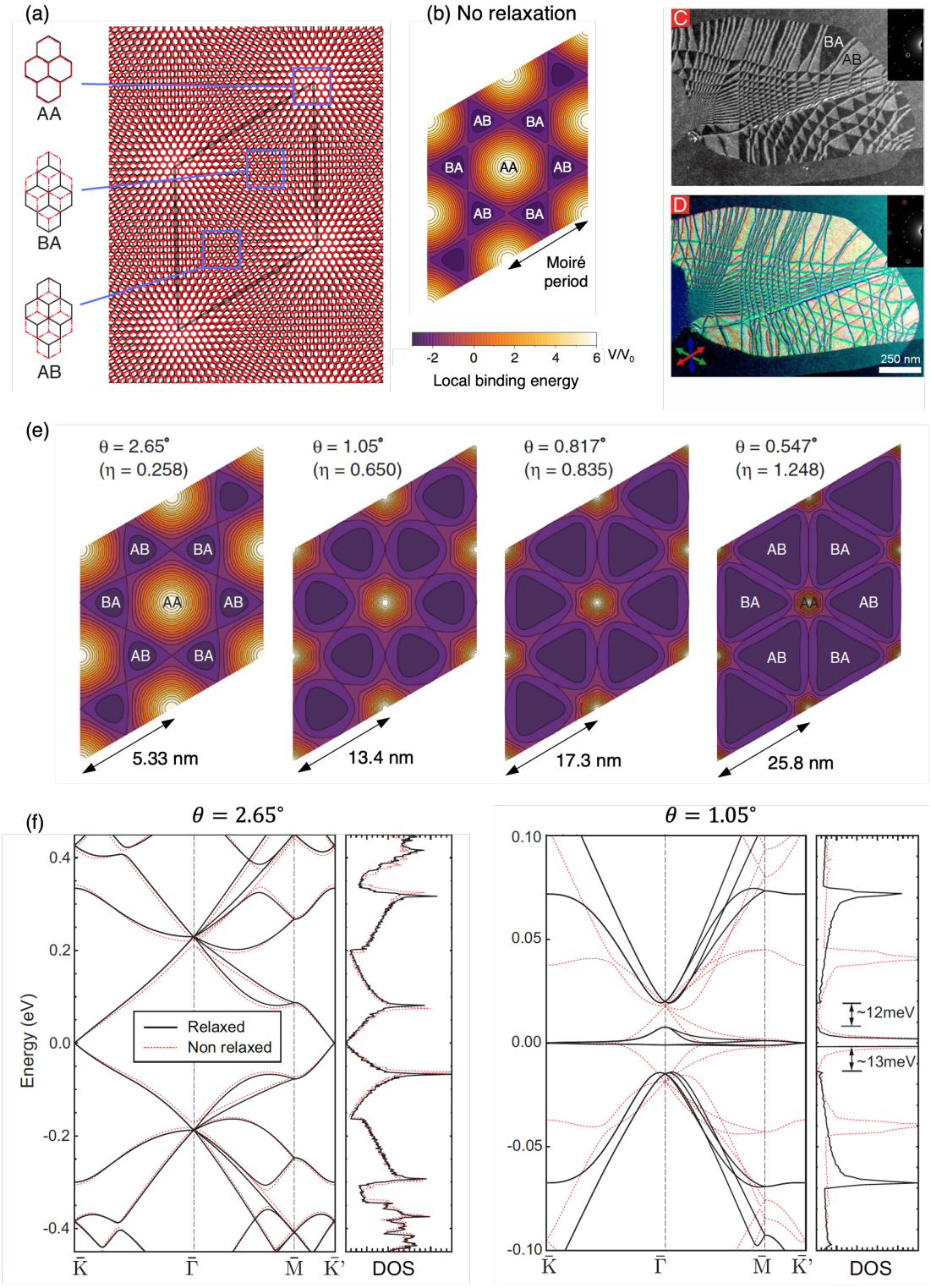

Figure 1.4: (a) Moiré pattern and the local AA, BA, and AB stacking structure. (b) Distribution of interlayer binding energy across moiré superlattice [85]. (c) and (d) Dark-field transmission electron microscopy images of bilayer graphene, showing the AB/BA domain formation and the domain walls [89]. (e) Local binding energy of TBG at various twist angles [85]. (f) Electronic band structure and density of states of relaxed (black lines) and non-relaxed (red-dashed lines) TBG for $\theta = 2.65°$ and $1.05°$ [85].

opment of simplified model to investigate the origin of the emergent correlated phases [93, 96, 97, 98, 99]. Meanwhile, the domain walls, which becomes clearly distinct at angle even lower than the magic angle, acts as a one-dimensional topological channels for electronic transport when the system is exposed by a transverse electric field [90, 100].

1.3.3 Phonon properties

The lattice reconstruction in TBG is expected to affect not only the electronic properties, but also the phonons. In graphene, the two atoms in its unit cell give rise to three acoustic phonon modes and three optical phonon modes. Due to the two-dimensional nature of graphene, each of the three modes are further classified as either in-plane or out-of-plane, based on the polarization of the atomic oscillations relative to the propagating direction. Figure 1.5 (a) shows the phonon dispersion of monolayer graphene, calculated by the force constant method [40]. At low-frequency, the two in-plane modes, longitudinal acoustic (LA) and transverse acoustic (TA) have linear dispersions while the out-of-plane flexural acoustic mode (ZA) is quadratic. The quadratic dispersion of the ZA phonons is a characteristic of two-dimensional system which is decoupled to the in-plane counter part within the harmonic approximation [101].

When two graphene are stacked to form AA or AB bilayer graphene, each of the phonon modes become hybridized into either interlayer symmetric (atoms on both layer move in parallel) or antisymmetric (move in opposite) [102, 103, 104, 105]. However, due to the weak van der Waals interaction between the layers, the two interlayer modes are generally nearly degenerate, except for the ZA phonons as the corresponding antisymmetric modes modulate the interlayer distance, as shown in Fig. 1.5(b) [102, 103, 104, 40]. The phonon dispersion of TBG with $\theta = 13.2^\circ$ is shown in Fig. 1.5(c), calculated using the force-constant method with Lennard-Jones function to capture the interlayer potential [40]. The folding effect of the original phonon bands of AA bilayer graphene is evident as numerous bands

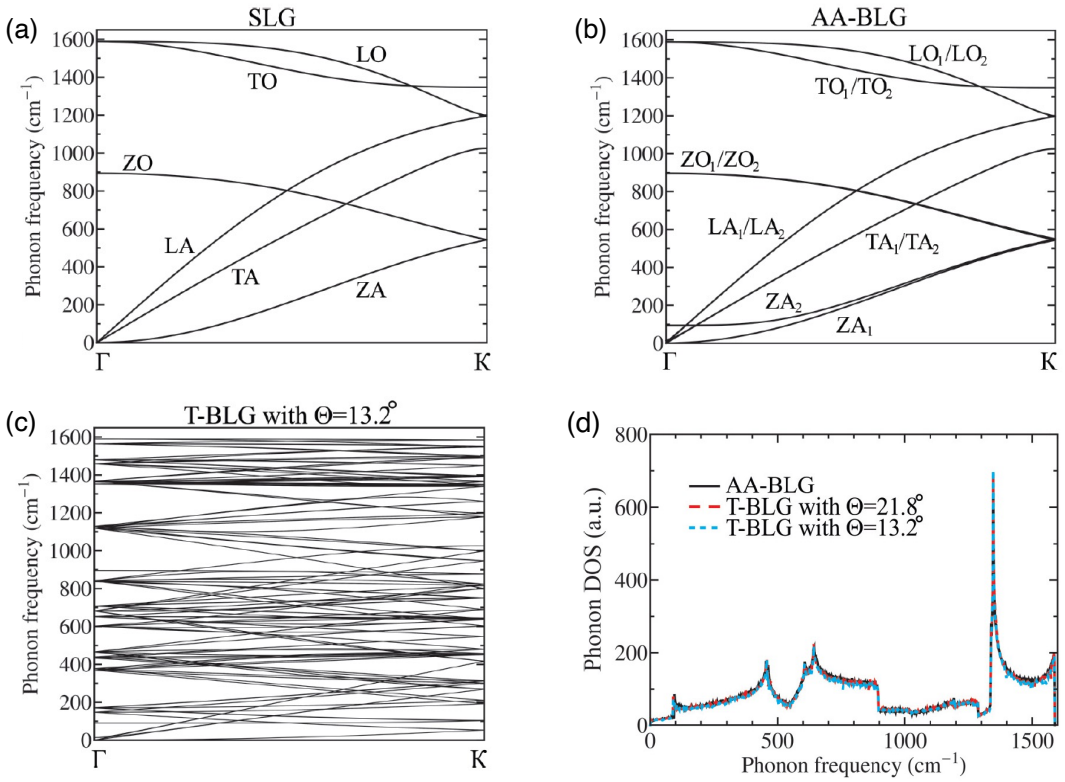

Figure 1.5: Phonon dispersions of (a) monolayer graphene, (b) AA-stacked bilayer graphene (AA-BLG), and (c) TBG with $\theta = 13.2°$. (d) Phonon density of states for AA-BLG and TBG with $\theta = 21.8°$ and $13.2°$. Figures are obtained from [40].

appear in the small superlattice Brillouin zone. However, the phonon density of states, as shown in Fig. 1.5 (d), remain mostly unchanged from those of AA/AB bilayer graphene and also independent of the twist angle [40]. Similar conclusions are obtained by other calculation methods, such as force-constant method with registry-dependent interlayer potential [41], molecular dynamics [38], and density functional theory [106], showing minimum frequency change by the interlayer potential. In fact, the lack of renormalization effect enables a relatively accurate determination of twist angle from Raman spectroscopy, since the frequency signal that is attributed to the folded phonons can be mapped directly to the phonon dispersion of the original non-twisted bilayer system [39, 42, 43].

The notable lattice relaxation at small twist angle, however, is expected to strongly affect the phonon properties. When the triangular domain structure become apparent, the lattice vibrations in TBG become localized within different regions of moiré superlattice [44, 45, 47, 49]. At low frequency, in particular, the in-plane acoustic phonons are reconstructed into superlattice mini bands with notable band gap and the flattening of some specific bands. This is clearly seen by comparing the phonon dispersion in the absence of interlayer coupling, i.e., empty-lattice folding of graphene's LA and TA phonons, [Fig.1.6(a)], that of 1.05° TBG [Fig.1.6(b)] [45]. In the real space, the superlattice phonon modes correspond to the oscillation of the domain walls that separate the AB/BA stacking regions [see Fig. 1.6 (e)]. In fact, these modes can be emulated by the mass and bond model [Fig. 1.6 (c)] which correspond to the squeezed AA stacking regions and the domain walls connecting them, respectively. In such model, the potential energy of the system is proportional to the length of the bonds, reminiscent of the one-dimensional soliton wall [46, 107]. The effective model manages to reproduce the phonon dispersion of the two lowest bands [Fig. 1.6 (d)] and the corresponding eigen modes [Fig. 1.6 (f)], as well as the convergence of the phonon velocities at low-θ limit which later verified by a fully analytic derivation [108].

Recently, the study of moiré phonons in TBG is extended to include the

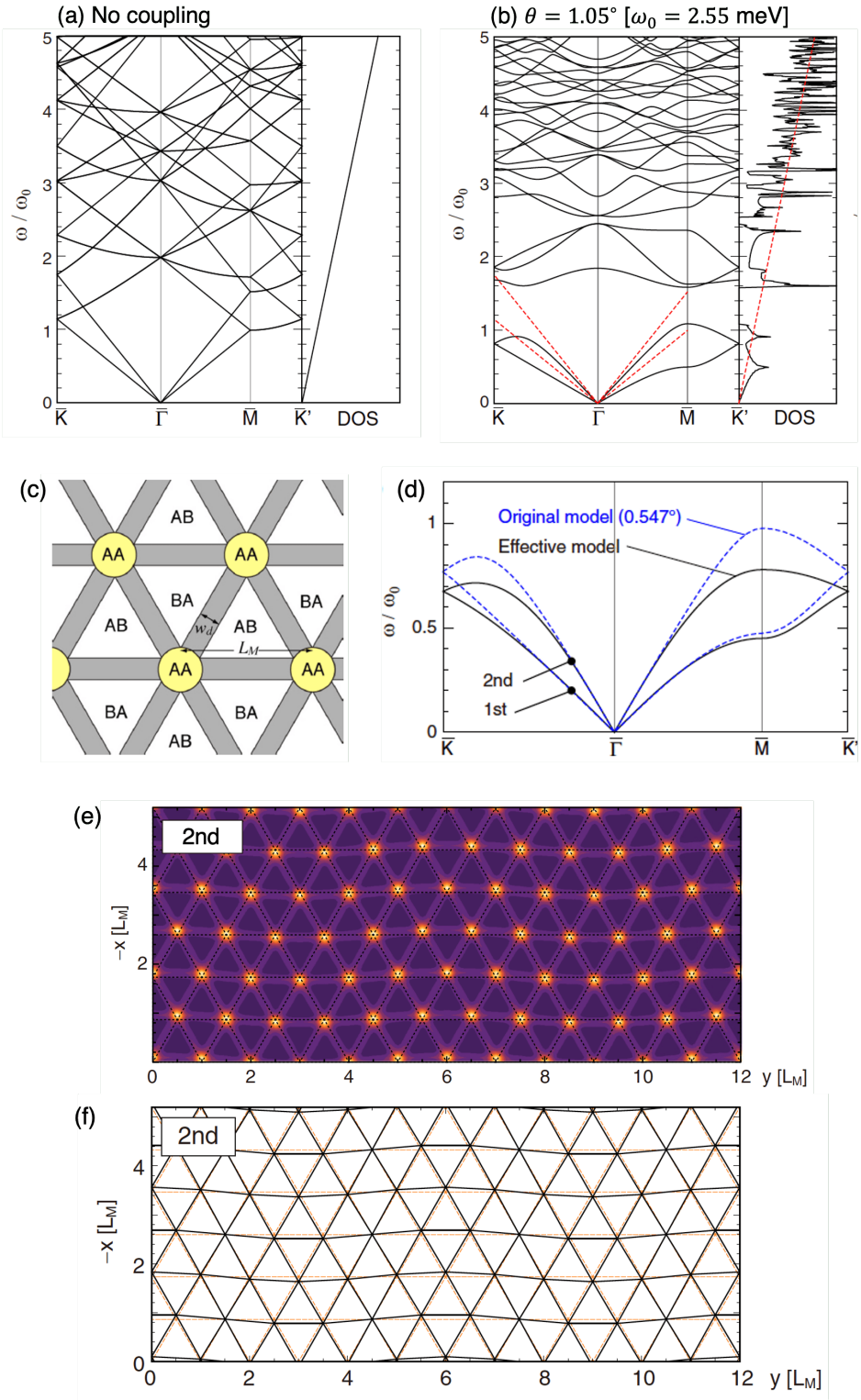

Figure 1.6: Phonon dispersion of the interlayer antisymmetric modes of TBG for (a) no interlayer coupling case and (b) $\theta = 1.05°$. Panel (a) also corresponds to the empty-lattice folding of the LA and TA phonons of graphene. (c) Schematic diagram of the mass-bond model. (d) Phonon dispersion of the original numerical calculation for $\theta = 0.547°$ and the effective mass-bond model. Phonon wave functions for the second mode at $\mathbf{q} = [0, 2\pi/(6L_M)]$ in (e) 1.05° TBG and the (f) effective model. All figures are obtained from [45].

out-of-plane modes, which is calculated by continuum method [53], molecular dynamics [109], and a DFT-based continuum method [52]. Generalization to higher number of layers was also investigated [110, 108], as well as the discussions on the symmetry origins in relation to the generally incommensurate nature of the moiré superlattice [108]. The interaction of the renormalized phonons with the electrons were also studied [46, 111, 112], where coupling enhancement at low twist angle is predicted [111], and possible explanation of the very low critical temperature for the linear-in-temperature resistivity behavior is also proposed [73, 112].

1.4 Moiré superlattices beyond TBG

The wealth of new physics discovered in twisted bilayer grpahene attracted significant interest to the study of moiré superlattices beyond TBG. Some of the well-studied examples are graphene/hBN and bilayer TMDs. These materials are also found to exhibit novel properties. For instance, the few tens of nanometers period of the moiré potential in graphene/hBN heterostructures provides the necessary length scale to observe Hofstadter's butterfly, i.e., fractal electronic spectrum, at an accessible magnetic field strength, as well as the fractional quantum Hall effects [17, 78, 19, 21]. In TMD moiré superlattices, an isolated flat band also appears and various correlated phases are also observed [30, 34, 113, 114, 36, 115, 116, 117]. In this section, we briefly review the physical properties of moiré bilayer systems beyond TBG, that includes hBN and TMD materials. Particularly, we focus on how the differences in the moiré superlattice structure are reflected in the lattice relaxation and the phonon properties.

1.4.1 Atomic structure and lattice relaxation

Figure 1.7 (a) and (b) show the atomic structure of hBN and TMD, respectively. Instead of carbon atoms as in graphene, the A and B sublattices of the honeycomb

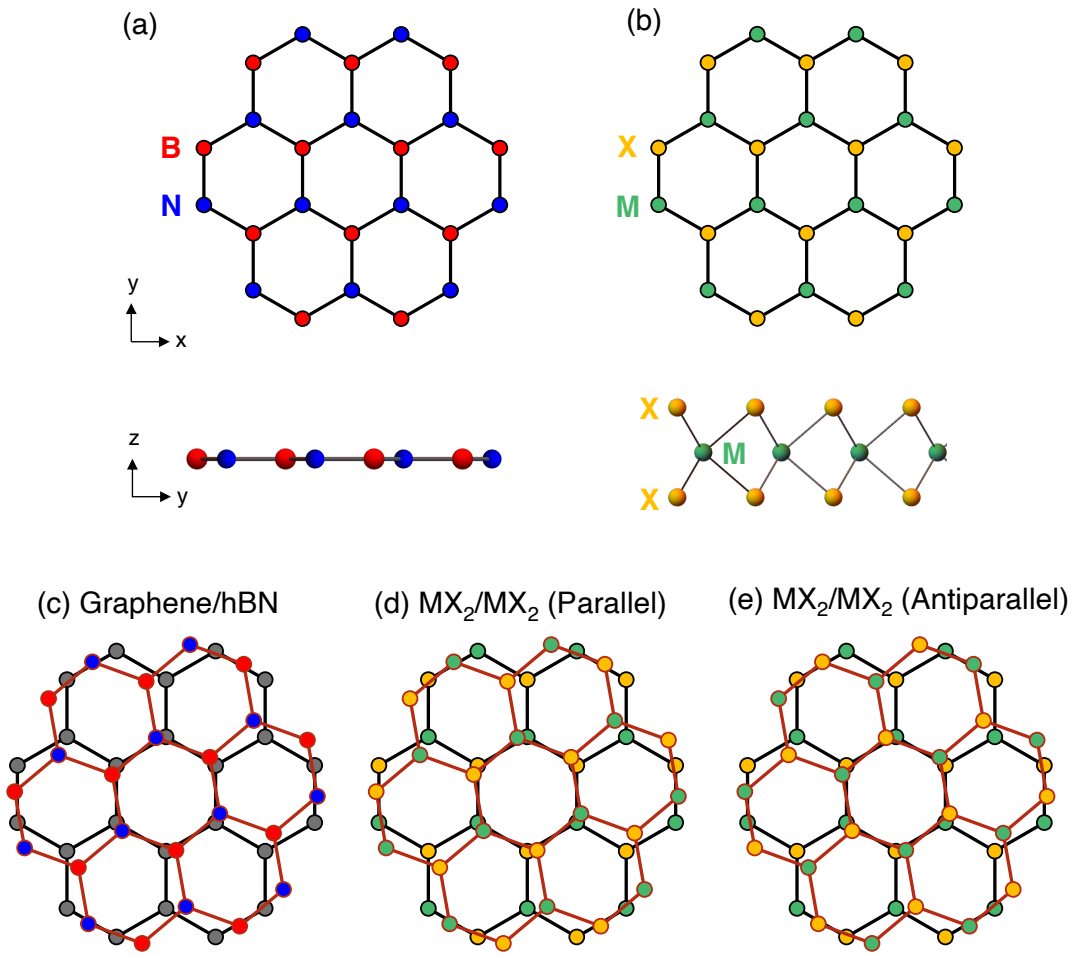

Figure 1.7: Atomic structure of (a) hexagonal boron nitride (hBN) and (b) transition metal dichalcogenides (TMD). In (c), M denotes transition metal atoms and X denotes chalcogen atoms. (c-e) Different stacking formation of twisted bilayers.

lattice in hBN are occupied by boron and nitrogen atoms. As for TMD, the two sublattices are occupied by transition metal atoms (e.g., Mo, W), denoted by ′M′, and two chalcogen atoms (e.g., S, Se, Te), denoted by ′X′, which are separated at a distance perpendicular to the two-dimensional plane. The lattice constant of hBN is closely similar to that of TBG, with approximately 1.8% difference, while the lattice constant of TMD is generally around 30% larger.

In constructing twisted bilayer systems, it is possible to stack two monolayers of the same type (homobilayer) or different type (heterobilayer). One of the most common example of heterobilayer is graphene/hexagonal boron nitride [Fig. 1.7(c)] In homobilayer with different sublattice atoms, two different way of

stacking can also be realized, which are parallel stacking (perfect alignment of the two layers) and antiparallel stacking (one of the layers are rotated by 180°), as illustrated in Fig. 1.7(d) and (e). One of the physical properties that demonstrates the significant difference among the variety of twisted bilayer structures is the lattice relaxation. Figure 1.8 shows the local AA, AB, and BA stacking structure [see Fig. 1.4(a)] along with the corresponding binding energy landscape for the moiré superlattice in graphene/hBN, parallel-stacked MoS_2, and the antiparallel-stacked MoS_2.

In graphene/hBN, the local AA stacking (where both boron and nitrogen atoms are on top of carbon atoms of graphene) represents the highest energy (least preferable) stacking structure while the AB stacking (boron on carbon) correspond to the lowest energy (most preferable) configuration. Here, the difference of the binding energy between AA/BA is approximately a tenth of the AA/AB [118]. As a result, the relaxed structure of graphene/hBN consists of an enlarged AB stacking regions which forms an effective hexagonal domain pattern in contrasts to the triangular pattern of TBG [see Fig. 1.4(e)].

Meanwhile, the parallel- and antiparallel-stacked MoS_2 have a clearly dissimilar binding energy on their corresponding AA, AB, and BA stacking configurations. In the parallel MoS_2, the AB and BA configuration are a mirror images of each other along the xy-plane between the layers, resulting to an identical stacking energy. Conversely, the AB and BA stacking strucures in antiparallel MoS_2 are no longer related by mirror symmetry and they have different stacking energy. This leads to distinct a relaxed structure as observed in the experiments [119, 120]. The parallel case has a TBG-like triangular domain shape at low twist angle, while the antiparallel one transitions from a triangular structure at large twist angle, towards a graphene/hBN-like honeycomb structure in the low-θ limit [86, 121, 122].

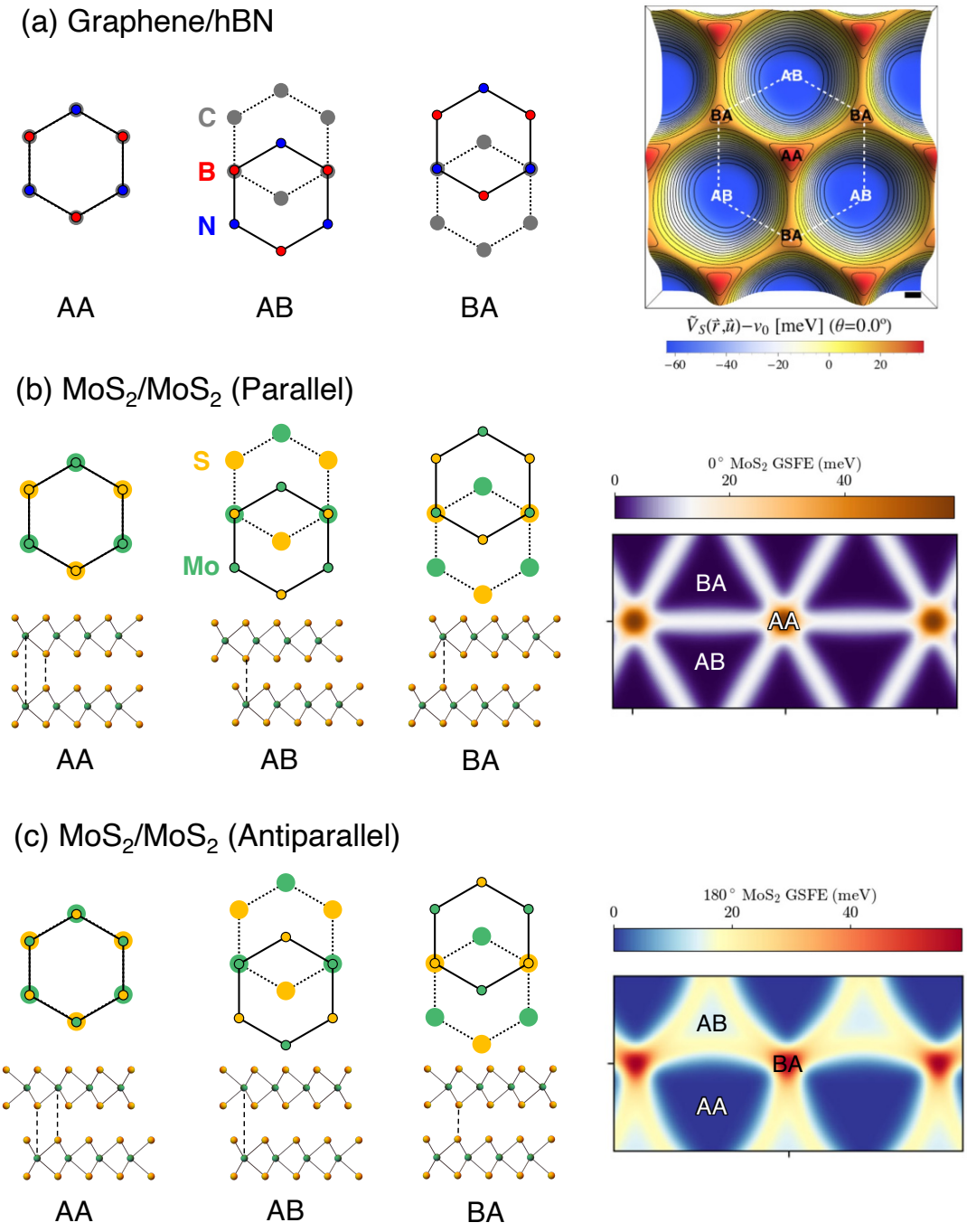

Figure 1.8: Different local stacking structures and the interlayer binding energy for a variety of twisted bilayer systems [118, 86].

1.4.2 Phonon properties

Moiré effect is also expected to be present in the vibrational properties of twisted bilayers beyond TBG. In twisted bilayer hBN, measurements of optical phonon frequency reveals multiple signals which correspond to different localized stacking in the relaxed domain structures [123]. Renormalization effects induced by lattice relaxation was also observed in twisted bilayer MoS_2 [50]. There, the frequency shift of the shear modes (i.e., interlayer antisymmetric in-plane mode) and the breathing mode (i.e., interlayer antisymmetric out-of-plane mode) for different twist angle was observed and the regimes corresponding to the fully reconstructed structure ($\theta < 2^\circ$) can be identified. Theoretically, the phonons of twisted TMD system at small twist angle is calculated by continuum method [55], molecular dynamics [48, 51], and hybrid continuum-DFT method [52]. The molecular dynamics calculation predicts phonon velocity reduction of the LA and TA modes similar to TBG [45, 46]. The chiral properties of the emergent moiré phonons are also discussed [55, 51]. The appearance of these chiral phonons is attributed to the lack of inversion symmetry in the the moiré potential. These studies demonstrate how the phonons of twisted bilayer systems are strongly renormalized by the interlayer moiré potential and the lattice relaxation. However, little is known on how the differences in the relaxed structure of various twisted bilayer systems, as illustrated in Fig. 1.8, are manifested in the reconstructed phonon bands.

In this thesis, we will demonstrate that the geometry of the relaxed structure has a strong relationship to the phonon properties of twisted bilayer moiré superlattices. This relation is represented by universal features in the phonon band structure across different systems with similar profile of interlayer binding energy. We also develop an effective model that is able to capture the low-frequency band structure that can be utilized to elucidate the nature of the flat phonon bands observed across different systems. Furthermore, we also demonstrate that the absence of inversion symmetry in the moiré-induced interlayer potential, such as in graphene/hBN, leads to the appearance of superlattice phonon modes with finite

angular momentum, signifying the presence of chiral phonons at moiré scale.

1.5 Thermal transport in 2D materials

Heat transport in 2D materials has attracted notable interest because of its superiority and its sensitivity to heterostructuring. For example, the high thermal conductivity of suspended graphene [124, 125, 126, 127] is significantly decreased in the presence of substrate or other layer due to strong scattering of flexural phonons [128, 129, 130, 131, 132, 133, 134]. Meanwhile, experimental measurements demonstrated further suppression when rotationally stacked graphene layers [135, 136]. Theoretical simulations showed that such a thermal conductivity reduction by a twist can be caused by the enhancement of anharmonic phonon scattering and the redistribution of phonons to higher frequencies [137, 138, 139, 140, 141]. While all these simulations assumed the room temperature and above, the effect of moiré-induced phonon band reconstruction on the thermal properties is expected to be relevant in the low temperature regime, and it remains unknown.

In this thesis, we calculate the thermal conductivity of various representative twisted bilayer systems, including TBG, twisted graphene/hBN, and also twisted bilayer MoS_2 as representation of the TMD family. Using the continuum model and the semiclassical approach, we demonstrate that the flattening of the low-energy phonons bands across different systems leads to a significant suppression of thermal conductivity up to 40%, resulting in a characteristic deviation from the generic quadratic temperature dependence of thermal conductivity in two-dimensional system.

Chapter 2

Continuum theory of phonons in moiré superlattice

In this Chapter, we introduce the continuum approach to calculate phonons in twisted bilayer systems. We begin by constructing the moiré superlattice from a pair of generic two-dimensional honeycomb lattice. Then, we describe the formulation of continuum Lagrangian which takes into account the kinetic energy, intralayer elastic energy, and the interlayer binding energy, in terms of displacement on both layers. Next, we obtain the time-indepedent solution to the Euler-Lagrange equations, which correspond to the displacements that minimize the total energy, i.e., lattice relaxation. Finally, we describe the time-dependent solution and derive the dynamical equations from which the phonon frequency and the corresponding phonon eigen modes can be obtained.

2.1 Geometry of moiré superlattice

We consider a twisted bilayer system composed of two honeycomb lattice layers with generally different lattice constants, a and a', as illustrated in Fig. 2.1(a). The layer 2 is stacked on top of the layer 1 with relative rotation angle θ around a common honeycomb center. We label the sublattices of layer 1 by A and B, and that of layer 2 by A$'$ and B$'$ as in Fig. 2.1(a). The primitive lattice vectors of layer 1 are defined as $\mathbf{a}_1 = a(1, 0)$ and $\mathbf{a}_2 = a(1/2, \sqrt{3}/2)$, and those of layer 2 are given by $\mathbf{a}'_i = \hat{M}\hat{R}\,\mathbf{a}_i\,(i = 1, 2)$, with rotation matrix $\hat{R}(\theta)$ and isotropic expansion matrix $\hat{M} = (1+\varepsilon)\hat{I}$ where $\varepsilon = (a'-a)/a$. The corresponding reciprocal

lattice vectors for layer 1 and 2 are given by $\mathbf{b}_i$ and $\mathbf{b}'_i$, respectively, which satisfy $\mathbf{a}_i \cdot \mathbf{b}_j = \mathbf{a}'_i \cdot \mathbf{b}'_j = 2\pi\delta_{ij}$. A long-range moiré interference pattern appears due to a slight mismatch from a small difference in lattice constant or small twist angle. The reciprocal lattice vectors of the pattern are given by $\mathbf{G}_i^{\mathrm{M}} = \mathbf{b}_i - \mathbf{b}'_i$, while the corresponding real-space lattice vectors are obtained from the condition $\mathbf{L}_i^{\mathrm{M}} \cdot \mathbf{G}_j^{\mathrm{M}} = 2\pi\delta_{ij}$. The moiré period $L_{\mathrm{M}} = |\mathbf{L}_i^{\mathrm{M}}|$ can be expressed as

$$L_{\mathrm{M}} = a\frac{1+\varepsilon}{\sqrt{\varepsilon^2 + 2(1+\varepsilon)(1-\cos\theta)}}. \tag{2.1}$$

For honeycomb lattice components, we take graphene, hexagonal boron nitride, and molybdenum disulfide with lattice constant of $a \approx 0.246$ nm, 0.2504 nm, and 0.317 nm, respectively. In this paper, we consider twisted bilayer graphene (TBG) and twisted bilayer molybdenum disulfide (t-MoS_2) as examples of homobilayer ($\varepsilon = 1$) and also twisted graphene/hexagonal boron nitride (t-G/hBN) as a heterobilayer ($\varepsilon \neq 1$). In Fig. 2.1(c), we illustrate the formation of moiré superlattice in t-G/hBN with $\theta = 1.25°$ where a lattice constant difference $\varepsilon \approx 1.8\%$ and the twist angle produce a moiré pattern of $L_{\mathrm{M}} = |\mathbf{L}_i^{\mathrm{M}}| \approx 8.8$ nm.

Across the moiré pattern, the local stacking structure changes smoothly at the atomic scale. At a given position $\mathbf{r}$, it is characterized by the phase difference (φ_1, φ_2) defined as

$$\varphi_j(\mathbf{r}) = (\mathbf{b}_j - \mathbf{b}'_j) \cdot \mathbf{r} = \mathbf{G}_j^{\mathrm{M}} \cdot \mathbf{r}. \tag{2.2}$$

For example, $(\varphi_1, \varphi_2) = (0, 0)$, $(2\pi/3, 2\pi/3)$ and $(4\pi/3, 4\pi/3)$ correspond to AA (complete alignment of the honeycomb lattices), AB (B′-site of layer 2 on top of A-site of layer 1), and BA (A′-site of layer 2 on top of B-site of layer 1), respectively [Fig. 2.1(b)]. We note that, when stacking two monolayers with different sublattice atoms, e.g., t-MoS_2, there are two possible stacking configuration, parallel (P) and antiparallel (AP), which are related by 180° rotation of layer 2. In the parallel stacking, the two layers have identical atoms at A and A′ (B and B′), whereas in the antiparallel stacking, the two layers have different atoms on the

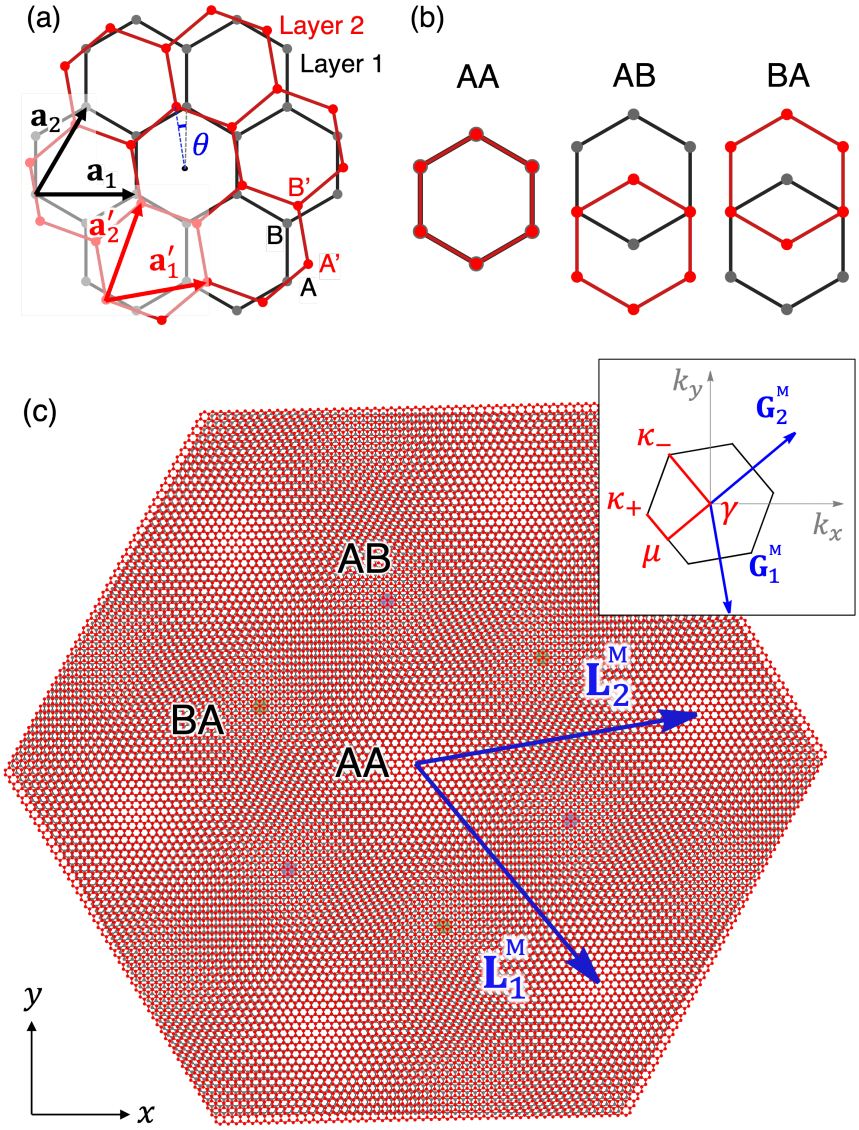

Figure 2.1: (a) Schematic diagram of a twisted bilayer system. (b) Three local stacking structures AA, AB, and BA. (c) Non-relaxed atomic structure of t-G/hBN with $\theta = 1.25°$. The inset shows the first moiré Brillouin zone.

same sublattice sites.

2.2 Continuum Lagrangian

We describe the in-plane lattice vibration in the twisted bilayer systems using a continuum approach. Specifically, we express the Lagrangian as a functional of smoothly-varying lattice displacement field (shifts of atoms) and obtain the Euler-Lagrange equation. The Lagrangian is given by $L = T - (U_E + U_B)$ with kinetic energy T, the elastic energy U_E and the interlayer binding energy U_B. In the following, we generalize the formulation for TBG [85, 45] to also include hetero moiré bilayers consisting of different 2D materials.

The interlayer binding energy U_B is expressed as integration of the binding energy depending on the local interlayer configuration. As a simple example, let us consider a one-dimensional system composed of two parallel atomic chains with different lattice constants. We describe the atomic periodicities of chain 1 and 2 by sinusoidals $\cos bx$ and $\cos b'x$, respectively, where minima of the functions represent the atomic positions. We assume $|b - b'| \ll b, b'$, i.e., the moiré period is much longer than the atomic periods. The local structure at position x is characterized by the phase difference between the two sinusoidals, $\varphi(x) = (b-b')x$. Here $\varphi = 0$ represents a perfectly overlapping arrangement where atoms of chain 1 and 2 are aligned, while $\varphi = \pi$ is a staggered configuration where the atoms are aligned with the midpoint of bonds of the other chain. The local interchain binding energy can be written as $V[\varphi(x)]$, a functional of the local phase difference. The $V[\varphi]$ must be a periodic function satisfying $V[\varphi + 2\pi] = V[\varphi]$.

Now we consider the lattice distortion parallel to the chain, described by smooth displacement field $u(x)$ and $u'(x)$ for chain 1 and 2, respectively. Then the sinusoidal functions are changed to $\cos b(x - u(x))$ and $\cos b'(x - u'(x))$, and

hence the phase difference at x becomes

$$\begin{aligned}\varphi(x) &= b(x-u(x)) - b'(x-u'(x)) \\ &= G^M(x-u^+(x)/2) + \bar{b}\,u^-(x),\end{aligned} \tag{2.3}$$

where $G^M = b - b', \bar{b} = (b+b')/2$, and $u^\pm = u' \pm u$ are interlayer-symmetric and asymmetric components of the displacement. The local inter-chain binding energy in the presence of the distortion is given by $V[\varphi(x)]$ with $\varphi(x)$ of Eq. (2.3).

The binding energy between two layers in twisted bilayer systems can be described in a parallel manner. The periodicity of individual honeycomb lattices are modelled by $\sum_{j=1}^{3}\cos\mathbf{b}_j\cdot\mathbf{r}$ and $\sum_{j=1}^{3}\cos\mathbf{b}'_j\cdot\mathbf{r}$ for layer 1 and 2, respectively, where the minima represent the atomic positions. The local interlayer arrangement is characterized by the phase difference (φ_1,φ_2), where $\varphi_j(\mathbf{r}) = (\mathbf{b}_j - \mathbf{b}'_j)\cdot\mathbf{r}$ for a rigid lattice without distortion. Here $(\varphi_1,\varphi_2) = (0,0)$, $(2\pi/3, 2\pi/3)$ and $(4\pi/3, 4\pi/3)$ correspond to AA, AB and BA stacking, respectively. Due to 120° symmetry of the system, the local binding energy should be expressed as a symmetric function of φ_1, φ_2, and $\varphi_3(= -\varphi_1 - \varphi_2)$. In the lowest harmonics, it is written as

$$V[\varphi_1,\varphi_2] = \sum_{j=1}^{3} 2V_0\cos\left[\varphi_j + \varphi_0\right] + V_{\text{const}}. \tag{2.4}$$

The energy of AA, AB, and BA bilayer stacking is then given by $V_{AA} = 6V_0\cos(\varphi_0)$, $V_{AB} = 6V_0\cos(\varphi_0 + \frac{2}{3}\pi)$, and $V_{BA} = 6V_0\cos(\varphi_0 - \frac{2}{3}\pi)$. Here we obtain the parameters (V_0,φ_0) from the relative values of V_{AA}, V_{AB}, and V_{BA} found in the literature. Table 2.1 lists the values of (V_0,φ_0) and the corresponding (V_{AA}, V_{AB}, V_{BA}) for the systems considered in this thesis.

Now we consider smooth, in-plane displacement fields $\mathbf{u}^{(1)}(\mathbf{r},t)$ and $\mathbf{u}^{(2)}(\mathbf{r},t)$ for layer 1 and layer 2, respectively, which represent atomic shifts at the position $\mathbf{r}$ and time t. We also define the symmetric and antisymmetric components as

Table 2.1: Parameters for interlayer binding energy, (V_0, φ_0), and the corresponding (V_{AA}, V_{AB}, V_{BA}) for the considered systems in this paper. Note that the zero-energy reference of the interlayer binding energy is arbitrary. The unit of V_0, V_{AA}, V_{AB}, and V_{BA} is eV/nm^2.

	V_0	φ_0	V_{AA}	V_{AB}	V_{BA}	Ref.
TBG	0.160	0	0.961	-0.481	-0.481	[79, 80]
t-G/hBN	0.202	0.956	0.700	-1.208	0.509	[118]
t-MoS_2 (P)	0.0889	0	0.533	-0.267	-0.267	[121, 142]
t-MoS_2 (AP)	-0.0801	-0.805	-0.333	-0.133	0.467	[121, 142]

Table 2.2: Lamé parameter and mass density used in the calculation.

	λ (eV/Å^2)	μ (eV/Å^2)	ρ (10^{-8} g/cm^2)	Ref.
Graphene	3.25	9.57	7.61	[144, 145]
hBN	3.5	7.8	7.59	[146, 145]
MoS_2	4.23	4.23	30.5	[121, 142]

$\mathbf{u}^{\pm}(\mathbf{r},t) = \mathbf{u}^{(2)}(\mathbf{r},t) \pm \mathbf{u}^{(1)}(\mathbf{r},t)$. The phase difference becomes

$$\begin{aligned}\varphi_j(\mathbf{r},t) &= \mathbf{b}_j \cdot \left(\mathbf{r} - \mathbf{u}^{(1)}(\mathbf{r},t)\right) - \mathbf{b}'_j \cdot \left(\mathbf{r} - \mathbf{u}^{(2)}(\mathbf{r},t)\right) \\ &= \mathbf{G}^{\mathrm{M}}_j \cdot \left(\mathbf{r} - \mathbf{u}^{+}(\mathbf{r},t)/2\right) + \bar{\mathbf{b}}_j \cdot \mathbf{u}^{-}(\mathbf{r},t), \end{aligned} \tag{2.5}$$

where $\bar{\mathbf{b}}_j = (\mathbf{b}_j + \mathbf{b}'_j)/2$. The total interlayer binding energy is then calculated by taking the integral over the system,

$$U_B = \int V[\varphi_1(\mathbf{r},t), \varphi_2(\mathbf{r},t)]\, d^2\mathbf{r}. \tag{2.6}$$

The energy cost associated with the in-plane distortion is described by a standard elastic theory [143],

$$\begin{aligned}U_E = \sum_{l=1}^{2} \frac{1}{2} \int & (\lambda^{(l)} + \mu^{(l)}) \left(u^{(l)}_{xx} + u^{(l)}_{yy}\right)^2 \\ & + \mu^{(l)} \left[\left(u^{(l)}_{xx} - u^{(l)}_{yy}\right)^2 + 4\left(u^{(l)}_{xy}\right)^2\right] d^2\mathbf{r}, \end{aligned} \tag{2.7}$$

where $u^{(l)}_{ij} = (\partial_i u^{(l)}_j + \partial_j u^{(l)}_i)/2$ is the strain tensor, and $\lambda^{(l)}$ and $\mu^{(l)}$ are the Lamé parameters for layer l which are given in Table 2.2.

Meanwhile, time-dependent displacement field gives a kinetic energy which is expressed as

$$T = \sum_{l=1}^{2} \int \frac{1}{2} \rho^{(l)} \left(\dot{u}_x^{(l)2} + \dot{u}_y^{(l)2} \right) d^2\mathbf{r}, \tag{2.8}$$

where $\rho^{(l)}$ is the mass density of layer l. The mass density for graphene, hBN, and MoS_2 are given in Table 2.2.

The Lagrangian of the moiré bilayer system is given by $L = T - (U_E + U_B)$ which is a functional of the displacement vector fields $\mathbf{u}^{(l)}(\mathbf{r}, t)$. We rewrite the Lagrangian in terms of the symmetric and antisymmetric displacement vector fields $\mathbf{u}^{\pm}$. The Euler-Lagrange equation for $\mathbf{u}^{\pm}$ is obtained as

$$\frac{1}{2} \left[\begin{pmatrix} \rho & \rho' \\ \rho' & \rho \end{pmatrix} \frac{\partial^2}{\partial t^2} + \begin{pmatrix} \hat{K} & \hat{K}' \\ \hat{K}' & \hat{K} \end{pmatrix} \right] \begin{pmatrix} \mathbf{u}^+ \\ \mathbf{u}^- \end{pmatrix} = \sum_{j=1}^{3} 2V_0 \sin\left[\varphi_j(\mathbf{r}, t) + \varphi_0\right] \begin{pmatrix} -\mathbf{G}_j^{\mathrm{M}}/2 \\ \bar{\mathbf{b}}_j \end{pmatrix}, \tag{2.9}$$

where

$$\hat{K} = -\begin{pmatrix} (\lambda + 2\mu)\partial_x^2 + \mu\partial_y^2 & (\lambda + \mu)\partial_x\partial_y \\ (\lambda + \mu)\partial_x\partial_y & (\lambda + 2\mu)\partial_y^2 + \mu\partial_x^2 \end{pmatrix}, \tag{2.10}$$

$$\hat{K}' = -\begin{pmatrix} (\lambda' + 2\mu')\partial_x^2 + \mu'\partial_y^2 & (\lambda' + \mu')\partial_x\partial_y \\ (\lambda' + \mu')\partial_x\partial_y & (\lambda' + 2\mu')\partial_y^2 + \mu'\partial_x^2 \end{pmatrix}, \tag{2.11}$$

and

$$\begin{aligned} \lambda &= \frac{\lambda^{(2)} + \lambda^{(1)}}{2}, \quad \lambda' = \frac{\lambda^{(2)} - \lambda^{(1)}}{2}, \\ \mu &= \frac{\mu^{(2)} + \mu^{(1)}}{2}, \quad \mu' = \frac{\mu^{(2)} - \mu^{(1)}}{2}, \\ \rho &= \frac{\rho^{(2)} + \rho^{(1)}}{2}, \quad \rho' = \frac{\rho^{(2)} - \rho^{(1)}}{2}. \end{aligned} \tag{2.12}$$

Note that ρ and ρ' in Eq. (2.9) are multiplied by a 2×2 unit matrix.

We see that λ', μ', ρ' are responsible for the hybridization of interlayer symmetric component $\mathbf{u}^+$ and anti-symmetric component $\mathbf{u}^-$. For homobilayers, $\lambda', \mu', \rho' = 0$ which means that the antisymmetric and symmetric modes are completely decoupled. For graphene/hBN case, λ', μ', ρ' are much smaller than λ, μ, ρ, respectively, and hence we neglect these hybridization terms hereafter.

The effect of the moiré interlayer coupling is also much more significant in the antisymmetric part than in the symmetric part, as the phase difference φ_i in Eq. (2.5) is more sensitive to $\mathbf{u}^-$ because of $|\bar{\mathbf{b}}_j| \gg |\mathbf{G}_j^{\mathrm{M}}|$. By neglecting $\mathbf{u}^+$ in φ_i, the equation of motion for $\mathbf{u}^+$ becomes equivalent to that for the single-layer honeycomb lattice with the averaged parameters of Eq. (2.12). As a result, the symmetric phonon modes are simply represented by the longitudinal (LA) and transverse (TA) acoustic modes with phonon velocity

$$v_{\mathrm{L}} = \sqrt{\frac{\lambda + 2\mu}{\rho}} \quad \text{and} \quad v_{\mathrm{T}} = \sqrt{\frac{\mu}{\rho}}, \tag{2.13}$$

respectively.

2.3 Static case: Lattice relaxation

We assume a solution for the anti-symmetric mode in the form of [45]

$$\mathbf{u}^-(\mathbf{r}, t) = \mathbf{u}_0^-(\mathbf{r}) + \delta\mathbf{u}^-(\mathbf{r}, t), \tag{2.14}$$

where $\mathbf{u}_0^-(\mathbf{r})$ is the static equilibrium part and $\delta\mathbf{u}^-(\mathbf{r}, t)$ is a time-dependent perturbation from the equilibrium. The equation for the static solution $\mathbf{u}_0^-(\mathbf{r})$ is given by setting $\delta\mathbf{u}^-(\mathbf{r}, t) = 0$ in Eq. (2.14). Here we assume that $\mathbf{u}_0^-$ has the same periodicity as the original moiré pattern, and write it as

$$\mathbf{u}_0^-(\mathbf{r}) = \sum_{\mathbf{G}} \mathbf{u}_{0,\mathbf{G}}^- e^{i\mathbf{G}\cdot\mathbf{r}}, \tag{2.15}$$

where $\mathbf{G} = m\mathbf{G}_1^{\mathrm{M}} + n\mathbf{G}_2^{\mathrm{M}}$ are the moiré reciprocal lattice vectors. Eq. (2.9) then becomes

$$\hat{K}_{\mathbf{G}}\mathbf{u}_{0,\mathbf{G}}^{-} = \sum_{j=1}^{3} 4V_0 f_{\mathbf{G}}^{j}\bar{\mathbf{b}}_j, \tag{2.16}$$

where

$$\hat{K}_{\mathbf{q}} = \begin{pmatrix} (\lambda+2\mu)q_x^2 + \mu q_y^2 & (\lambda+\mu)q_x q_y \\ (\lambda+\mu)q_x q_y & (\lambda+2\mu)q_y^2 + \mu q_x^2 \end{pmatrix}, \tag{2.17}$$

and $f_{\mathbf{G}}^{j}$ is defined by

$$\sin\left[\mathbf{G}_j^{\mathrm{M}}\cdot\mathbf{r} + \bar{\mathbf{b}}_j\cdot\mathbf{u}_0^{-}(\mathbf{r}) + \varphi_0\right] = \sum_{\mathbf{G}} f_{\mathbf{G}}^{j} e^{i\mathbf{G}\cdot\mathbf{r}}. \tag{2.18}$$

We solve a set of equations (2.16) and (2.18) iteratively as follows [85]. For a given $\mathbf{u}_0^{-}$, we obtain the Fourier component $f_{\mathbf{G}}^{j}$ by Eq. (2.18). We then obtain the $\mathbf{u}_0^{-}$ of the next generation by $\mathbf{u}_{0,\mathbf{G}}^{-} = \sum_{j=1}^{3} 4V_0 f_{\mathbf{G}}^{j}\hat{K}_{\mathbf{G}}^{-1}\bar{\mathbf{b}}_j$ [Eq. (2.16)]. We iterate the process until the solution converges. The order of relevant number of harmonics in the Fourier transformation of $\mathbf{u}_0^{-}$ is characterized by a dimensionless parameter [85],

$$\eta = \frac{L_{\mathrm{M}}}{a}\sqrt{\frac{V_0}{\lambda+\mu}}. \tag{2.19}$$

As the moiré period increases, higher number of Fourier expansion terms become necessary to obtain the converged solution.

Figure 2.2 shows the calculated interlayer binding potential, V, before and after relaxation at various twist angle of all the considered systems. Each system exhibits a characteristic domain pattern, which is determined by relative stabilities among AA, AB and BA stacking configurations (Table 2.1). In TBG [Fig. 2.2(a)] and parallel t-MoS_2 [2.2(c)], the relaxed structure reveals a triangular pattern comprising AB and BA stacking regions, indicative of the energetic equivalence between these configurations [85, 86]. In t-G/hBN [Fig. 2.2(b)], on

the other hand, only the AB stacking dominates in the relaxed structure as it is the only structure with the lowest energy, resulting in a honeycomb domain pattern [118, 147]. Note that the rightmost figure correspond to the case where lattice constant mismatch, ε, is reduced to 0.65% (from the original 1.8%). The antiparallel t-MoS_2 [Fig. 2.2(d)] exhibits a transition between triangular structure towards a honeycomb pattern in the low-θ limit, This behavior arises from the relatively small energy difference between the most stable AA stacking and the second stable AB stacking (see, Table 2.1), resulting in competition of domain structure enlargement before the eventual domination of the AA stacking regions as the twist angle is reduced towards 0° [86, 121, 142].

The higher number of harmonics, as represented by the dimensionless parameter η, at small twist angle, also means that the displacement field becomes sharper with respect to the moiré period L_{M}. Therefore, the η parameter can be generally understood as the degree of lattice relaxation, where large η corresponds to a soft lattice, strong interlayer coupling, and/or large moiré period. In fact, the sharp domain walls at large η represent one-dimensional solitons which is a special solution to the time-independent Euler-Lagrange equations [85, 46, 108]. Using that description, the width of the domain walls is approximately given by[85],

$$w_{\mathrm{d}} \approx \frac{a}{4}\sqrt{\frac{\lambda+\mu}{V_0}}, \tag{2.20}$$

which is independent of the twist angle, and hence, the moiré period.

2.4 Dynamical case: Moiré phonons

The time dependent part in Eq. (2.14) can be expressed in a Fourier series as

$$\delta\mathbf{u}^{-}(\mathbf{r},t) = \frac{1}{\sqrt{S}}\sum_{\mathbf{G}}\sum_{\mathbf{q}}\delta\mathbf{u}^{-}_{\mathbf{q}+\mathbf{G}}(t)e^{i(\mathbf{q}+\mathbf{G})\cdot\mathbf{r}}, \tag{2.21}$$

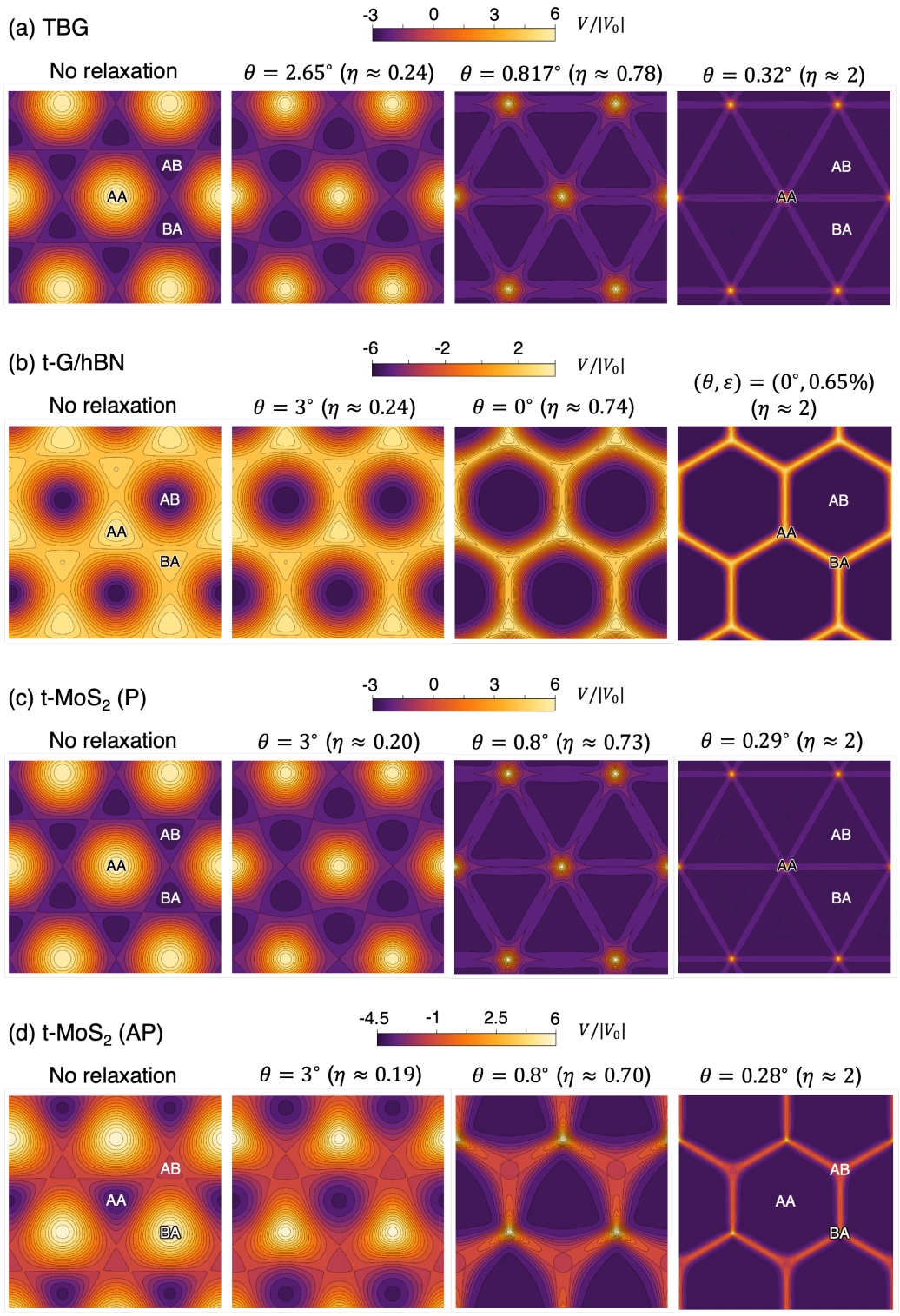

Figure 2.2: Local binding energy of the four considered twisted bilayer systems at various twist angles. Each figures are scaled by the moiré period L_{M}.

where S is the system's total area, $\mathbf{q}$ is the phonon wave vector within MBZ. The equation of motion, Eq. (2.9), is then written as

$$\rho_r \frac{d^2}{dt^2}\delta\mathbf{u}^-_{\mathbf{q}+\mathbf{G}} = -\sum_{\mathbf{G}'} \hat{D}_{\mathbf{q}}(\mathbf{G},\mathbf{G}')\delta\mathbf{u}^-_{\mathbf{q}+\mathbf{G}'}, \tag{2.22}$$

where $\rho_r = \rho/2$ is the relative mass density, $\hat{D}_{\mathbf{q}}(\mathbf{G},\mathbf{G}') = (1/2)\hat{K}_{\mathbf{q}+\mathbf{G}}\delta_{\mathbf{G},\mathbf{G}'} + \hat{V}_{\mathbf{G}'-\mathbf{G}}$ is the dynamical matrix, and $\hat{V}$ is defined as

$$\hat{V}_{\mathbf{G}} = -2V_0 \sum_{j=1}^{3} h^j_{\mathbf{G}} \begin{pmatrix} \bar{b}_{j,x}\bar{b}_{j,x} & \bar{b}_{j,x}\bar{b}_{j,y} \\ \bar{b}_{j,y}\bar{b}_{j,x} & \bar{b}_{j,y}\bar{b}_{j,y} \end{pmatrix}, \tag{2.23}$$

with

$$\cos\left[\mathbf{G}^{\mathrm{M}}_j \cdot \mathbf{r} + \bar{\mathbf{b}}_j \cdot \mathbf{u}^-_0(\mathbf{r}) + \varphi_0\right] = \sum_{\mathbf{G}} h^j_{\mathbf{G}} e^{i\mathbf{G}\cdot\mathbf{r}}. \tag{2.24}$$

At a given $\mathbf{q}$, we obtain the phonon eigen modes by solving the following eigenvalue equation,

$$\rho_r \omega^2_{n,\mathbf{q}} \mathbf{C}_{n,\mathbf{q}}(\mathbf{G}) = \sum_{\mathbf{G}'} \hat{D}_{\mathbf{q}}(\mathbf{G},\mathbf{G}')\mathbf{C}_{n,\mathbf{q}}(\mathbf{G}'), \tag{2.25}$$

where n is the mode index, $\omega_{n,\mathbf{q}}$ is the eigenfrequency, and $\mathbf{C}_{n,\mathbf{q}}(\mathbf{G}) = (C^x_{n,\mathbf{q}}(\mathbf{G}), C^y_{n,\mathbf{q}}(\mathbf{G}))$ is the eigenvector normalized by $\sum_{\mathbf{G}} |\mathbf{C}_{n,\mathbf{q}}(\mathbf{G})|^2 = 1$.

While we neglect distortion on the out-of-plane direction throughout this work, the real sample is expected to be corrugated as in TBG [67, 83, 92], since the optimal interlayer spacing is generally registry-dependent. Accordingly the out-of-plane phonon modes (flexural phonons) would also be subject to some superlattice effect [52, 53]. However, it is relatively minor compared to the complete restoration of in-plane phonon since out-of-plane motion does not affect the moiré pattern unlike in-plane interlayer sliding [45]. Also, the corrugated structure may cause some finite coupling between the in-plane modes and out-of-plane modes, but it is negligible within harmonic approximations [101].

Chapter 3

Phonons in twisted bilayer moiré superlattices

In this chapter, we discuss the properties of the phonons of the various representative twisted bilayer moiré superlattices using the continuum theory described in the previous chapter. In Sec. 3.1, we show the phonon dispersion of twisted bilayer graphene, twisted graphene/hBN, and twisted bilayer MoS_2, including the wave function of some of the modes. Using these results, we demonstrate the universal features as the twist angle reduces towards the low-angle limit. In Sec. 3.2, we construct an effective model that is able to reproduce the properties of moiré phonons in the low-angle limit. In Sec. 3.3, we use the effective model to elucidate the origin of flat phonon bands that are found across different twisted bilayer systems. In Sec. 3.4, we discuss the existence of chiral phonons, given by the finite angular momentum of the moiré phonons due to the lack of inversion symmetry in the twisted graphene/hBN.

3.1 Phonon modes

3.1.1 TBG

In this part, we show the calculated phonon dispersion and wave function of TBG. We note that similar results have been previously shown by Koshino and Son [45]. Here, we reproduce some parts that are relevant to the purpose of this thesis.

Figure 3.1 show the phonon dispersions of in-plane antisymmetric modes of

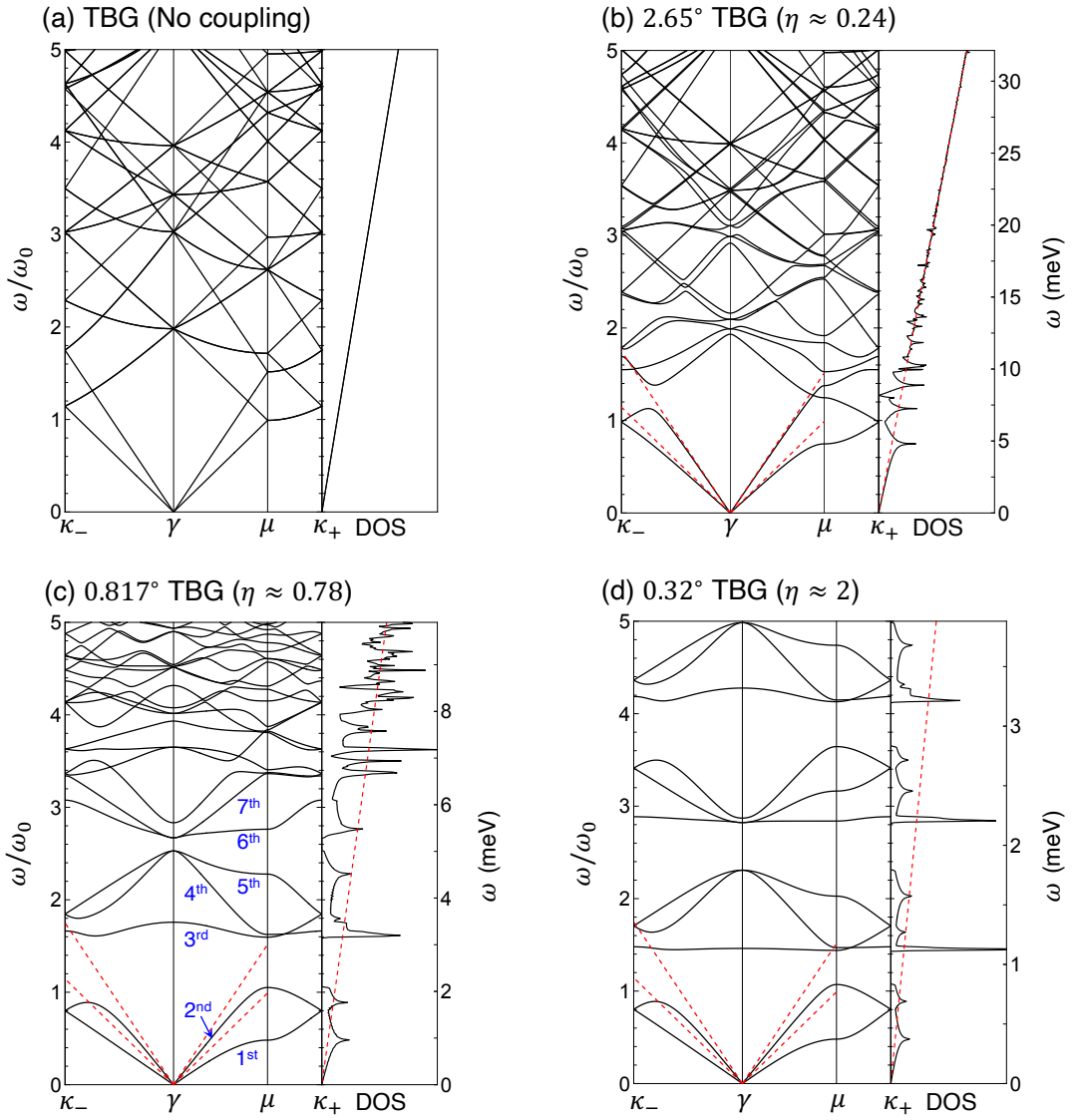

Figure 3.1: Phonon dispersion and density of states of the in-plane antisymmetric mode of TBG with various twist angle. The horizontal axis is scaled by the superlattice Brillouin-zone size $\propto 1/L_{\mathrm{M}}$, and the vetical axis is scaled by $\omega_0 \propto 1/L_{\mathrm{M}}$ (see main text). The value of η is given for each case to indicate the relative strength of interlayer coupling. (a) Phonon dispersion when the interlayer coupling is absent.

TBG ($\mathbf{u}^-$) calculated for $\theta = 2.65°, 0.817°$, and $0.32°$. Here the horizontal axis is scaled by the size of the superlattice Brillouin zone ($\propto 2\pi/L_{\rm M}$ and the vertical axis is scaled by

$$\omega_0 = \frac{2\pi}{L_{\rm M}}\sqrt{\frac{\lambda}{\rho}}, \tag{3.1}$$

where $\sqrt{\lambda/\rho}$ corresponds to the characteristic velocity scale for the acoustic phonons in graphene. The right vertical axis provides the corresponding scale of phonon energy, $\hbar\omega$ in meV. Figure 3.1(a) is the phonon dispersion in the absence of interlayer moiré potential. This is equivalent to the folded linear dispersions of the LA and TA phonons of graphene, which are given by $\omega(\mathbf{q}) = v_L q$ and $v_T q$, respectively, where v_L and v_T are the phonon velocity of the corresponding modes as given in Eq. (2.13). The plotted bands in 3.1(a) are independent of the twist angle, since both the horizontal and vertical axes are normalized by units proportional to $1/L_{\rm M}$. As comparisonn, the same dispersions of the lowest two bands are also indicated by red dashed lines in Figs. 3.1(b)-(d). Note that the phonon band structure of the in-plane symmetric modes ($\mathbf{u}^+$) remain unchanged and they are not drawn in Fig. 4.2(b)-(d).

For the antisymmetric modes, we find the reconstruction of the original acoustic bands of graphene into mini bands of the moiré superlattice, signified by band splittings that show up as sharp peaks in the density of states. This reconstruction becomes more notable at small twist angle, where band gaps gradually open between specific group of bands, i.e., between 2nd and 3rd, 5th and 6th, 8th and 9th. More importantly, we also find the extreme flattening of the third, sixth, and ninth bands, seemingly fitting a specific number pattern given by $3n$ where n is a non-zero positive integer.

Figure 3.2 shows the phonon wave functions for the lowest seven antisymetric modes of TBG with $\theta = 0.817°$, calculated at $\mathbf{q} = [0, 2\pi/(6L_{\rm M})][= (1/4)\gamma\kappa]$. Here, the y axis is taken as the horizontal axis, and the colors represent a snapshot of the local binding energy at a ceratin time of the oscillations. We note that in these plots, the amplitude of the oscillations are amplified for the purpose of

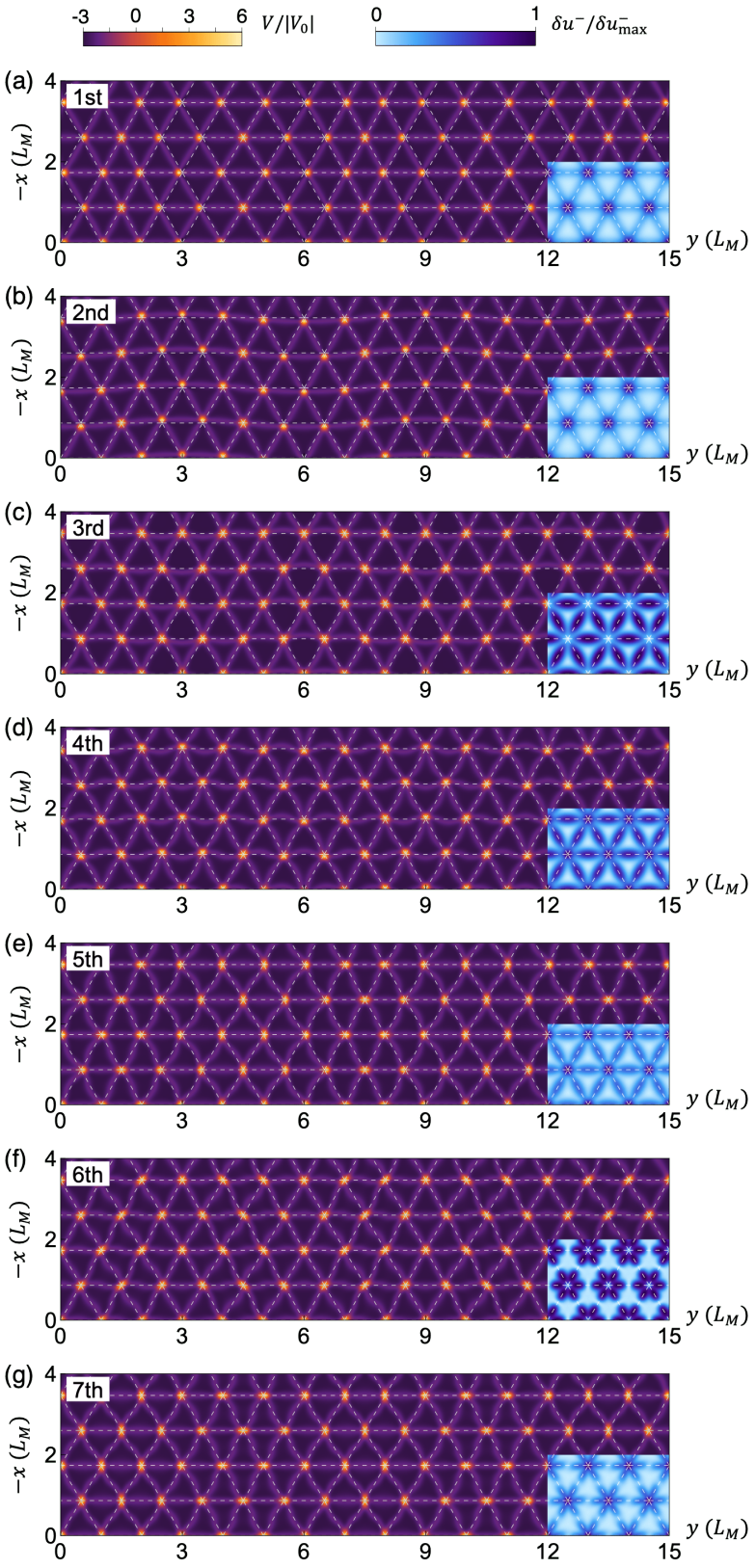

Figure 3.2: Phonon wave functions of the lowest seven modes at $\mathbf{q} = [0, 2\pi/(6L_{\mathrm{M}})]$ in TBG with $\theta = 0.817°$. The y axis is taken as the horizontal axis, and the colors represent the local binding energy. Dashed line indicates the static position of the domain walls.

illustration only. From this figure, we find that the reconstructed phonon modes are seen as the effective vibrations at the moiré scale. For example, the first two modes, as shown in Fig. 3.2(a) and (b), can be viewed as the longitudinal and transverse acoustic modes of the triangular domain pattern of the moiré superlattice. We also note that the phonon velocity of this LA mode is less than the TA mode, in contrary to the LA and TA mode of graphene and other two-dimensional honeycomb lattices, as given by Eq. (2.13). This feature implies that the moiré superlattice has different elasticity nature to the graphene and the description of low-energy phonons requires different lattice model that takes into account the renormalization of the elastic constants [107, 46, 108].

In each panel of Fig. 3.2, an inset (bottom right) shows the spatial distribution of the amplitude of the atomic displacement, $|\delta\mathbf{u}(\mathbf{r})|$ for each corresponding phonon band. Here, we can observe the position of atomic displacement in the graphene lattice which responsible for the effective oscillations in the moiré superlattice. We find that across the lowest seven modes, the atomic vibrations are concentrated in the vicinity of the domain walls. More importantly, we find that for the third and sixth modes, which correspond to the flat bands in Fig. 3.1(c), clearly exhibit nodes where the amplitude completely vanishes. As we argue in the next few sections, this indicates that the wave function is composed of fundamental oscillation modes of independent strings that is intimately related to the flatness of the corresponding bands.

3.1.2 Twisted graphene/hBN

In Fig. 3.3, we show the phonon dispersion of the interlayer antisymmetric modes of twisted graphene/hBN at various twist angles, in a similar way to Fig. 3.1. Fig. 3.3 represents the non-coupling case that is independent of the twist angle which also shown in Fig. 3.3(b)-(d). Fig. 3.3(d) represents the lattice-matching case, as discussed in Sec. 2.3 in the context of lattice relaxation. Here, the lattice-matching allows a moiré period larger than that of 0° twisted graphene/hBN to

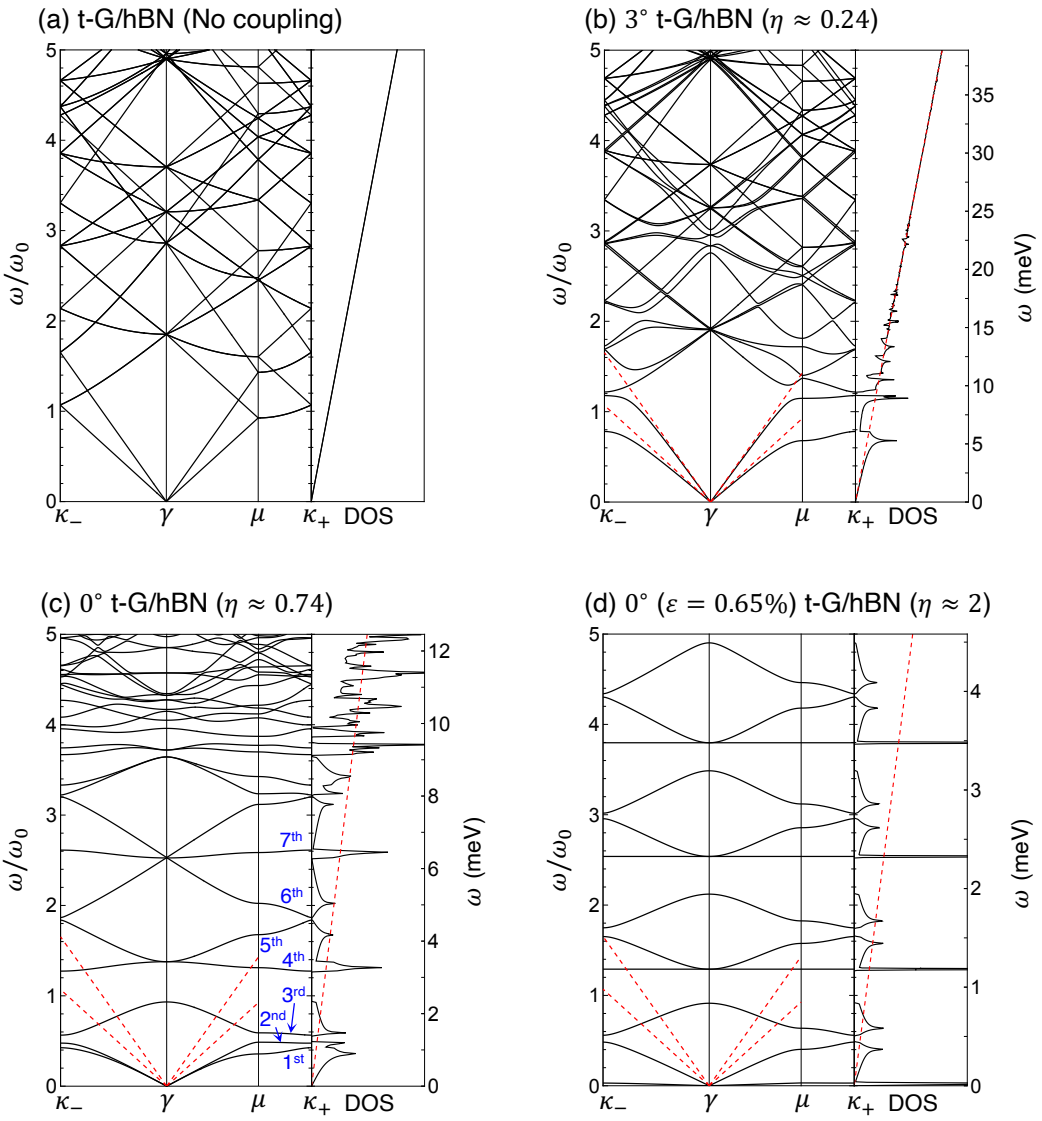

Figure 3.3: Phonon dispersion of the interlayer antisymmetric phonon modes of t-G/hBN for the (a) no coupling case, and three different twist angles, (b) $\theta = 3°$, (c) $0°$, and (d) $0°$ with lattice mismatch reduced to 0.65%.

illustrate the strong interlayer coupling regime ($\eta \approx 2$) [see Eq. (2.19)]. We note that similar effect can be achieved by enhancing V_0, i.e., larger potential difference between the most and least stable stacking regions.

As observed in the case of TBG, the moiré effect in the phonon band structure of interlayer antisymmetric modes is observed as the appearance of gaps and the flattening of particular phonon bands. However, as the interlayer coupling becomes more significant (larger η), the reconstructed bands converge to a completely different structure to those of TBG. Here, we find two different type of gaps, the smaller gaps separate the $3n$+2-th and $3n$+3-th ($n = 0, 1, 2, ..$) bands at the κ_+ and κ_- points, and the larger gaps separating the $3n$+3-th and the $3n$+4-th bands at the γ-point. The small gaps at the MBZ corners are related to the inversion symmetry breaking and the presence of phonons with finite angular momentum, which will be discussed in more detail in Sec. 3.4. We also find that the extreme band flattening are occurring at different band index. In this twisted graphene/hBN system, the flat bands are given by the $3n$+1-th ($n = 0, 1, 2, ...$) band. This suggests different nature of these flat phonon bands to that of TBG, which will be elucidated using effective model described in the later sections.

Figure 3.4 shows the phonon wave functions for the lowest seven antisymetric modes of twisted graphene/hBN with $\theta = 0°$, calculated at $\mathbf{q} = [2\pi/(6L_{\mathrm{M}}), 0][= (1/4)\gamma\kappa]$. In each panel, the spatial distribution of the amplitudes of the atomic oscillation is also shown as inset in the bottom right. Similar to the TBG case, here we also find the renormalized phonon modes are represented as effective oscillations at the moiré scale. This time, these oscillations are given as modulation of the honeycomb domain wall network. The distribution of oscillating atoms are also found to be concentrated in the vicinity of domain walls, which is obvious as the modulation of honeycomb moiré superlattice is just distortion of the domain walls network. For the flat bands, clear nodes with vanishing amplitudes are also observed. However, we will show that the exact location of these clear nodes can be determined which intimately related to the origin of the flat phonon bands.

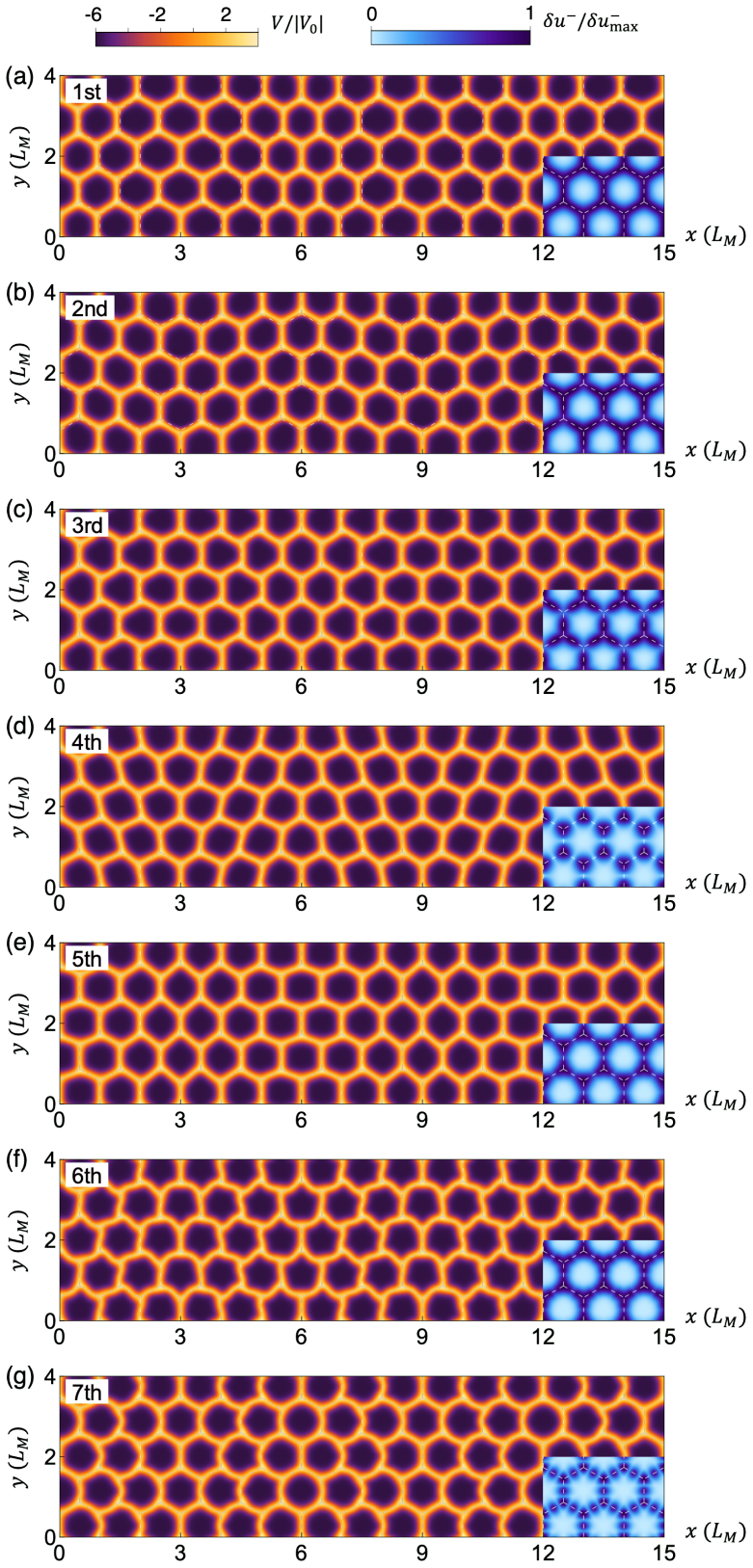

Figure 3.4: Phonon wave functions for the lowest 7 modes (a-h) of the interlayer antisymmetric modes in 0° G/hBN at $\mathbf{q} = (\frac{2\pi}{6L_M}, 0)$. The color gradient represents the local binding energy. The inset at each figure shows the sum of amplitude distribution of all wave vectors within MBZ for the corresponding phonon branch.

3.1.3 Twisted bilayer molybdenum disulfide

Figure 3.5 shows the phonon dispersion of the in-plane antisymmetric modes of twisted bilayer MoS_2 for both parallel and antiparallel case for two different twist angles. Here, we find that the antisymmetric phonon modes of the parallel-stacked case closely resembles to that of TBG [Fig. 3.1]. In fact, around the same relative coupling strength [Fig. 3.1(c) and Fig. 3.5(a); Fig. 3.1(c) and Fig. 3.5(b)], the phonon band structure of the two systems are almost identical, except that those of MoS_2 have a lower energy scale. This similarity is reflected in their relaxed lattice structure where TBG and parallel-stacked t-MoS_2 shares the same triangular domain pattern.

In analogous way, the phonon band structure of the antiparallel case can be understood by comparing its relaxed structure with other systems. At 0.8°, the lattice structure of antiparallel t-MoS_2 correspond to an intermediate state in the transition from triangular structure at large twist angle (weak interlayer coupling) to honeycomb structure at small twist angle (strong interlayer coupling). As a result, while at nominal twist angle [Fig. 3.5(c)], the phonon band structure does not have a clear correspondence to either that of TBG or graphene/hBN, it converges towards a graphene/hBN-like bands in the strong-coupling regime [Fig. 3.5(d)] where the honeycomb domain pattern in the relaxed structure are clearly observed.

These results demonstrate the strong correspondence between lattice relaxation and the phonon band structure and the presence of universal characteristics shared across different twisted bilayer systems. In the following sections, we develop an effective model to reproduce the phonon dispersion of different moiré superlattices can be reproduced and use it to elucidate the origin of various features, particularly the flat bands.

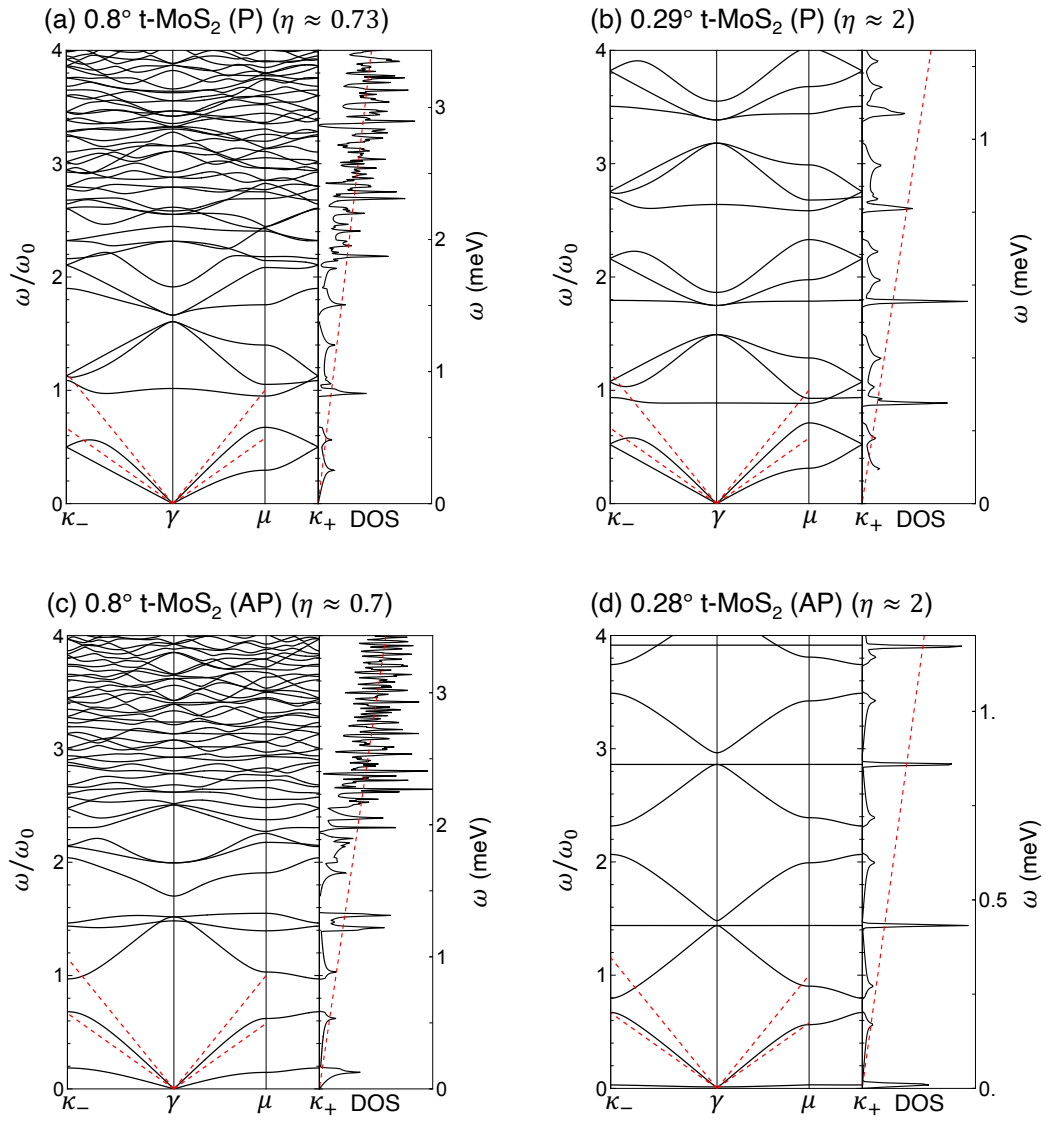

Figure 3.5: Phonon dispersion of twisted bilayer MoS_2 for the parallel case with $\theta =$ (a) 0.8° and (b) 0.29°, and for the antiparallel case with $\theta =$ (c) 0.8° and (d) 0.28°. The red-dashed line corresponds to the lowest two bands of the phonon dispersion in the absence of moiré interlayer coupling.

3.2 Effective model

Effective description of acoustic phonons in the small-θ (strong-coupling) regime of twisted bilayer graphene have been studied using mass-bond model [45], soliton approximation [46], and a fully field theoretical treatment [108]. One of the notable results from these studies is the finite convergence of the phonon velocities of the lowest two modes (the moiré acoustic modes) and the effective elasticity of the moiré superlattice. However, the description of higher energy bands remains unknown. In this section, we presents an extended version of the mass-bond model that reproduces the full band structure in the strong-coupling limit.

3.2.1 Equation of motion

One key element of the domain wall in the relaxed structure of moiré superlattices is that its energy is proportional to its length [107, 45, 46]. This can be understood by the following argument [45]. In the relaxed structure of TBG, the total binding energy per moiré unit cell, relative to the AB/BA stacking, is proportional to the area of the domain walls, $U_B \sim w_d L_{\mathrm{M}}$, where w_d is width of the domain walls. The elastic energy is also concentrated within the domain-wall regions, and it is given by $U_E \sim \lambda(\partial u_i/\partial x_j)^2(w_d L_M)$. Here, λ is a representative scale for the elastic constant, since λ and μ are in the same order of magnitude. In the domain wall, the strain tensor $\partial u_i/\partial x_j$ is of the order of a/w_d since an atomic shift u_i changes by about a inside the domain wall. The relaxed state is then given by the condition $U_E \sim U_B$, and this gives $w_d \sim a\sqrt{\lambda/V_0}$ which correctly approximate the width of the domain walls, Eq. (2.20), which is independent of the twist angle [46, 148].

Now, let us consider a simple oscillations that correspond to the phonon wave functions such as the first few modes in Figs. 3.2 of TBG. During the oscillations, the local changes at a given moiré unit cell are represented by distortion of the domain walls, such as elongation and bending, in which the width of the walls

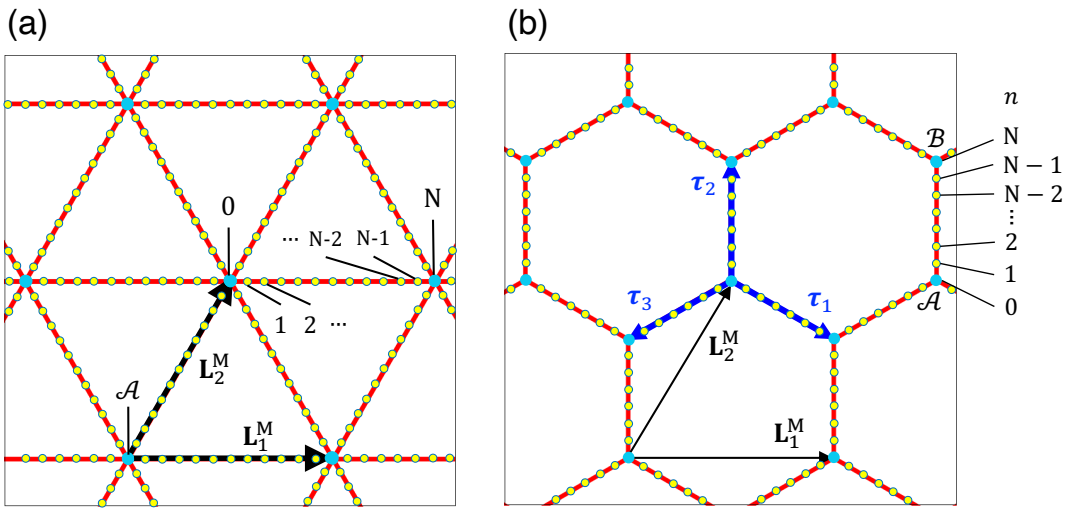

Figure 3.6: Schematic diagram of the effective mass-bond model for the (a) triangular and (b) honeycomb domain walls of the relaxed domain pattern in moiré superlattice [see Fig. 2.2].

remains approximately constant. In such distortion, the actual atoms in the honeycomb lattice are not displaced in a similar way to the domain walls, but the area of the same local atomic configurations is increased (or decreased), so that the total energy change is proportional to the change in the total length of the domain walls. Note that this is contrary to the usual mass-spring model for lattice dynamics, where the energy of the spring proportional to the square of the change in length.

Based on the argument above, we construct a discrete lattice model which simulates the domain wall motion with an array of masses and bonds, as illustrated in Fig. 3.6. Here, a segment of the wall connecting the vertices is broken down into N small segments (bonds) that are linked to masses that can move within the two-dimensional plane. Let us first focus on the honeycomb structure. We define $\boldsymbol{\tau}_j$ $(j = 1, 2, 3)$ as vectors connecting $\mathcal{A}$ (AA in graphene/hBN and BA in antiparallel t-MoS_2) to the nearest $\mathcal{B}$ points (BA in graphene/hBN and AB in antiparallel t-MoS_2). The equilibrium position of a mass is given by

$$\mathbf{r}_{\mathbf{R}}^{(j,n)} = \mathbf{R} + n\boldsymbol{\tau}_j/N, \tag{3.2}$$

where $\mathbf{R} = m_1\mathbf{L}_1^{\mathrm{M}} + m_2\mathbf{L}_2^{\mathrm{M}}$ is the position of the nearest $\mathcal{A}$ sublattice, and $j = 1, 2, 3$ represents the direction of the chain that the mass belongs to, and the index $n = 0, 1, \cdots, N$ specifies the position on the chain as in Fig. 3.6(b). The displacement of the corresponding mass is denoted by $\mathbf{u}_{\mathbf{R}}^{(j,n)} = (u_{x,\mathbf{R}}^{(j,n)}, u_{y,\mathbf{R}}^{(j,n)})$. This is a quantity different from the atomic displacement of the graphene lattice. Note that three vectors $\mathbf{u}_{\mathbf{R}}^{(j,0)}(j = 1, 2, 3)$ are actually the same variable that represents a shift of a vertex mass at $\mathcal{A}$, and likewise $\mathbf{u}_{\mathbf{R}+\boldsymbol{\tau}_1-\boldsymbol{\tau}_j}^{(j,N)}(j = 1, 2, 3)$ express a mass at $\mathcal{B}$.

In the presence of the displacement of masses, the change of total length of the bonds is written in the second order as

$$\Delta L = \frac{1}{2l}\sum_{\mathbf{R}}\sum_{j=1}^{3}\sum_{n=0}^{N-1}\left[|\Delta\mathbf{u}_{\mathbf{R}}^{(j,n)}|^2 - \left(\hat{\boldsymbol{\tau}}_j \cdot \Delta\mathbf{u}_{\mathbf{R}}^{(j,n)}\right)^2\right], \tag{3.3}$$

where $\Delta\mathbf{u}_{\mathbf{R}}^{(j,n)} = \mathbf{u}_{\mathbf{R}}^{(j,n+1)} - \mathbf{u}_{\mathbf{R}}^{(j,n)}$, $l = |\boldsymbol{\tau}_j|/N$ and $\hat{\boldsymbol{\tau}}_j = \boldsymbol{\tau}_j/|\boldsymbol{\tau}_j|$ is a unit vector along j direction. Here, the linear length change to $\mathbf{u}_{\mathbf{R}}^{(j,n)}$ is considered to be zero, assuming that an overall expansion of the whole system is restricted by the boundary condition. The change in the total energy is then given by $U = \alpha V_0 w_d \Delta L$, where w_d is the width of the wall [Eq. (2.20)] and α is a numerical constant to match the energy scale of original system. By the Fourier transform $\mathbf{u}_{\mathbf{R}}^{(j,n)} = \sum_{\mathbf{q}} \mathbf{u}_{\mathbf{q}}^{(j,n)} \exp(i\mathbf{q}\cdot\mathbf{r}_{\mathbf{R}}^{(j,n)})$, U can be written as

$$U = \frac{K}{2}\sum_{\mathbf{q}}\sum_{j=1}^{3}\sum_{n,n'=0}^{N}\left[\mathbf{u}_{-\mathbf{q}}^{(j,n')}\right]^T \hat{D}_{\mathbf{q}}^{j}(n', n)\mathbf{u}_{\mathbf{q}}^{(j,n)}, \tag{3.4}$$

where $K = \alpha V_0 w_d/l$ is the effective spring constant of the bond. The $\hat{D}_{\mathbf{q}}^{j}(n, n')$ is a 2×2 dynamical matrix of which non-zero elements are given by,

$$\hat{D}_{\mathbf{q}}^{j}(n, n) = \begin{cases} \hat{T}_j & (n = 0, N) \\ 2\hat{T}_j & (n = 1, 2, \cdots, N-1), \end{cases} \tag{3.5}$$

$$\hat{D}_{\mathbf{q}}^{j}(n-1, n) = \left[\hat{D}_{\mathbf{q}}^{j}(n, n-1)\right]^{\dagger} = -\hat{T}_j e^{i\mathbf{q}\cdot\tau_j/N}, \tag{3.6}$$

where

$$\hat{T}_j = \begin{pmatrix} 1-(\hat{\tau}_j^x)^2 & -\hat{\tau}_j^x\hat{\tau}_j^y \\ -\hat{\tau}_j^x\hat{\tau}_j^y & 1-(\hat{\tau}_j^y)^2 \end{pmatrix}. \tag{3.7}$$

The $\hat{T}_j$ is a projection operator perpendicular to $\hat{\boldsymbol{\tau}}_j$, which works for an arbitrary vector $\boldsymbol{x}$ as $\hat{T}_j\boldsymbol{x} = (\delta^{\mu\nu} - \hat{\tau}_j^\mu\hat{\tau}_j^\nu)x^\nu = \boldsymbol{x} - \hat{\boldsymbol{\tau}}_j(\hat{\boldsymbol{\tau}}_j \cdot \boldsymbol{x})$.

The kinetic energy of the system is

$$T = \frac{M}{2}\sum_{\mathbf{q}}\left[|\dot{\mathbf{u}}_{\mathbf{q}}^{\mathcal{A}}|^2 + |\dot{\mathbf{u}}_{\mathbf{q}}^{\mathcal{B}}|^2 + \sum_{j=1}^{3}\sum_{n=1}^{N-1}|\dot{\mathbf{u}}_{\mathbf{q}}^{(j,n)}|^2\right], \tag{3.8}$$

where $M = \rho a^2 l/w_d$ is the effective mass [45], and $\mathbf{u}_{\mathbf{q}}^{\mathcal{A}} = \mathbf{u}_{\mathbf{q}}^{(j,0)}$ and $\mathbf{u}_{\mathbf{q}}^{\mathcal{B}} = \mathbf{u}_{\mathbf{q}}^{(j,N)}$. The Euler-Lagrange equation is then given by $M\ddot{\mathbf{u}}_{\mathbf{q}}^{(j,n)} = K\sum_{n'}\hat{D}_{\mathbf{q}}^j(n',n)\mathbf{u}_{\mathbf{q}}^{(j,n')}$, which is solved to obtain eigen phonon frequencies and the corresponding wave functions.

For the triangular effective model, a wall segment connect a single vertex (the AA stacking regions) to the an equivalent vertex in the neighboring moiré unit cells. By following similar derivation to the honeycomb case, the corresponding total energy can be written as

$$U = \frac{K}{2}\sum_{\mathbf{q}}\sum_{j=1}^{3}\sum_{n,n'=0}^{N-1}\left[\mathbf{u}_{-\mathbf{q}}^{(j,n')}\right]^T\hat{D}_{\mathbf{q}}^j(n',n)\mathbf{u}_{\mathbf{q}}^{(j,n)}, \tag{3.9}$$

where the dynamical matrix $\hat{D}_{\mathbf{q}}^j(n,n')$ is now given by

$$\hat{D}_{\mathbf{q}}^j(n,n) = 2\hat{T}_j, \tag{3.10}$$

$$\hat{D}_{\mathbf{q}}^j(n-1,n) = \left[\hat{D}_{\mathbf{q}}^j(n,n-1)\right]^\dagger = -\hat{T}_j e^{i\mathbf{q}\cdot\tau_j/N}. \tag{3.11}$$

The equations of motion is obtained in a similar way. Note that for the triangular case, the number of independent mass displacement are given by $3(N-2)+1$, instead of $3(N-2)+2$ as in the honeycomb case, due to the absence of sublattices,

i.e., extra vertex within the unit cell.

3.2.2 Phonon modes

Figure 3.7 shows the phonon dispersion of the effective model that is fitted to the original band structure of each considered systems in the strong-limit regime ($\eta \approx 2$). Here, we use $N = 50$ and $\alpha = 33.0, 24.2, 22.17, 10.1$ for TBG, parallel t-MoS_2, antiparallel t-MoS_2, and t-G/hBN, respectively. The choice of these parameters is purely based on the best-fit consideration. We see that the effective model qualitatively reproduces the flat bands and the repeating unit of the original band strucutre. For effective triangular model, the flat bands are located at the $3n$-th ($n = 1, 2, ...$) band, while for honeycomb model they are located at the $3n + 1$-th ($n = 0, 1, ...$) band.

The phonon wave functions of the first seven modes of the effective triangular model and honeycomb model are shown in Figs. 3.8 and 3.9, respectively. The wave vector and temporal snapshot are chosen to be the same as the phonon wave function of TBG and t-G/hBN shown in Figs. 3.2 and 3.4. Here, we observe the perfect correspondence of the oscillations mode between the effective model and the original system, particularly for those corresponding to the flat bands, where vanishing oscillation amplitudes are located at identical positions within the domain walls.

3.2.3 Inhomogeneous mass model

While the effective model is able to reproduce the flat bands satisfactorily, we note that it does not capture well some band gaps in both triangular and honeycomb case.

Here, we show that these band gaps are reproducible by considering an inhomogeneous distribution of masses in the effective model. We assume that the

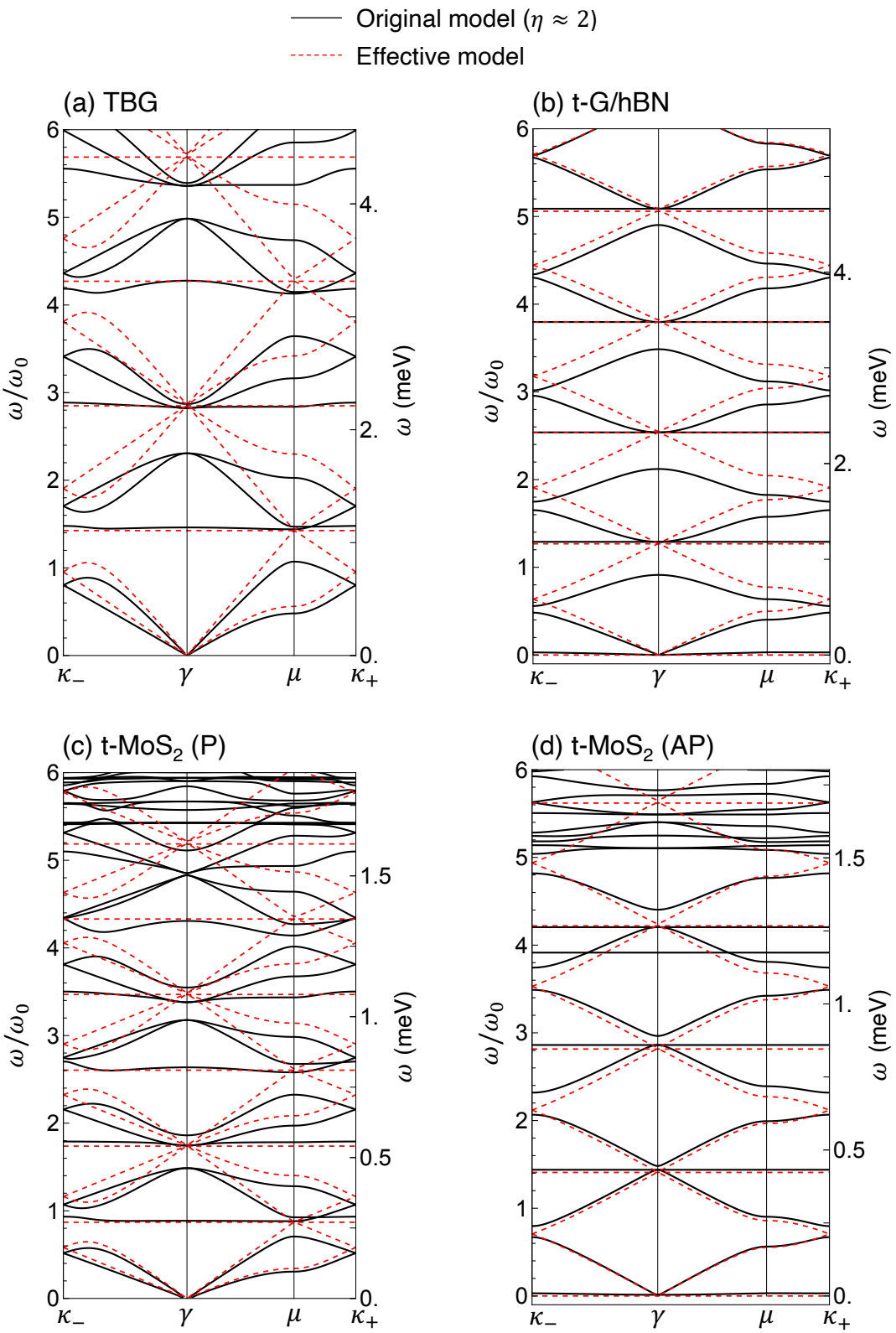

Figure 3.7: Phonon dispersion of the effective model (red-dashed line) and the original model (black line) of each considered twisted bilayer systems at the strong-coupling regime ($\eta \approx 2$).

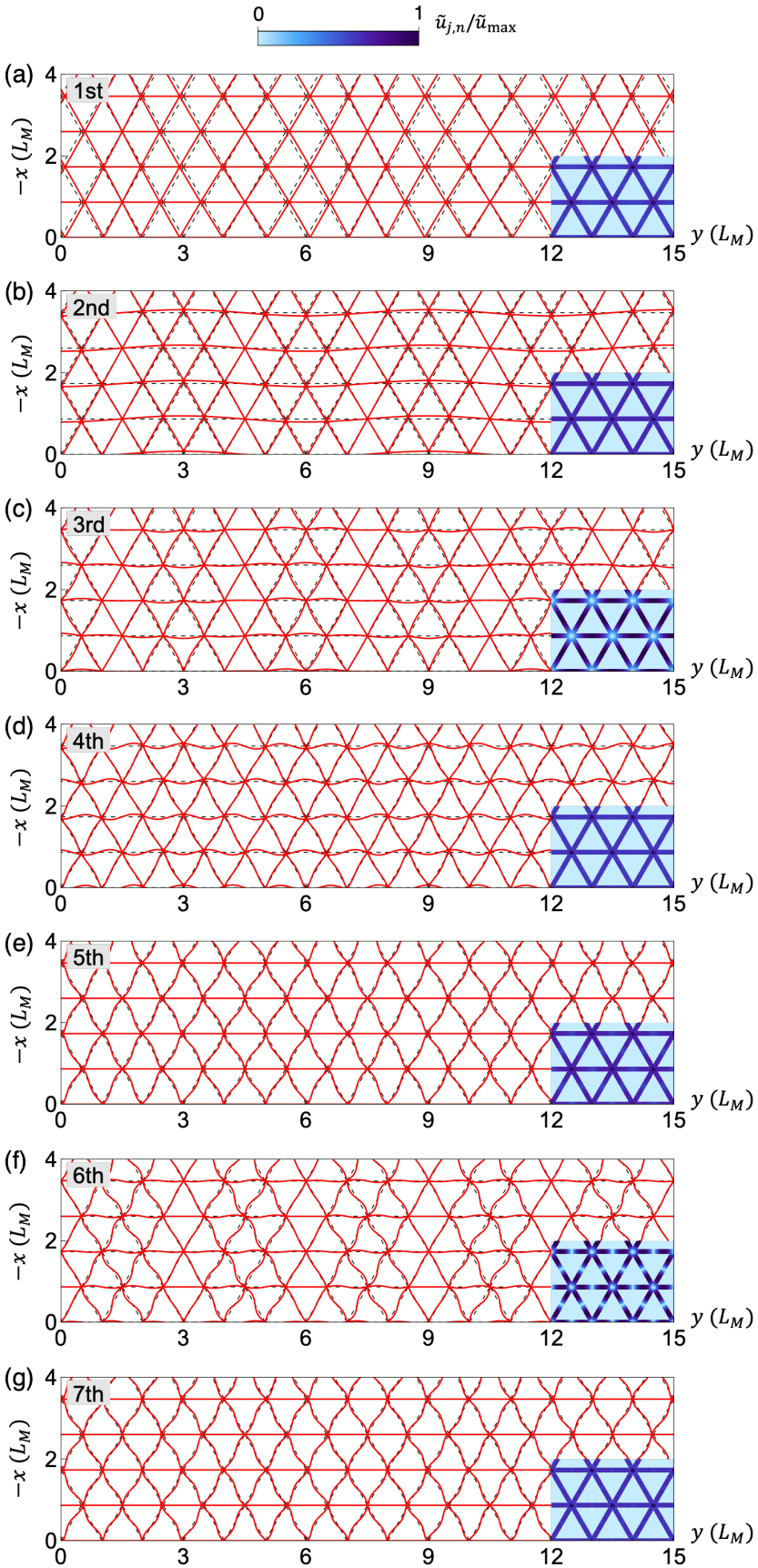

Figure 3.8: Phonon wave function of the first seven modes of the triangular effective model which correspond to the same wave vector and temporal snapshot of Fig. 3.2.

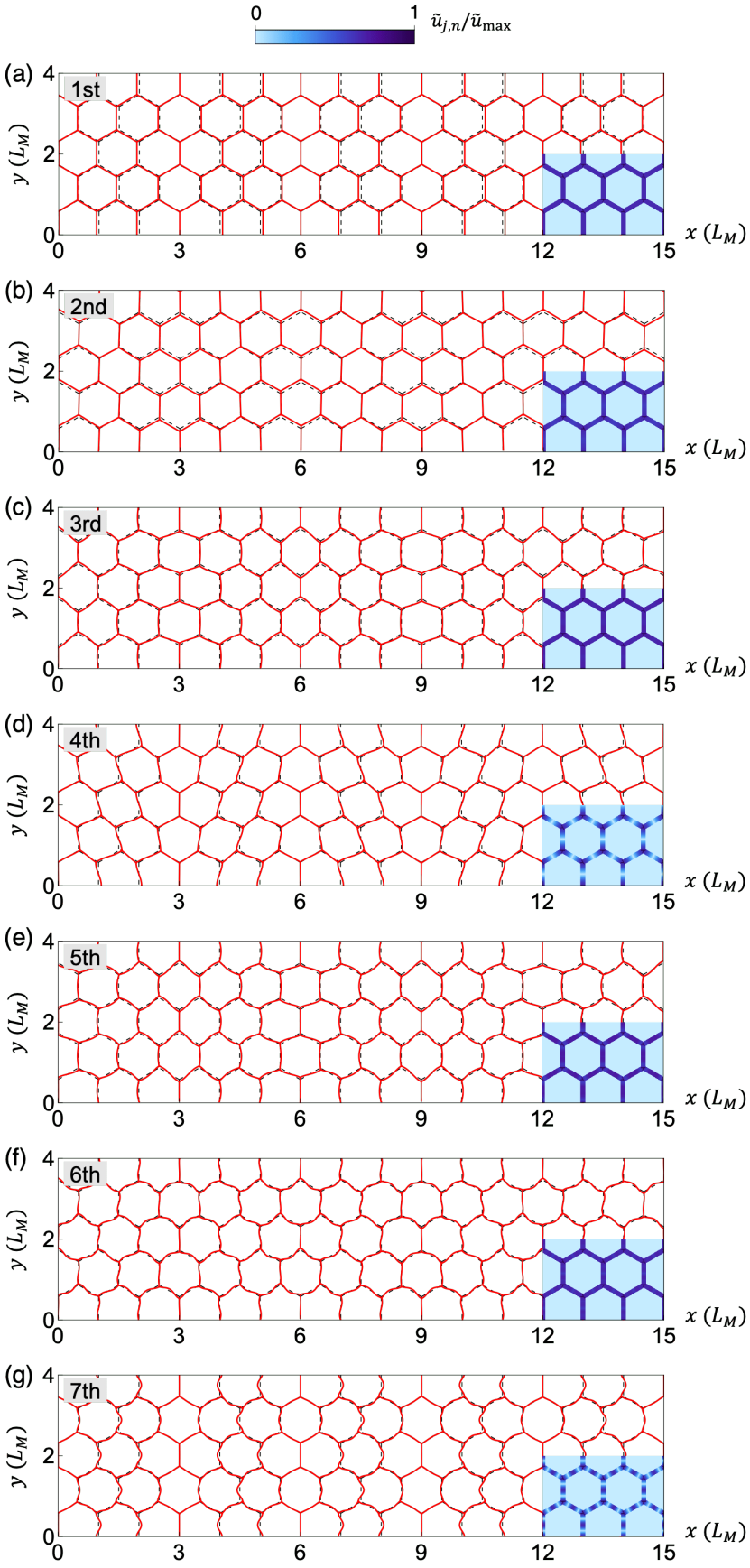

Figure 3.9: Phonon wave function of the first seven modes of the honeycomb effective model which correspond to the same wave vector and temporal snapshot of Fig. 3.4.

Table 3.1: List of parameters for the effective models with inhomogeneous mass distribution.

	α	b_0	b_1	b_2
TBG	24.2	2	0.019	0.019
t-G/hBN	8.12	1	-0.375	-0.390
t-MoS_2 (P)	19.4	2	0.020	0.020
t-MoS_2 (AP)	22.2	10	0.007	-0.050

mass at position $\mathbf{r}_{\mathbf{R}}^{(j,n)}$, is given by

$$m_n/M_0 = b_0 + f(n/N, b_1) + f(n/N - 1, b_2), \tag{3.12}$$

where $b_{i(=0,1,2)}$ is a fitting parameter, M_0 is a normalization factor such that $\sum_{n=0}^{N} m_n = (N+1)M$, and $f(x,b) = (b/\pi)/(x^2+b^2)$ is a decaying function with maximum at $x = 0$ and half maxima at $x = \pm b$. Figure 3.10 (a-d) compares the phonon dispersion of the effective model with the inhomogeneous mass distribution (red-dashed lines) and the original model (black lines) for each system. We find that a nearly perfect agreement can be achieved by considering a distribution of masses along a single segment ($n = 0, ..., N$) as given in the top-right inset within each panel. The corresponding values of b_i parameters that produce these distributions are given in Table 3.1. These values are determined by considering the nature of the band gaps which is explained as follows.

As an example, let us consider the third, fourth, and fifth phonon modes near the γ-point in the honeycomb model. In the t-G/hBN case, the fourth and fifth modes are degenerate at γ while the third mode is gapped at lower frequency. By observing the corresponding phonon wave functions [Fig. 3.4 (c-e)], we find that the oscillation pattern of the third mode can be clearly distinguished from that of the fourth and fifth modes. The vibrations in the former mode are concentrated within each domain wall segment whereas those in the latter modes are concentrated near the vertex positions. From the perspective of mass-bond model, this suggests that the masses in the center of each segment are heavier than those close to the end points. To reproduce the exact size of the gaps in

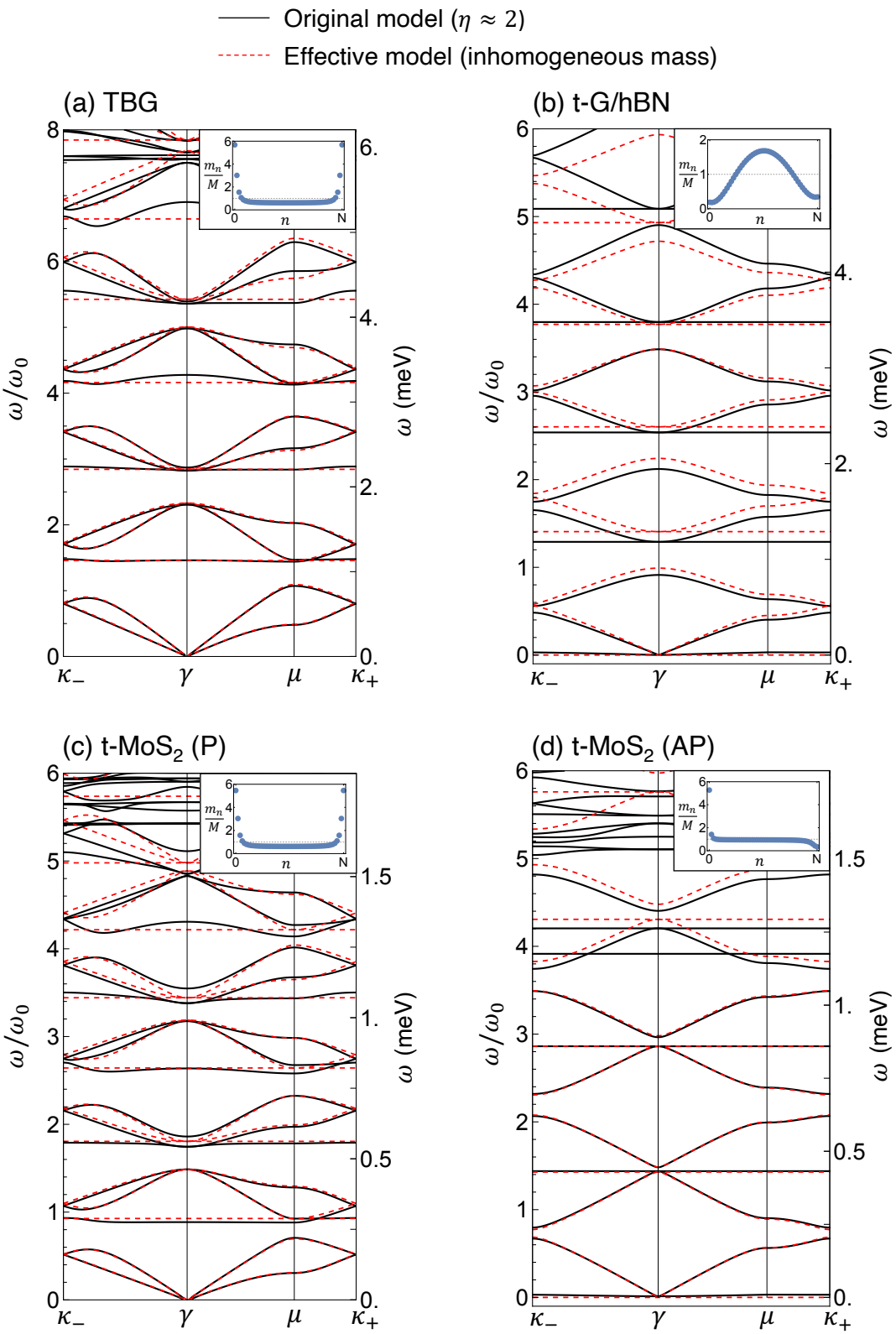

Figure 3.10: Phonon dispersion of the effective model with inhomogeneous mass assumption (red-dashed line) and the original model (black line). Inset in each panel shows the mass distribution for masses at $n = 0, ..., N$.

the model, we fine-tune the magnitude of b_1 and b_2 that tells the sharpness of the distribution gradient and the magnitude of b_0 which determines the ratio of the mass at the center and the ends of the segments.

Band gaps at γ in other systems are also reproduced using the same approach except those between the seventh and eighth mode in the triangular model which requires further introduction of an energy cost associated with rotational degree of freedom at the vertex points. Meanwhile, the gaps at the $\kappa_\pm$ points in the honeycomb case is particularly special, as it requires mass distribution that breaks the inversion symmetry, i.e., $b_1 \neq b_2$. We note that in the present case, we treat the b_i as phenomenological constants. In the actual systems, we expect that these corresponds to the inhomogeneity of binding and elastic energy across the domain walls. We left this rigorous treatment of the b_i parameters for future study.

3.3 Origin of flat bands

One striking feature in the phonon band structures of both triangular and honeycomb models are the presence of multiple flat bands. To consider the origin of these flat bands, we first consider the $N = 1$ case of the honeycomb effective model and obtain the analytical solution. Here, a unit cell contains masses only at $\mathcal{A}$ and $\mathcal{B}$, and hence the equation has only four degrees of freedom. The equation of motion is written as

$$M\omega^2 \begin{pmatrix} \mathbf{u}_\mathbf{q}^\mathcal{A} \\ \mathbf{u}_\mathbf{q}^\mathcal{B} \end{pmatrix} = K \sum_{j=1}^{3} \begin{pmatrix} \hat{T}_j & -\hat{T}_j e^{i\mathbf{q}\cdot\tau_j} \\ -\hat{T}_j e^{i\mathbf{q}\cdot\tau_j} & \hat{T}_j \end{pmatrix} \begin{pmatrix} \mathbf{u}_\mathbf{q}^\mathcal{A} \\ \mathbf{u}_\mathbf{q}^\mathcal{B} \end{pmatrix}, \tag{3.13}$$

where ω is the eigen frequency. The obtained phonon dispersion has a similar structure to the lowest four bands of $N = 20$ model, where flat bands appear in the first and fourth bands with eigen frequencies $\omega = 0, 3\sqrt{K/M}$, respectively.

The corresponding eigenstates are given by

$$\begin{pmatrix} \mathbf{u}_{\mathbf{q}}^{\mathcal{A}} \\ \mathbf{u}_{\mathbf{q}}^{\mathcal{B}} \end{pmatrix} = \begin{pmatrix} \mathbf{f}_{\mathbf{q}} \\ \mp \mathbf{f}_{\mathbf{q}}^{*} \end{pmatrix}, \tag{3.14}$$

respectively, where

$$\mathbf{f}_{\mathbf{q}} = \sum_{j=1}^{3} \boldsymbol{\tau}_j e^{-i\mathbf{q}\cdot\boldsymbol{\tau}_j}. \tag{3.15}$$

It is straightforward to check that Eq. (3.14) satisfies the eigen equation Eq. (3.13), by using the relation

$$\hat{T}_j \mathbf{f}_{\mathbf{q}} = -\hat{T}_j \mathbf{f}_{\mathbf{q}}^{*} e^{i\mathbf{q}\cdot\boldsymbol{\tau}_j}, \tag{3.16}$$

and $\sum_{j=1}^{3} \hat{T}_j = (3/2)I$, where I is a 2×2 unit matrix.

The expression of Eq. (3.14) leads to an important observation for the motion of the neighboring masses. Let us consider a pair of masses at $\mathcal{A}$ and $\mathcal{B}$ points separated by $\boldsymbol{\tau}_j$. According to Eq. (3.14), the motions of the two points are given by $\mathbf{u}^{\mathcal{A}}(\mathbf{R}) = C\mathbf{f}_{\mathbf{q}}$ and $\mathbf{u}^{\mathcal{B}}(\mathbf{R}+\boldsymbol{\tau}_j) = \mp C\mathbf{f}_{\mathbf{q}}^{*} e^{i\mathbf{q}\cdot\boldsymbol{\tau}_j}$, where C is a common constant. Using Eq. (3.16), we immediately have

$$\hat{T}_j \mathbf{u}^{\mathcal{A}}(\mathbf{R}) = \pm \hat{T}_j \mathbf{u}^{\mathcal{B}}(\mathbf{R}+\boldsymbol{\tau}_j), \tag{3.17}$$

for the first and fourth modes, respectively. Noting that $\hat{T}_j$ is the projection operator perpendicular to $\boldsymbol{\tau}_j$, we conclude that, in the flat band modes, the neighboring vertices $\mathcal{A}$ and $\mathcal{B}$ always move either in phase (the first mode) or out of phase (the fourth mode) when the motion is projected perpendicularly to the bond, regardless of the wave number.

Actually, this relationship holds for vertex-site motions of any flat band modes in $N \geq 1$ cases, where $3n+1$-th flat bands can be further associated with the in-phase motions ($6n+1$-th) and out-of-phase motions ($6n+4$-th), as illustrated in Fig. 3.11. The phase synchronization of the vertex sites means that masses in

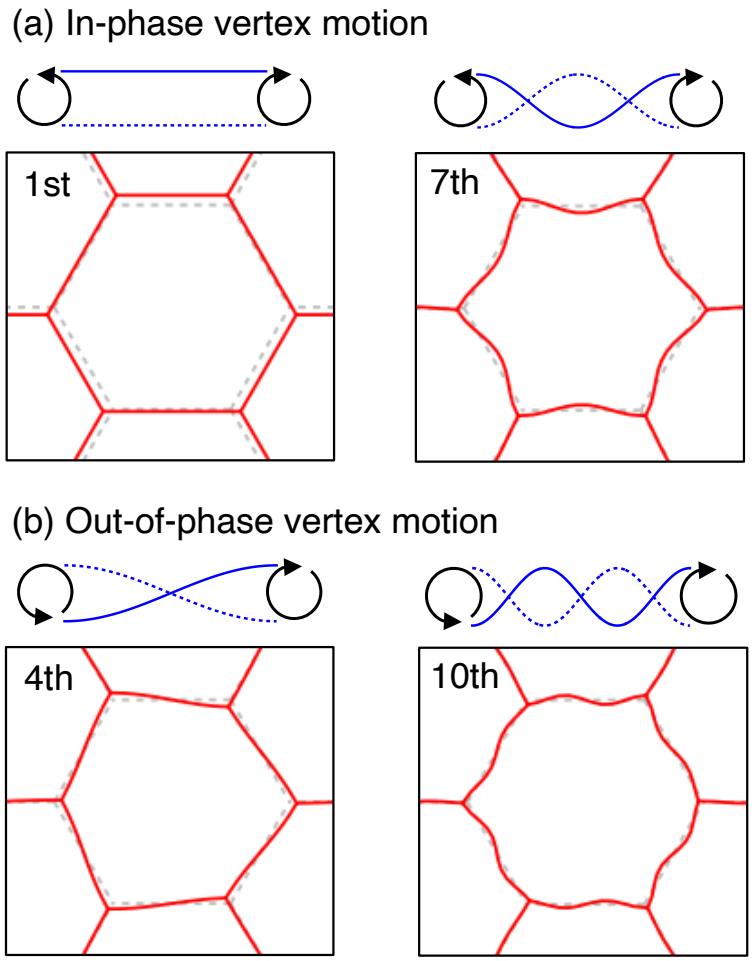

Figure 3.11: Phase synchronization for the perpendicular motion of neighboring vertices in the honeycomb effective model: (a) in-phase mode, and (b) out-of-phase mode. These corresponds to the two type of solutions in the vibration modes of string-like system with open boundary conditions.

each single chain can collectively vibrate as a stationary wave of an isolated string. Since the phase synchronization persists at any $\mathbf{q}$ as shown above, this gives a flat dispersion at the frequency of the corresponding fundamental mode of the string. The vertex motions parallel to bonds are not generally synchronized, but they are irrelevant for the band flatness because the contributions of the parallel shifts to the total bond length cancel as a whole, and do not change the total energy. Here note that the energy of an effective bond is linearly proportional to its length as argued above.

Meanwhile, for the triangular case, the absence of sublattice degree of freedom prevent the phase synchonization of neighboring vertices at any finite wave-vector

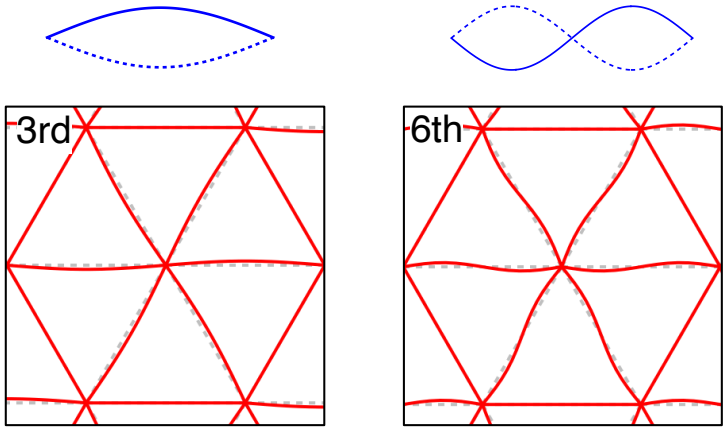

Figure 3.12: The two lowest fundamental oscillation modes in the string-like system with closed boundary conditions. The corresponding oscillation in the effective triangular model are also given, representing the wave function of the lowest two flat bands at the κ_+ point.

q. Therefore, the only way it can hosts a localized oscillation along the domain walls is by having a similar oscillation pattern resembling the stationary waves of isolated string with *closed boundary conditions*. This is contrary to the honeycomb lattice case, where the oscillation modes corresponding to the flat bands can be viewed as stationary waves of isolated string with *open boundary conditions*. Therefore, the oscillation pattern that corresponds to the flat bands of triangular lattice are characterized by nodes at the vertices, followed by additional nodes at equidistant positions along the domain walls for each subsequent fundamental mode. These type of nodes are clearly observed in the spatial distribution of the oscillation amplitudes of atomic vibrations in TBG [Fig. 3.2(c) and (f)] as well as the oscillation of the masses in the effective model [Fig. 3.8(c) and (f)]. The first two fundamental modes of such oscillations are illustrated in Fig. 3.12. Here the corresponding oscillations in the effective triangular lattice are taken from the third and sixth band at the κ_+ point.

A notable feature in the phonon band structure in the effective honeycomb lattices like t-G/hBN and antiparallel t-MoS_2 is the existence of a flat band at zero frequency. The complete flattening of the lowest branch implies that

the regular honeycomb array is unstable against expansion/contractions of the hexagonal unit cell. This can be understood by noting that we can modify a regular honeycomb array into an irregular pattern without a change in the total length of the domain wall (and hence the total energy), by expanding/shrinking hexagons with the orientation of sides (domain walls) kept unchanged. This situation is quite similar to solid phases of adsorbed atoms on a graphite surface, where the commensurate domain wall formation was discussed [149]. In the reality, the lowest band is not completely flat as seen in Figs. 4.3 and 3.5, and therefore the regular honeycomb superlattice is energetically stable. Within the effective model, the finite dispersion of the lowest band could be incorporated by adding vertex-vertex interaction energy in the effective model. The flat zero mode does not appear in the triangular lattices as it is impossible to introduce any distortion without changing the total side length.

3.4 Phonon angular momentum

In a system without inversion symmetry, the phonons generally acquire a chiral nature with finite angular momentum and the Berry curvature [150, 55, 51]. In the current system, the inversion symmetry breaking enters as difference in local binding energy of stacking configurations located at opposite positions, e.g., AB/BA in t-G/hBN and antiparallel t-MoS_2. The existence of chiral phonons in the antiparallel stacking of t-MoS_2 has been investigated by Suri, et al. [55]. To clarify the existence of chiral phonons in t-G/hBN, we calculate the out-of-plane component of angular momentum defined as [151, 55]

$$L^z = \rho \int d^2\mathbf{r} \sum_{l=1}^{2} \left(\delta\mathbf{u}^{(l)} \times \delta\dot{\mathbf{u}}^{(l)} \right)_z , \tag{3.18}$$

where $l(=1,2)$ is the layer index and $\delta\mathbf{u}^{(l)}(\mathbf{r},t)$ is the displacement vector of layer $l=1,2$.

By using the Fourier transformation of the displacement vector [Eq. 2.21] and

the relation $\delta\mathbf{u}^{(2)} = -\delta\mathbf{u}^{(1)} = (1/2)\delta\mathbf{u}^{-}$, we can rewrite Eq. (3.18) as,

$$L^z = \sum_{\mathbf{q}} \sum_{\mathbf{G}} \left(\delta\mathbf{u}^{-}_{\mathbf{q}+\mathbf{G}} \times \delta\mathbf{p}^{-}_{\mathbf{q}+\mathbf{G}}\right)_z, \tag{3.19}$$

where $\delta\mathbf{p}^{-}_{\mathbf{q}} = \rho_r \delta\dot{\mathbf{u}}^{-}_{-\mathbf{q}}$. In terms of phonon creation and annihilation operators, $\delta\mathbf{u}^{-}_{\mathbf{q}+\mathbf{G}}$ and $\delta\mathbf{p}^{-}_{\mathbf{q}+\mathbf{G}}$ are written as [111],

$$\begin{aligned}
\delta\mathbf{u}^{-}_{\mathbf{q}+\mathbf{G}} &= \sum_{n} \mathbf{C}_{n,\mathbf{q}}(\mathbf{G}) \sqrt{\frac{\hbar}{2\rho_r \omega_{n,\mathbf{q}}}} (a_{n,\mathbf{q}} + a^{\dagger}_{n,-\mathbf{q}}), \\
\delta\mathbf{p}^{-}_{\mathbf{q}+\mathbf{G}} &= \sum_{n} i\mathbf{C}^{*}_{n,\mathbf{q}}(\mathbf{G}) \sqrt{\frac{\hbar\rho_r \omega_{n,\mathbf{q}}}{2}} (a^{\dagger}_{n,\mathbf{q}} - a_{n,-\mathbf{q}}),
\end{aligned} \tag{3.20}$$

where $\mathbf{C}_{n,\mathbf{q}}(\mathbf{G})$ is the normalized eigenvector of Eq. (2.25). Substituting these into Eq. 3.19, we have

$$\begin{aligned}
L^z = \frac{i\hbar}{2} \sum_{\mathbf{q},\mathbf{G}} \sum_{n,n'} \sqrt{\frac{\omega_{n',\mathbf{q}}}{\omega_{n,\mathbf{q}}}} \left[\mathbf{C}_{n,\mathbf{q}}(\mathbf{G}) \times \mathbf{C}^{*}_{n',\mathbf{q}}(\mathbf{G})\right]_z \\
\times (a_{n,\mathbf{q}} + a^{\dagger}_{n,-\mathbf{q}})(a^{\dagger}_{n,\mathbf{q}} - a_{n,-\mathbf{q}}).
\end{aligned} \tag{3.21}$$

Finally, the expectation value in equilibrium is written as

$$\langle L^z \rangle = \sum_{n,\mathbf{q}} L^z_{n,\mathbf{q}} \left[f(\omega_{n,\mathbf{q}}) + \frac{1}{2} \right], \tag{3.22}$$

where

$$L^z_{n,\mathbf{q}} = i\hbar \sum_{\mathbf{G}} \mathbf{C}_{n,\mathbf{q}}(\mathbf{G}) \times \mathbf{C}^{*}_{n,\mathbf{q}}(\mathbf{G}), \tag{3.23}$$

and $f(\omega) = 1/(\exp(\hbar\omega/k_B T) - 1)$ is the Bose-Einstein distribution function, and we note that $\langle a^{\dagger}_{n,\mathbf{q}} a_{n',\mathbf{q}'} \rangle = f(\omega_{n,\mathbf{q}})\delta_{n,n'}\delta_{\mathbf{q},\mathbf{q}'}$, $\langle a_{n,\mathbf{q}} a_{n',\mathbf{q}'} \rangle = \langle a^{\dagger}_{n,\mathbf{q}} a^{\dagger}_{n',\mathbf{q}'} \rangle = 0$, and $\omega_{n,\mathbf{q}} = \omega_{n,-\mathbf{q}}$.

Figure 3.13 shows the k-space distribution of the angular momentum $L^z_{n,\mathbf{q}}$ for the lowest six bands in 0°-stack of G/hBN. We observe relatively large amplitudes

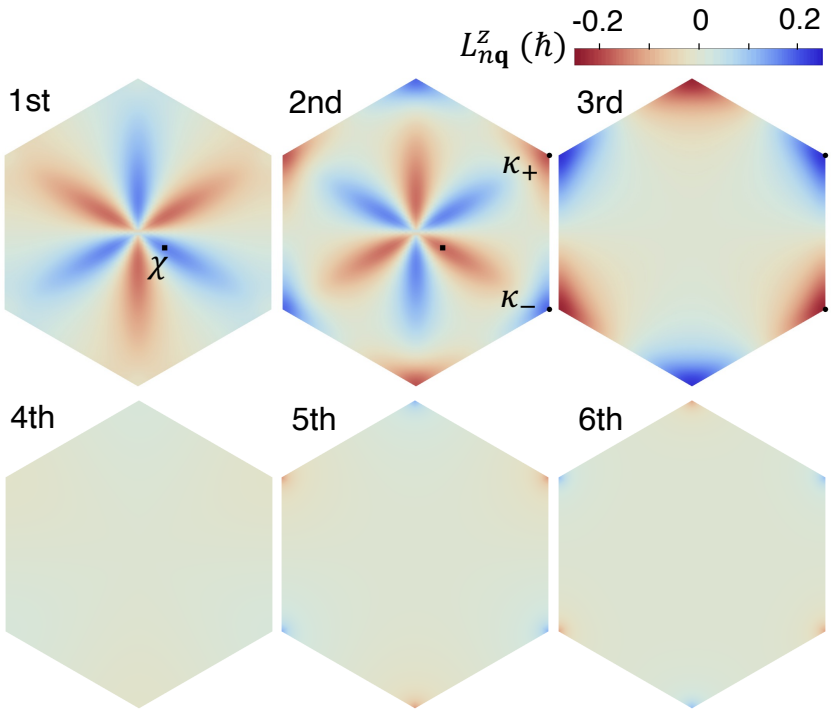

Figure 3.13: Angular momentum for the lowest sixth bands of 0° G/hBN within the MBZ.

with opposite signs in the second and third bands around the BZ corner $\kappa_\pm$. This corresponds to a gap opening caused by the inversion symmetry breaking [$\Delta_{23}^{\kappa_-}$, Fig. 3.14(a)]. In the fourth to sixth bands, notable angular momentum is observed only in the close vicinity of $\kappa_\pm$, in accordance with very small symmetry-breaking gaps in the phonon band structure.

Figure 3.14(c) shows the twist-angle dependence of the angular momentum $L^z_{n,\mathbf{q}}$ of the second and the third bands at κ_-. The corresponding plot for the gap width $\Delta_{23}^{\kappa_-}$ is shown in Fig. 3.14(b). We observe that the angular momenta of these two bands are swapped when the gap closes at $\theta \sim 0.3°$. The absolute values peak at $\sim$2° and monotonically decrease in larger twist angles, as shown in the inset of Fig. 3.14(c).

In Fig. 3.13, we also observe notable signals of angular momentum in the two lowest bands around lines connecting γ and the $\kappa_\pm$ points. This can be attributed to a tiny energy distance between the two bands, where perturbative matrix elements of the symmetry breaking terms give rise to sizable angular

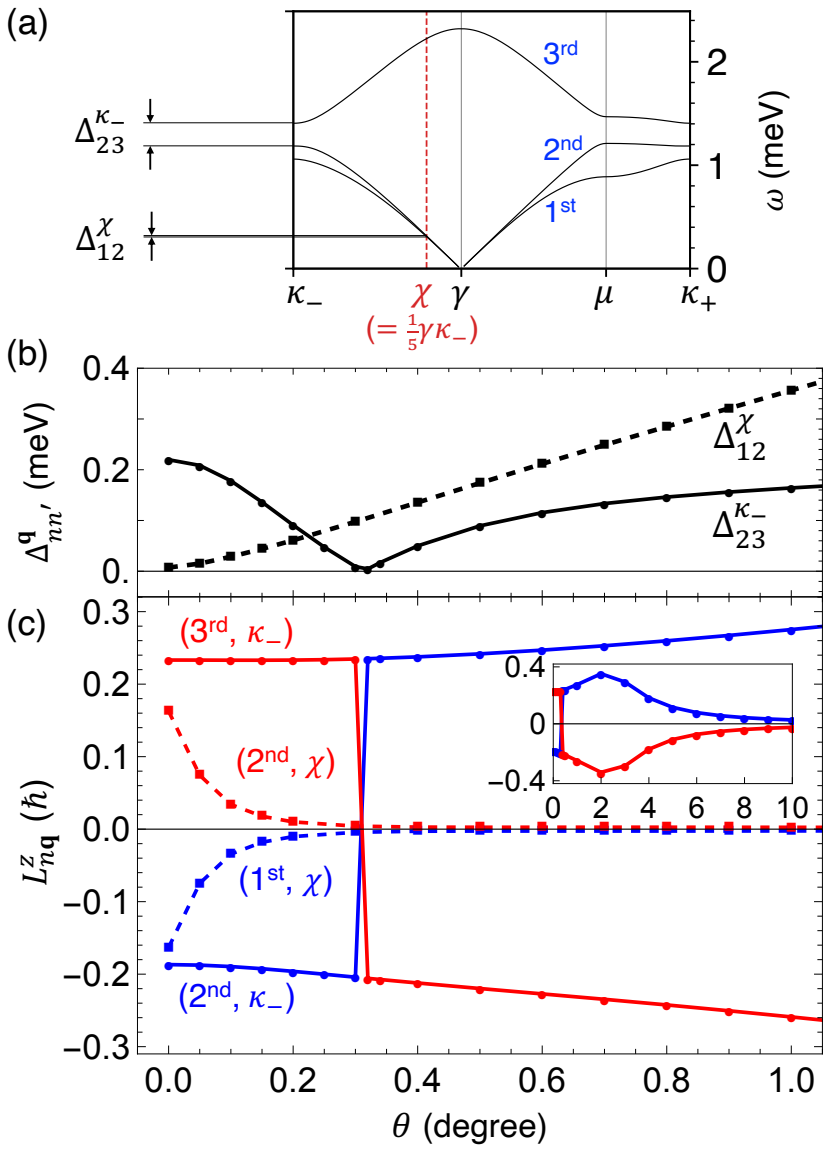

Figure 3.14: (a) Dispersion of the lowest three bands of 0° G/hBN. (b) Twist angle dependence of gap width ($\Delta_{nn'}^{\mathbf{q}}$) between the n-th and n'-th band at $\mathbf{q}$. χ is taken as $\frac{1}{5}\gamma\kappa_-$. (c) Twist angle dependence of the angular momenta for each corresponding bands involved in (b) with inset showing larger range of angle up to $\theta = 10°$.

momentum by hybridizing these nearly-degenerate bands. We present the twist angle dependence of the angular momentum of the first and the second bands at $\chi \equiv (1/5)\gamma\kappa_-$ in Fig. 3.14(c), and also the corresponding plot of the energy distance Δ_{12}^{χ} between the two bands at χ in Fig. 3.14(b). In increasing the twist angle from 0, the Δ_{12}^{χ} become rapidly increases, and their angular momenta immediately vanish correspondingly.

Chapter 4

Low-temperature thermal transport in bilayer moiré superlattices

In this chapter, we discuss how the moiré effect on the low-frequency phonon properties of twisted bilayer systems are reflected in the thermal transport phenomena. In Sec. 4.1, we describe the formulation of thermal transport theory within the semiclassical picture and the constant mean free path assumption. In Sec. 4.2, we show the calculated thermal conductivity for various representative moiré superlattices and demonstrate the reduction of thermal conductivity and changes in the temperature-dependence due to the moiré effect.

4.1 Thermal transport theory

Based on linearized Boltzmann transport theory with relaxation time approximation [152], thermal conductivity of 2D isotropic material can be expressed as

$$\kappa = \frac{1}{S}\sum_{n,\mathbf{q}} \frac{1}{2} v_{n,\mathbf{q}}^2 \tau_{n,\mathbf{q}} \hbar\omega_{n,\mathbf{q}} \frac{\partial f_0(\omega_{n,\mathbf{q}})}{\partial T}, \tag{4.1}$$

where S is the total area of the system, $f_0(\omega) = 1/[\exp(\hbar\omega/k_B T) - 1]$ is the Bose-Einstein distribution function, $v_{n,\mathbf{q}} = |\boldsymbol{\nabla}_{\mathbf{q}}\omega_{n,\mathbf{q}}|$ is the phonon velocity, $\tau_{n,\mathbf{q}}$ is the relaxation time, and the summation is taken over all of the mode index n and wave vector $\mathbf{q}$. Here, we note that the isotropic behavior is a consequence of the three-fold rotation symmetry.

The relaxation time, $\tau_{n,\mathbf{q}}$, describes various scattering mechanisms that limit the mean free path of the phonon which is defined as $\Lambda_{n,\mathbf{q}} \equiv \tau_{n,\mathbf{q}} v_{n,\mathbf{q}}$. At low tem-

perature, scattering due to geometric boundary is the dominant scattering mechanism and the mean free path no longer depends on the phonons frequency and wavelength, i.e., $\Lambda_{n,\mathbf{q}} = \Lambda$ (constant) [152]. For example, in graphitic systems, Λ is determined from the size and shape of the sample or the grain boundaries, and it well describes the thermal conductivity for up to 100 K [153, 154, 155]. In moiré systems, the superlattice period is generally observed to be varying across a single sample [156, 157] and this would disrupt the propagation of phonon modes [148]. In such a case, Λ can be regarded as a typical length where the moiré pattern remains uniform. Henceforth, we treat Λ as a phenomenological constant to be determined from direct measurements. The thermal conductivity is then entirely governed by the harmonic properties, and it can be written as

$$\kappa = \frac{\Lambda}{2} \int_0^\infty \tilde{n}(\omega) C(\omega, T) d\omega, \tag{4.2}$$

where velocity-weighted density of states (VDOS) $\tilde{n}$ is defined as

$$\tilde{n}(\omega) = \frac{1}{S} \sum_{n,\mathbf{q}} \delta(\omega - \omega_{n,\mathbf{q}}) v_{n,\mathbf{q}} \tag{4.3}$$

and spectral heat capacity C is defined as

$$C(\omega, T) = \hbar\omega \frac{\partial f_0(\omega)}{\partial T} = k_B \left[\frac{\beta\hbar\omega/2}{\sinh(\beta\hbar\omega/2)} \right]^2, \tag{4.4}$$

where $\beta = 1/(k_B T)$. In Eq. (4.2), $\tilde{n}(\omega)$ contains all information regarding the phonon dispersion while $C(\omega, T)$ acts as a weight function. The function $C(\omega, T)$ is plotted in Fig. 4.1; it equals to k_B when $\omega = 0$, and decays exponentially for $\hbar\omega \gtrsim 2k_B T$. In general, the summation over mode index n would include both in-plane and out-of-plane (flexural) phonon modes. However, scattering due to substrate or other layers significantly reduces the mean free path of the flexural mode [129, 130, 131, 132, 133, 134], hence, its contribution to thermal conductivity especially at low temperatures [128]. Hereafter, we will focus only

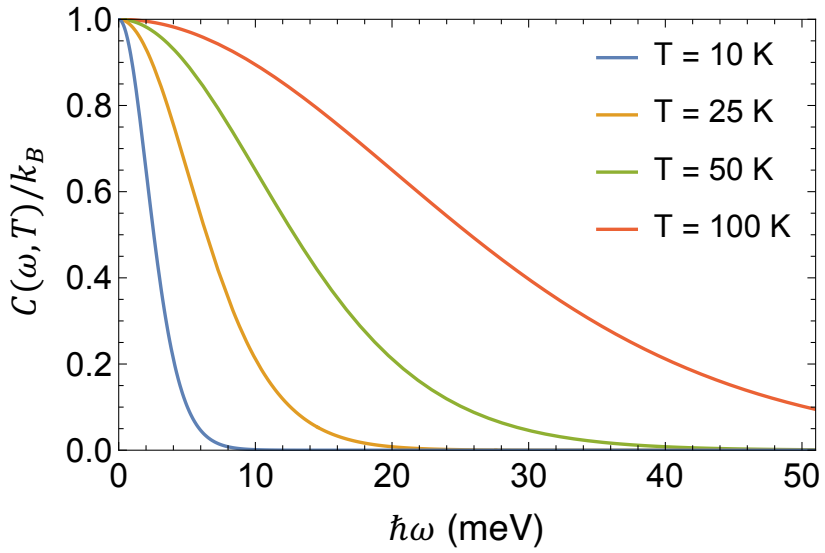

Figure 4.1: Plot of the spectral heat capacity function $C(\omega, T)$ [Eq. (4.4)] as a function of phonon energy at different temperatures.

on the in-plane modes contribution in the thermal conductivity.

Since only the antisymmetric phonon modes are strongly affected by the interlayer moiré potential, it is useful to write κ and $\tilde{n}$ in terms of the symmetric and antisymmetric components

$$\kappa = \kappa^+ + \kappa^-, \quad \tilde{n} = \tilde{n}^+ + \tilde{n}^-, \tag{4.5}$$

which takes the contribution from the symmetric (+) and antisymmetric (−) phonon modes separately. In the absence of the interlayer moiré coupling (i.e., two independent monolayers), they are given as

$$\tilde{n}^+_{\rm NC} = \tilde{n}^-_{\rm NC} = \tfrac{1}{2}\tilde{n}_{\rm NC} = \frac{\omega}{2\pi\bar{v}}, \tag{4.6}$$

$$\kappa^+_{\rm NC} = \kappa^-_{\rm NC} = \tfrac{1}{2}\kappa_{\rm NC} = \frac{3\Lambda\zeta(3)}{2\pi\hbar^2\bar{v}}k_B^3T^2, \tag{4.7}$$

where $\bar{v}^{-1} = v_{\rm L}^{-1} + v_{\rm T}^{-1}$, $\zeta(n)$ is the Riemann zeta function, and NC stands for 'non-coupled'. Here, we note that we have neglected the out-of-plane (flexural) phonon modes in the calculation of thermal conductivity. The quadratic temperature dependence of the thermal conductivity is a characteristic of linear acoustic phonon-dominated thermal transport of 2D systems in the low-temperature

regime [128].

4.2 Thermal conductivity

4.2.1 TBG and twisted graphene/hexagonal boron nitride

Figure 4.2 shows the calculated band dispersion and density of states for antisymmetric phonon modes in TBG with $\theta = 5°$, $2.65°$ and $0.817°$. Figure 4.3 presents similar plots for t-G/hBN with $\theta = 5°$, $3°$, and $0°$. The phonon dispersion is plotted along the high-symmetry line in the moiré Brillouin zone (MBZ) as illustrated in Fig. 2.1(c). In each panel, the red-dashed line indicate the dispersion (only the lowest two branches shown) and the density of states in the non-coupled case. Here we can see that the interlayer coupling significantly modifies the band structure of the antisymmetric modes in the energy range below $\sim$20 meV. This reconstruction is characterized by sharp peaks in the density of states which results from the flattening of superlattice phonon bands [45, 55, 56, 53]. As the twist angle is reduced towards 0, the number of sharp peaks increases dramatically. On the other hand, the phonon bands of the symmetric phonon modes are not affected by the moiré interlayer coupling, hence they are equivalent to those of the non-coupled case (red-dashed lines).

To provide a more comprehensive understanding of the band flattening effects, we present two-dimensional density maps in Fig. 4.2(d)-(f) and Fig. 4.3(d)-(f), which plot the distribution of antisymmetric phonon modes on a space of frequency and velocity, or

$$D(\omega, v) = \sum_{n,\mathbf{q}} \delta(\omega - \omega_{n,\mathbf{q}})\delta(v - v_{n,\mathbf{q}}). \tag{4.8}$$

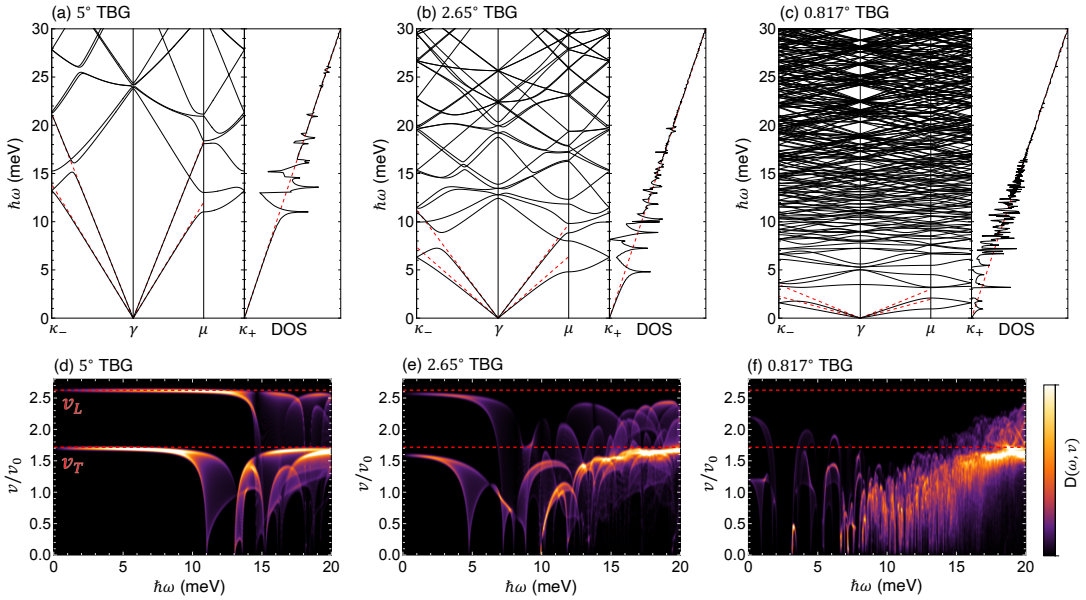

Figure 4.2: Band structure of the interlayer antisymmetric phonon modes (black line) and the symmetric modes (red-dashed line) for (a) 5°, (b) 2.65°, (c) 0.817° TBG. The right panel plots the density of states. (d)-(f) Corresponding plots for $D(\omega, v)$, the density of states on the frequency-velocity space [see, Eq. (4.8)].

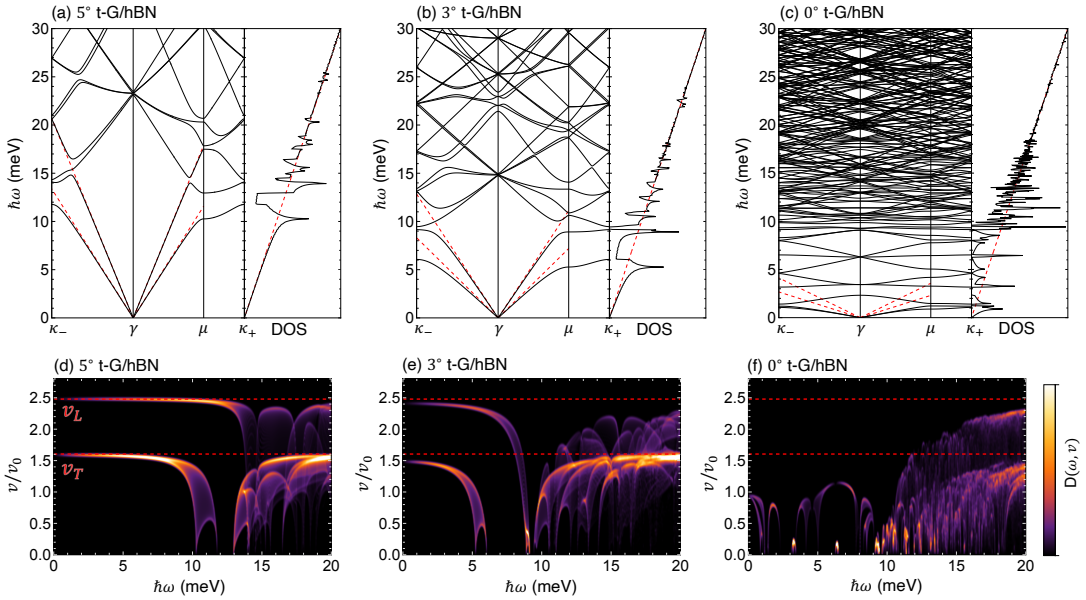

Figure 4.3: Plots of the band structure and $D(\omega, v)$ similar to Fig. 4.2, for t-G/hBN with $\theta = 5°$, $3°$, $0°$.

In each panel, the vertical axis is scaled by a factor of

$$v_0 = \sqrt{\lambda/\rho} \tag{4.9}$$

and the color brightness is a linear scale of $D(\omega, v)$. The horizontal red-dashed lines correspond to the velocity of the TA (v_{T}) and LA (v_{L}) phonons of a single layer [Eq. (2.13)]. Here, the flattening of phonon bands can be immediately seen as a distribution of phonon modes below v_{T} and v_{L}. In 0.817° TBG [Fig. 4.2(f)] and 0° t-G/hBN [Fig. 4.3(f)], particularly, the signals in $\hbar\omega < 15$ meV predominantly falls below the line of v_{T}, i.e., nearly all of the low-energy antisymmetric phonons become slower than the original acoustic phonons in its non-moiré counterpart. Note that the distribution of symmetric phonon states (not shown) sticks to the v_L and v_T lines, where the intensity increases linearly with energy.

Figure 4.4(a) and (b) show $\tilde{n}^-(\omega)$ (the VDOS of the antisymmetric phonon modes) of TBG and t-G/hBN, respectively, with various small twist angles. The effect of the moiré coupling is observed as a difference from a black-dashed line, which represents $\tilde{n}^+_{\mathrm{NC}} = \tilde{n}^-_{\mathrm{NC}} \propto \omega$ [Eq. (4.6)]. While VDOS is proportional to both phonon density of states and velocity, we find that the reduction of phonon velocity is more significant than the sharpening of density of states, leading to a suppression of $\tilde{n}^-$ over a wide range of phonon frequency. We also find that the linear behavior of $\tilde{n}^-$ remains in the low frequency region, which corresponds to the linear dispersion in the the lowest moiré phonon band in $\omega < \omega_{\mathrm{edge}} \approx 2\pi v_0/L_{\mathrm{M}}$. For the symmetric phonon modes (not shown), we have $\tilde{n}^+(\omega) = \tilde{n}^{\pm}_{\mathrm{NC}}(\omega)$, because they are not influenced by the moiré coupling.

Figure 4.5(a) and (b) summarise the calculated thermal conductivity $\kappa(T)(= \kappa^+ + \kappa^-)$ of TBG and t-G/hBN, respectively. In each figure, the left panel shows a log-log plot of $\kappa(T)$ for $2 < T < 100$ K. Here the vertical axis is scaled by the constant mean-free-path length Λ, which is assumed to be independent of temperature. The colored lines correspond to different twist angles. The black-dashed line represents the non-coupled bilayer case, κ_{NC}, which is proportional

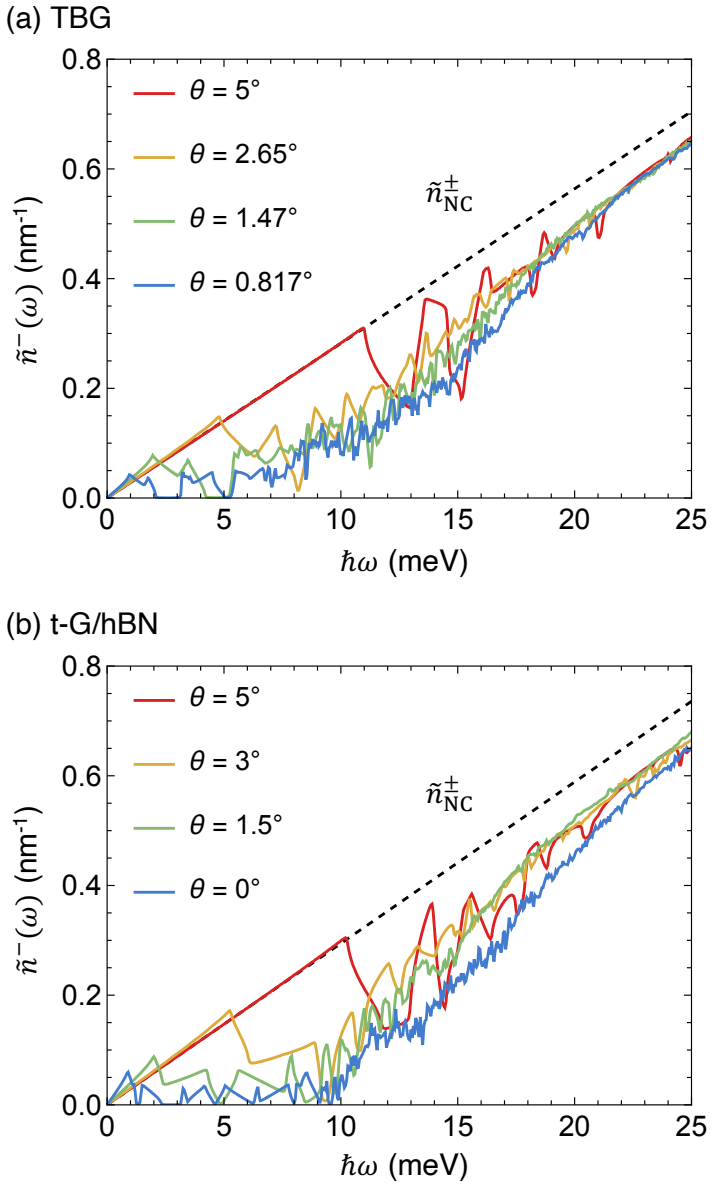

Figure 4.4: (a) Velocity-weighted density of states (VDOS) of the antisymmetric modes, $\tilde{n}^{-}(\omega)$, in TBGs with various twist angles. Black dashed lines represents $\tilde{n}^{+}_{\mathrm{NC}} = \tilde{n}^{-}_{\mathrm{NC}}$ for a non-coupled bilayer [Eq. (4.6)]. The VDOS for symmetric phonons $\tilde{n}^{+}$ is equal to $\tilde{n}^{\pm}_{\mathrm{NC}}$. (b) Similar plots for t-G/hBN.

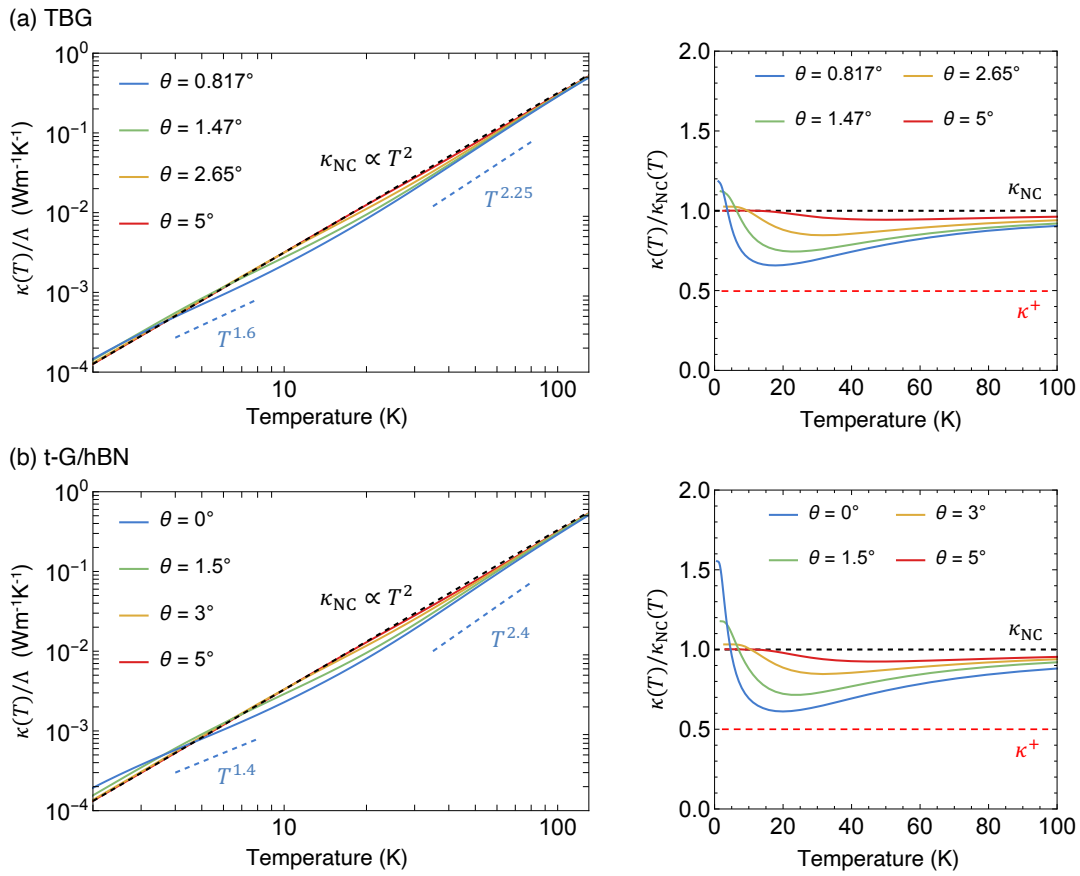

Figure 4.5: (a) Thermal conductivity in TBGs with various twist angles. The left panel shows the thermal conductivity $\kappa(T)$ scaled by the mean free path Λ. The right panel shows the relative thermal conductivity to the non-coupled bilayer case, $\kappa_{\mathrm{NC}}(T)$ [Eq. (4.7)]. (b) Similar plots for t-G/hBN.

to T^2 as given in Eq. (4.7). Here, we find that thermal conductivity is suppressed from the non-coupled case, notably around 20 K, while it converges towards the non-coupled value as increasing temperatures.

To better understand the change from the intrinsic graphene, we plot the relative thermal conductivity, $\kappa(T)/\kappa_{\mathrm{NC}}(T)$, in the right panel of Fig. 4.5(a) and (b). Here, suppression of thermal conductivity is represented by a value below unity. We can see that the suppression occurs over a wide temperature range except near the low-temperature limit. This suppression becomes more pronounced as the twist angle is smaller, where the largest reduction of up to ∼35% for 0.817° TBG and up to ∼40% for 0° t-G/hBN takes place at around 20 K. This can be understood since at around 20 K, heat transport is carried by phonons with energy below ∼20 meV [see Fig. 4.1], where the moiré effect on the asymmetric

modes are the most notable, as shown by the changes in VDOS [Fig. 4.4]. There, thermal conductivity is almost entirely came from the symmetric phonon modes, $\kappa^+ = \kappa_{\rm NC}/2$ (red-dashed line).

In the zero-temperature limit, we observe that the relative thermal conductivity $\kappa/\kappa_{\rm NC}$ rapidly rises and even exceeds 1, indicating that the thermal transport is *enhanced* by the moiré effect. The reason for this phenomenon is explained as follows. Within this temperature range, only phonons in the two lowest moiré phonon bands in $\omega < \omega_{\rm edge}$ become relevant in the thermal transport equation. These phonon modes have a linear dispersion, where the VDOS is given by $\omega/(2\pi v)$ with the corresponding group velocity v [Eq. (4.6) for the noncoupled case]. Since the velocities of the antisymmetric phonon modes are significantly reduced by the moiré effects [see Fig. 4.2 and Fig. 4.3], the inverse relation leads to an enhancement of the VDOS, and hence of the thermal conductivity. In decreasing the twist angle, these phonon velocities are monotonically decreased, and eventually converges towards a finite value in the small angle limit [45, 108]. This sets the upper bound of the relative thermal conductivity in the $T \to 0$ limit.

We also find that the overall modifications of the thermal conductivity by the moiré effect results in a change of the power coefficient α in $\kappa(T) \propto T^\alpha$, as seen from the logarithmic plot in the left panel of Fig. 4.5(a) and (b). In the absence of moiré interlayer coupling, thermal conductivity has quadratic temperature dependence ($\alpha = 2$), which comes from the linear dispersion of the original acoustic phonons. However, the enhancement in the low T limit and the subsequent suppression in higher T decrease the power coefficient from 2. For example, it is given by $\alpha \approx 1.6$ in 0.817° TBG and $\alpha \approx 1.4$ in 0° t-G/hBN within the temperature range of 4 K to 8 K. As temperature increases further, moiré effect starts to fade out and thermal conductivity returns towards the original value. This requires the power coefficient to be larger than 2. For example, it is given by $\alpha \approx 2.25$ for 0.817° TBG and $\alpha \approx 2.4$ for 0° for t-G/hBN which occurs in the range from 35

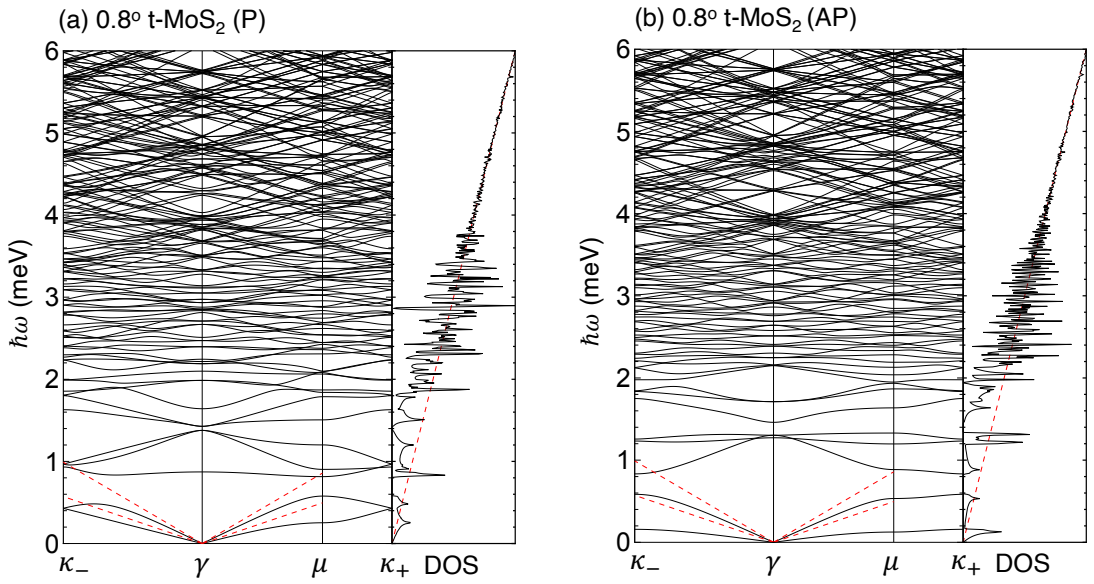

Figure 4.6: Phonon dispersion and density of states of the antisymmetric modes (black line) and the symmetric modes (red-dashed line) for (a) parallel-stacked (P) and (b) antiparallel-stacked (AP) 0.8° t-MoS_2.

K to 80 K.

4.2.2 Twisted bilayer molybdenum disulfide

The calculated phonon dispersion for t-MoS_2 is shown in Fig. 4.6 for both parallel and antiparallel stacking case with twist angle 0.8°. We find that the antisymmetric phonon modes of the parallel-stacked case closely resembles that of TBG [Fig. 4.2(c)]. This similarity occurs because TBG and t-MoS_2 share triangular domain wall structures [see Fig. 2.2(a) and (c)]. In an analogous way, the phonon band structure of the antiparallel t-MoS_2 resembles those of t-G/hBN, reflecting a common honeycomb domain-wall structure [Fig. 2.2(b) and (d)]. This is a natural result because the moiré phonon band structure is qualitatively reproduced by an effective mass-spring model for domain-wall motion [56], and hence it is primarily determined by the geometical structure of domain walls (triangular or honeycomb). We also observe that the characteristic energy scale of the moiré phonon bands in t-MoS_2 is much smaller than in TBG and t-G/hBN, because the original acoustic phonon velocity in MoS_2 is much lower than that of graphene and hBN.

In Fig. 4.7, we plot the calculated thermal conductivity of t-MoS_2 (P and AP) in a parallel manner to the TBG and t-G/hBN case. Here we find an overall reduction of thermal conductivity and the enhancement near $T \to 0$ just as in TBG and t-G/hBN. However, the characteristic temperature range is much lower than TBG and t-G/hBN because of the smaller energy scale of the corresponding moiré phonons. At $T \sim 4$ K, the thermal conductivity is reduced up to around 35% and 40% in the P and AP cases, respectively. In the limit of $T \to 0$, we find that the AP case exhibits greater enhancement of κ than in the P case. This is attributed to the smaller phonon velocity v in the lowest branch in the AP case [Fig. 4.6] and the fact that κ for the linear band regime is proportional to $1/v$ as argued in the previous section. Accordingly, we have the corresponding change of the power coefficient (α) in $\kappa(T) \propto T^{\alpha}$ in a similar manner to TBG and t-G/hBN.

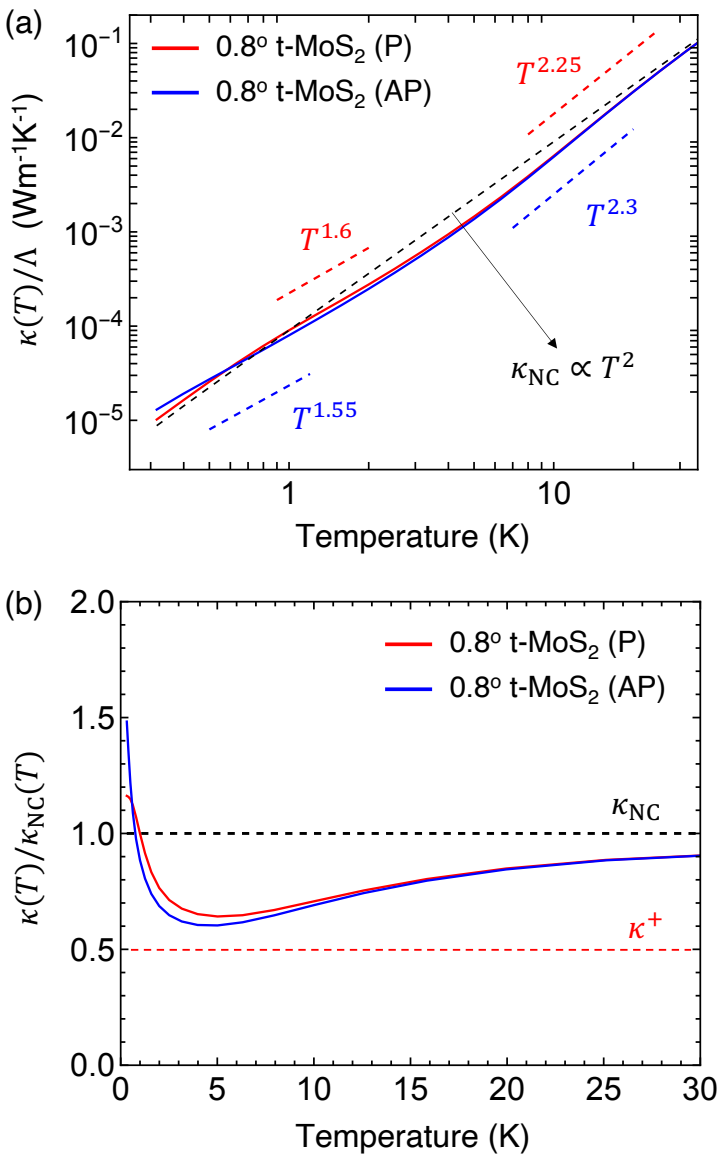

Figure 4.7: (a) Thermal conductivity of t-MoS_2 with $\theta = 0.8°$ for the parallel case (red line) and antiparallel case (blue line). (b) Relative thermal conductivity to the noncoupling case, $\kappa_{NC}(T)$.

Chapter 5

Conclusion

In this thesis, we have investigated the moiré effect on the low-frequency phonons and the low-temperature thermal conductivity of twisted bilayer systems.

In Chapter 2, we presented a continuum approach to investigate the effect of interlayer moiré potential on the in-plane acoustic phonons of twisted bilayer moiré superlattices. Specifically, we extend the existing model for TBG [45] , so that it also applicable for heterobilayer systems. We demonstrate this by considering various representative of twisted bilayer systems; TBG as a typical homobilayer case, twisted graphene/hBN as the common example of heterobilayers, and twisted bilayer MoS_2 to represent the transition metal dichalcogenides family. Using the static version of the model, we obtain the relaxed structure of each system. These relaxed states are characterized by the enlargement of regions with the most stable stacking configuration. The final structure can be viewed as an effective superlattice at the moiré scale which are further classified as either triangular or honeycomb.

In Chapter 3, we employ the continuum model to study the low-frequency phonons of each considered system. Here, we showed that the phonon band structure evolves in the same manner as the lattice relaxation. Their correspondence becomes clear at the low twist angle limit (or equivalently, the strong interlayer coupling regime), where universal features on the band structure are found across different systems. Specifically, these features are shown as an extreme flattening of some particular bands and a repeating unit consisting a specific order of dispersive bands and flat bands. We then develop an effective model consisting of a chain of mass and bonds that simulates the dynamics of the domain walls in the

relaxed domain structure of the actual systems. We showed that this model can qualitatively reproduces the original band structure, particularly the flat phonon bands where perfect correspondence can be observed. Then, using the effective model, we find that the flat phonon bands that are found across different systems are originated from the string-like oscillations of the domain walls. For the honeycomb-type effective lattice, the oscillation modes corresponding to the flat bands are analogous to the stationary wave on an isolated string with *open* boundary conditions. In contrast, for the triangular-type lattice, these modes correspond to a string with *closed* boundary conditions.

In the latter part of Chapter 3, we also investigate the chiral property of moiré phonons. We calculated the phonon angular momentum for twisted graphene/hBN and found a significant signal not only at the highly-symmetric Brillouin-zone corners, but also in the entire k-space regions for the lowest bands. We also reveal the twist-angle dependence of these chiral phonons. For the lowest two modes, the finite angular momentum only present near 0° twist angle where the corresponding bands are nearly degenerate. On the other hand, the chiral phonons at the BZ corners persists at large twist angle with a sign-inversion at around 0.3°.

In Chapter 4, we investigate how changes in the low-frequency phonons induced by the moiré effects are reflected in the thermal transport phenomena. We calculated the thermal conductivity for each system using the semiclassical approach. In general, we found a reduction of thermal conductivity due to an overall flattening of the phonon bands. The largest reduction is around 35-40% which occurs at around 20 K for 0.817° TBG and 0° t-G/hBN and around 4 K for 0.8° t-MoS_2/MoS_2. At higher temperature, the thermal conductivity returns towards the original intrinsic value, as the moiré superlattice effect for the acoustic phonons is significant only in the low energy region. These changes result in a characteristic deviation to the original quadratic temperature dependence of two-dimensional systems where linear acoustic phonons dominate the thermal transport properties.

Finally, we would like to make a final remark regarding the important achievement of this work and its future perspective. Here, we have established a clear correspondence between the relaxed structure of moiré superlattices and their phonon band structure. This provides an additional tuning mechanism where changes in lattice relaxation are reflected in the phonon band structure, and vice versa. For instance, in homobilayers with different atoms on the sublattices, such as MoS_2 and hBN, a transverse electric field induces a potential difference between AB/BA stacking configurations due to their opposite polarizations. As a result, adjusting the magnitude of the electric field would alter both the relaxed structure and the phonon properties [158, 159, 160]. The notable features, such as flat phonon bands and chiral moiré phonons with sub-meV gaps are expected to entail various physical consequences. For instance, bosonic condensation on flat bands through an external excitation was realized in an exciton-polariton system [161]. For moiré phonons, a possible excitation mechanism is through electromagnetic radiation, since in some cases such as graphene/hBN, the moiré superlattice has inversion-asymmetric charge densities [162], and the moiré phonon modes at the zone boundary would couple to an in-plane AC electric field. Meanwhile, band flatness is also generally associated with the existence of a spatially-localized eigenmode. In our moiré phonon system, this suggests that highly localized phonon excitation (vibration of a single domain wall sector) is possible, as was achieved in photonic lattice [163, 164]. Lastly, we expect that signature of moiré effect on the temperature dependence of thermal conductivity provide a promising way to observe the moiré effects on phonon properties of twisted bilayer moiré superlattices, which so far remains elusive. Furthermore, the tunability of thermal conductivity would also enable the engineering of thermal transport for the development of future thermal devices.

Bibliography

[1] J. M. B. Lopes dos Santos, N. M. R. Peres, and A. H. Castro Neto, "Graphene bilayer with a twist: Electronic structure," *Physical Review Letters*, vol. 99, no. 25, p. 256802, Dec. 2007.

[2] G. Li, A. Luican, J. M. B. L. d. Santos, A. H. C. Neto, A. Reina, J. Kong, and E. Y. Andrei, "Observation of van hove singularities in twisted graphene layers," *Nature Physics*, vol. 6, no. 2, pp. 109–113, 2009.

[3] E. J. Mele, "Commensuration and interlayer coherence in twisted bilayer graphene," *Physical Review B*, vol. 81, no. 16, p. 161405, 2010.

[4] G. Trambly de Laissardière, D. Mayou, and L. Magaud, "Localization of dirac electrons in rotated graphene bilayers," *Nano letters*, vol. 10, no. 3, pp. 804–808, 2010.

[5] S. Shallcross, S. Sharma, E. Kandelaki, and O. A. Pankratov, "Electronic structure of turbostratic graphene," *Physical Review B*, vol. 81, no. 16, p. 165105, 2010.

[6] E. Suárez Morell, J. D. Correa, P. Vargas, M. Pacheco, and Z. Barticevic, "Flat bands in slightly twisted bilayer graphene: Tight-binding calculations," *Physical Review B*, vol. 82, no. 12, p. 121407(R), Sep. 2010. [Online]. Available: https://ui.adsabs.harvard.edu/abs/2010PhRvB..82l1407S

[7] A. Luican, G. Li, A. Reina, J. Kong, R. Nair, K. S. Novoselov, A. K. Geim, and E. Andrei, "Single-layer behavior and its breakdown in twisted graphene layers," *Physical review letters*, vol. 106, no. 12, p. 126802, 2011.

[8] R. Bistritzer and A. H. MacDonald, "Moiré bands in twisted double-layer graphene," *Proceedings of the National Academy of Sciences*, vol. 108, no. 30, pp. 12 233–12 237, 2011.

[9] M. Kindermann and P. N. First, "Local sublattice-symmetry breaking in rotationally faulted multilayer graphene," *Physical Review B*, vol. 83, no. 4, p. 045425, 2011.

[10] J. M. B. Lopes dos Santos, N. M. R. Peres, and A. H. Castro Neto, "Continuum model of the twisted graphene bilayer," *Physical Review B*, vol. 86, no. 15, p. 155449, 2012.

[11] P. Moon and M. Koshino, "Energy spectrum and quantum hall effect in twisted bilayer graphene," *Physical Review B*, vol. 85, no. 19, p. 195458, 2012.

[12] G. Trambly de Laissardière, D. Mayou, and L. Magaud, "Numerical studies of confined states in rotated bilayers of graphene," *Physical Review B*, vol. 86, no. 12, p. 125413, 2012.

[13] P. Moon and M. Koshino, "Optical absorption in twisted bilayer graphene," *Physical Review B*, vol. 87, no. 20, p. 205404, 2013.

[14] Y. Cao, V. Fatemi, S. Fang, K. Watanabe, T. Taniguchi, E. Kaxiras, and P. Jarillo-Herrero, "Unconventional superconductivity in magic-angle graphene superlattices," *Nature*, vol. 556, no. 7699, pp. 43–50, 2018.

[15] Y. Cao, V. Fatemi, A. Demir, S. Fang, S. L. Tomarken, J. Y. Luo, J. D. Sanchez-Yamagishi, K. Watanabe, T. Taniguchi, E. Kaxiras *et al.*, "Correlated insulator behaviour at half-filling in magic-angle graphene superlattices," *Nature*, vol. 556, no. 7699, pp. 80–84, 2018.

[16] M. Yankowitz, J. Xue, D. Cormode, J. D. Sanchez-Yamagishi, K. Watanabe, T. Taniguchi, P. Jarillo-Herrero, P. Jacquod, and B. J. LeRoy, "Emergence of superlattice dirac points in graphene on hexagonal boron nitride," *Nature physics*, vol. 8, no. 5, pp. 382–386, 2012.

[17] L. A. Ponomarenko, R. V. Gorbachev, G. L. Yu, D. C. Elias, R. Jalil, A. A. Patel, A. Mishchenko, A. S. Mayorov, C. R. Woods, J. R. Wallbank, M. Mucha-Kruczynski, B. A. Piot, M. Potemski, I. V. Grigorieva, K. S. Novoselov, F. Guinea, V. I. Fal'ko, and A. K. Geim, "Cloning of dirac fermions in graphene superlattices," *Nature*, vol. 497, no. 7451, pp. 594–597, 2013.

[18] C. R. Dean, L. Wang, P. Maher, C. Forsythe, F. Ghahari, Y. Gao, J. Katoch, M. Ishigami, P. Moon, M. Koshino *et al.*, "Hofstadter's butterfly and the fractal quantum hall effect in moiré superlattices," *Nature*, vol. 497, no. 7451, pp. 598–602, 2013.

[19] B. Hunt, J. D. Sanchez-Yamagishi, A. F. Young, M. Yankowitz, B. J. LeRoy, K. Watanabe, T. Taniguchi, P. Moon, M. Koshino, P. Jarillo-Herrero *et al.*, "Massive dirac fermions and hofstadter butterfly in a van der waals heterostructure," *Science*, vol. 340, no. 6139, pp. 1427–1430, 2013.

[20] P. Moon and M. Koshino, "Electronic properties of graphene/hexagonal-boron-nitride moiré superlattice," *Physical Review B*, vol. 90, no. 15, p. 155406, Oct. 2014.

[21] L. Wang, Y. Gao, B. Wen, Z. Han, T. Taniguchi, K. Watanabe, M. Koshino, J. Hone, and C. R. Dean, "Evidence for a fractional fractal quantum hall effect in graphene superlattices," *Science*, vol. 350, no. 6265, pp. 1231–1234, Dec. 2015.

[22] R. Ribeiro-Palau, C. Zhang, K. Watanabe, T. Taniguchi, J. Hone, and C. R. Dean, "Twistable electronics with dynamically rotatable heterostructures," *Science*, vol. 361, no. 6403, pp. 690–693, Aug. 2018.

[23] G. Chen, L. Jiang, S. Wu, B. Lyu, H. Li, B. L. Chittari, K. Watanabe, T. Taniguchi, Z. Shi, J. Jung, Y. Zhang, and F. Wang, "Evidence of a gate-tunable mott insulator in a trilayer graphene moiré superlattice," *Nature Physics*, vol. 15, no. 3, pp. 237–241, Jan. 2019.

[24] H. Oka and M. Koshino, "Fractal energy gaps and topological invariants in hBN/graphene/hBN double moiré systems," *Physical Review B*, vol. 104, no. 3, p. 035306, Jul. 2021.

[25] V. W. Brar, M. S. Jang, M. Sherrott, S. Kim, J. J. Lopez, L. B. Kim, M. Choi, and H. Atwater, "Hybrid surface-phonon-plasmon polariton modes in graphene/monolayer h-BN heterostructures," *Nano Letters*, vol. 14, no. 7, pp. 3876–3880, Jun. 2014.

[26] G. X. Ni, H. Wang, J. S. Wu, Z. Fei, M. D. Goldflam, F. Keilmann, B. Özyilmaz, A. H. C. Neto, X. M. Xie, M. M. Fogler, and D. N. Basov, "Plasmons in graphene moiré superlattices," *Nature Materials*, vol. 14, no. 12, pp. 1217–1222, Sep. 2015.

[27] P. Huang, E. Riccardi, S. Messelot, H. Graef, F. Valmorra, J. Tignon, T. Taniguchi, K. Watanabe, S. Dhillon, B. Plaçais, R. Ferreira, and J. Mangeney, "Ultra-long carrier lifetime in neutral graphene-hBN van der waals heterostructures under mid-infrared illumination," *Nature Communications*, vol. 11, no. 1, p. 863, Feb. 2020.

[28] H. Zhang, S. Wang, E. Wang, X. Lu, Q. Li, C. Bao, K. Deng, H. Zhang, W. Yao, G. Chen, A. V. Fedorov, J. D. Denlinger, K. Watanabe, T. Taniguchi, G. Zhang, and S. Zhou, "Experimental evidence of plasmarons and effective fine structure constant in electron-doped graphene/h-BN heterostructure," *npj Quantum Materials*, vol. 6, no. 1, p. 83, Oct. 2021.

[29] P. Rivera, J. R. Schaibley, A. M. Jones, J. S. Ross, S. Wu, G. Aivazian, P. Klement, K. Seyler, G. Clark, N. J. Ghimire *et al.*, "Observation of long-lived interlayer excitons in monolayer mose2–wse2 heterostructures," *Nature communications*, vol. 6, no. 1, p. 6242, 2015.

[30] F. Wu, T. Lovorn, E. Tutuc, and A. H. MacDonald, "Hubbard model physics in transition metal dichalcogenide moiré bands," *Physical review letters*, vol. 121, no. 2, p. 026402, 2018.

[31] F. Wu, T. Lovorn, E. Tutuc, I. Martin, and A. MacDonald, "Topological insulators in twisted transition metal dichalcogenide homobilayers," *Physical review letters*, vol. 122, no. 8, p. 086402, 2019.

[32] K. L. Seyler, P. Rivera, H. Yu, N. P. Wilson, E. L. Ray, D. G. Mandrus, J. Yan, W. Yao, and X. Xu, "Signatures of moiré-trapped valley excitons in mose2/wse2 heterobilayers," *Nature*, vol. 567, no. 7746, pp. 66–70, 2019.

[33] K. Tran, G. Moody, F. Wu, X. Lu, J. Choi, K. Kim, A. Rai, D. A. Sanchez, J. Quan, A. Singh *et al.*, "Evidence for moiré excitons in van der waals heterostructures," *Nature*, vol. 567, no. 7746, pp. 71–75, 2019.

[34] L. Wang, E.-M. Shih, A. Ghiotto, L. Xian, D. A. Rhodes, C. Tan, M. Claassen, D. M. Kennes, Y. Bai, B. Kim *et al.*, "Correlated electronic phases in twisted bilayer transition metal dichalcogenides," *Nature materials*, vol. 19, no. 8, pp. 861–866, 2020.

[35] Y. Shimazaki, I. Schwartz, K. Watanabe, T. Taniguchi, M. Kroner, and A. Imamoğlu, "Strongly correlated electrons and hybrid excitons in a moiré heterostructure," *Nature*, vol. 580, no. 7804, pp. 472–477, 2020.

[36] A. Ghiotto, E.-M. Shih, G. S. Pereira, D. A. Rhodes, B. Kim, J. Zang, A. J. Millis, K. Watanabe, T. Taniguchi, J. C. Hone *et al.*, "Quantum criticality in twisted transition metal dichalcogenides," *Nature*, vol. 597, no. 7876, pp. 345–349, 2021.

[37] S. Miao, T. Wang, X. Huang, D. Chen, Z. Lian, C. Wang, M. Blei, T. Taniguchi, K. Watanabe, S. Tongay *et al.*, "Strong interaction between interlayer excitons and correlated electrons in wse2/ws2 moiré superlattice," *Nature communications*, vol. 12, no. 1, p. 3608, 2021.

[38] J.-W. Jiang, B.-S. Wang, and T. Rabczuk, "Acoustic and breathing phonon modes in bilayer graphene with moiré patterns," *Applied Physics Letters*, vol. 101, no. 2, p. 023113, 2012.

[39] J. Campos-Delgado, L. G. Cançado, C. A. Achete, A. Jorio, and J.-P. Raskin, "Raman scattering study of the phonon dispersion in twisted bilayer graphene," *Nano Research*, vol. 6, pp. 269–274, 2013.

[40] A. I. Cocemasov, D. L. Nika, and A. A. Balandin, "Phonons in twisted bilayer graphene," *Physical Review B*, vol. 88, no. 3, p. 035428, 2013.

[41] Y. W. Choi and H. J. Choi, "Strong electron-phonon coupling, electron-hole asymmetry, and nonadiabaticity in magic-angle twisted bilayer graphene," *Physical Review B*, vol. 98, no. 24, p. 241412, 2018.

[42] M.-L. Lin, Q.-H. Tan, J.-B. Wu, X.-S. Chen, J.-H. Wang, Y.-H. Pan, X. Zhang, X. Cong, J. Zhang, W. Ji, P.-A. Hu, K.-H. Liu, and P.-H. Tan, "Moiré phonons in twisted bilayer mos2," *ACS Nano*, vol. 12, no. 8, pp. 8770–8780, aug 2018.

[43] P. Parzefall, J. Holler, M. Scheuck, A. Beer, K.-Q. Lin, B. Peng, B. Monserrat, P. Nagler, M. Kempf, T. Korn *et al.*, "Moiré phonons in twisted mose2–wse2 heterobilayers and their correlation with interlayer excitons," *2D Materials*, vol. 8, no. 3, p. 035030, 2021.

[44] M. Angeli, E. Tosatti, and M. Fabrizio, "Valley jahn-teller effect in twisted bilayer graphene," *Physical Review X*, vol. 9, no. 4, p. 041010, 2019.

[45] M. Koshino and Y.-W. Son, "Moiré phonons in twisted bilayer graphene," *Physical Review B*, vol. 100, no. 7, p. 075416, 2019.

[46] H. Ochoa, "Moiré-pattern fluctuations and electron-phason coupling in twisted bilayer graphene," *Physical Review B*, vol. 100, no. 15, p. 155426, oct 2019.

[47] M. Lamparski, B. V. Troeye, and V. Meunier, "Soliton signature in the phonon spectrum of twisted bilayer graphene," *2D Materials*, vol. 7, no. 2, p. 025050, mar 2020.

[48] I. Maity, M. H. Naik, P. K. Maiti, H. R. Krishnamurthy, and M. Jain, "Phonons in twisted transition-metal dichalcogenide bilayers: Ultrasoft phasons and a transition from a superlubric to a pinned phase," *Physical Review Research*, vol. 2, no. 1, p. 013335, mar 2020.

[49] A. C. Gadelha, D. A. A. Ohlberg, C. Rabelo, E. G. S. Neto, T. L. Vasconcelos, J. L. Campos, J. S. Lemos, V. Ornelas, D. Miranda, R. Nadas, F. C. Santana, K. Watanabe, T. Taniguchi, B. van Troeye, M. Lamparski, V. Meunier, V.-H. Nguyen, D. Paszko, J.-C. Charlier, L. C. Campos, L. G. Cançado, G. Medeiros-Ribeiro, and A. Jorio, "Localization of lattice dynamics in low-angle twisted bilayer graphene," *Nature*, vol. 590, no. 7846, pp. 405–409, feb 2021.

[50] J. Quan, L. Linhart, M.-L. Lin, D. Lee, J. Zhu, C.-Y. Wang, W.-T. Hsu, J. Choi, J. Embley, C. Young, T. Taniguchi, K. Watanabe, C.-K. Shih, K. Lai, A. H. MacDonald, P.-H. Tan, F. Libisch, and X. Li, "Phonon renormalization in reconstructed MoS2 moiré superlattices," *Nature Materials*, vol. 20, no. 8, pp. 1100–1105, mar 2021.

[51] I. Maity, A. A. Mostofi, and J. Lischner, "Chiral valley phonons and flat phonon bands in moiré materials," *Physical Review B*, vol. 105, no. 4, p. l041408, jan 2022.

[52] J. Z. Lu, Z. Zhu, M. Angeli, D. T. Larson, and E. Kaxiras, "Low-energy moiré phonons in twisted bilayer van der waals heterostructures," *Physical Review B*, vol. 106, no. 14, p. 144305, oct 2022.

[53] B. Xie and J. Liu, "Lattice distortions, moiré phonons, and relaxed electronic band structures in magic-angle twisted bilayer graphene," *Physical Review B*, vol. 108, no. 9, p. 094115, 2023.

[54] N. Girotto, L. Linhart, and F. Libisch, "Coupled phonons in twisted bilayer graphene," *Physical Review B*, vol. 108, no. 15, p. 155415, 2023.

[55] N. Suri, C. Wang, Y. Zhang, and D. Xiao, "Chiral phonons in moiré superlattices," *Nano Letters*, vol. 21, no. 23, pp. 10 026–10 031, nov 2021.

[56] L. P. Krisna and M. Koshino, "Moiré phonons in graphene/hexagonal boron nitride moiré superlattice," *Physical Review B*, vol. 107, no. 11, p. 115301, 2023.

[57] K. S. Novoselov, A. K. Geim, S. V. Morozov, D. Jiang, Y. Zhang, S. V. Dubonos, I. V. Grigorieva, and A. A. Firsov, "Electric field effect in atomically thin carbon films," *Science*, vol. 306, no. 5696, pp. 666–669, Oct. 2004.

[58] K. S. Novoselov, A. K. Geim, S. V. Morozov, D. Jiang, M. I. Katsnelson, I. V. Grigorieva, S. Dubonos, and A. Firsov, "Two-dimensional gas of massless dirac fermions in graphene," *nature*, vol. 438, no. 7065, pp. 197–200, 2005.

[59] S. Morozov, K. Novoselov, M. Katsnelson, F. Schedin, D. C. Elias, J. A. Jaszczak, and A. Geim, "Giant intrinsic carrier mobilities in graphene and its bilayer," *Physical review letters*, vol. 100, no. 1, p. 016602, 2008.

[60] K. S. Novoselov, Z.-f. Jiang, Y.-s. Zhang, S. Morozov, H. L. Stormer, U. Zeitler, J. Maan, G. Boebinger, P. Kim, and A. K. Geim, "Room-temperature quantum hall effect in graphene," *science*, vol. 315, no. 5817, pp. 1379–1379, 2007.

[61] C. Beenakker, "Colloquium: Andreev reflection and klein tunneling in graphene," *Reviews of Modern Physics*, vol. 80, no. 4, p. 1337, 2008.

[62] A. K. Geim and I. V. Grigorieva, "Van der waals heterostructures," *Nature*, vol. 499, no. 7459, pp. 419–425, 2013.

[63] A. Avsar, J. Y. Tan, T. Taychatanapat, J. Balakrishnan, G. Koon, Y. Yeo, J. Lahiri, A. Carvalho, A. Rodin, E. O'farrell *et al.*, "Spin–orbit proximity effect in graphene," *Nature communications*, vol. 5, no. 1, p. 4875, 2014.

[64] M. Gmitra and J. Fabian, "Graphene on transition-metal dichalcogenides: A platform for proximity spin-orbit physics and optospintronics," *Physical Review B*, vol. 92, no. 15, p. 155403, 2015.

[65] Y. Li and M. Koshino, "Twist-angle dependence of the proximity spin-orbit coupling in graphene on transition-metal dichalcogenides," *Physical Review B*, vol. 99, no. 7, p. 075438, 2019.

[66] E. Y. Andrei, D. K. Efetov, P. Jarillo-Herrero, A. H. MacDonald, K. F. Mak, T. Senthil, E. Tutuc, A. Yazdani, and A. F. Young, "The marvels of moiré materials," *Nature Reviews Materials*, vol. 6, no. 3, pp. 201–206, Mar. 2021.

[67] K. Uchida, S. Furuya, J.-I. Iwata, and A. Oshiyama, "Atomic corrugation and electron localization due to moiré patterns in twisted bilayer graphenes," *Physical Review B*, vol. 90, no. 15, p. 155451, oct 2014.

[68] X. Lu, P. Stepanov, W. Yang, M. Xie, M. A. Aamir, I. Das, C. Urgell, K. Watanabe, T. Taniguchi, G. Zhang *et al.*, "Superconductors, orbital magnets and correlated states in magic-angle bilayer graphene," *Nature*, vol. 574, no. 7780, pp. 653–657, 2019.

[69] Y. Saito, J. Ge, K. Watanabe, T. Taniguchi, and A. F. Young, "Independent superconductors and correlated insulators in twisted bilayer graphene," *Nature Physics*, vol. 16, no. 9, pp. 926–930, 2020.

[70] P. Stepanov, I. Das, X. Lu, A. Fahimniya, K. Watanabe, T. Taniguchi, F. H. Koppens, J. Lischner, L. Levitov, and D. K. Efetov, "Untying the insulating and superconducting orders in magic-angle graphene," *Nature*, vol. 583, no. 7816, pp. 375–378, 2020.

[71] H. Polshyn, M. Yankowitz, S. Chen, Y. Zhang, K. Watanabe, T. Taniguchi, C. R. Dean, and A. F. Young, "Large linear-in-temperature resistivity in

twisted bilayer graphene," *Nature Physics*, vol. 15, no. 10, pp. 1011–1016, 2019.

[72] Y. Cao, D. Chowdhury, D. Rodan-Legrain, O. Rubies-Bigorda, K. Watanabe, T. Taniguchi, T. Senthil, and P. Jarillo-Herrero, "Strange metal in magic-angle graphene with near planckian dissipation," *Physical review letters*, vol. 124, no. 7, p. 076801, 2020.

[73] A. Jaoui, I. Das, G. D. Battista, J. Díez-Mérida, X. Lu, K. Watanabe, T. Taniguchi, H. Ishizuka, L. Levitov, and D. K. Efetov, "Quantum critical behaviour in magic-angle twisted bilayer graphene," *Nature Physics*, vol. 18, no. 6, pp. 633–638, Apr. 2022.

[74] A. L. Sharpe, E. J. Fox, A. W. Barnard, J. Finney, K. Watanabe, T. Taniguchi, M. Kastner, and D. Goldhaber-Gordon, "Emergent ferromagnetism near three-quarters filling in twisted bilayer graphene," *Science*, vol. 365, no. 6453, pp. 605–608, 2019.

[75] M. Serlin, C. L. Tschirhart, H. Polshyn, Y. Zhang, J. Zhu, K. Watanabe, T. Taniguchi, L. Balents, and A. F. Young, "Intrinsic quantized anomalous hall effect in a moiré heterostructure," *Science*, vol. 367, no. 6480, pp. 900–903, 2020.

[76] G. Chen, A. L. Sharpe, E. J. Fox, Y.-H. Zhang, S. Wang, L. Jiang, B. Lyu, H. Li, K. Watanabe, T. Taniguchi, Z. Shi, T. Senthil, D. Goldhaber-Gordon, Y. Zhang, and F. Wang, "Tunable correlated chern insulator and ferromagnetism in a moiré superlattice," *Nature*, vol. 579, no. 7797, pp. 56–61, Mar. 2020.

[77] C. Lee, X. Wei, J. W. Kysar, and J. Hone, "Measurement of the elastic properties and intrinsic strength of monolayer graphene," *science*, vol. 321, no. 5887, pp. 385–388, 2008.

[78] C. R. Dean, A. F. Young, I. Meric, C. Lee, L. Wang, S. Sorgenfrei, K. Watanabe, T. Taniguchi, P. Kim, K. L. Shepard, and J. Hone, "Boron nitride substrates for high-quality graphene electronics," *Nature Nanotechnology*, vol. 5, no. 10, pp. 722–726, 2010.

[79] A. M. Popov, I. V. Lebedeva, A. A. Knizhnik, Y. E. Lozovik, and B. V. Potapkin, "Commensurate-incommensurate phase transition in bilayer graphene," *Physical Review B*, vol. 84, no. 4, p. 045404, 2011.

[80] I. V. Lebedeva, A. A. Knizhnik, A. M. Popov, Y. E. Lozovik, and B. V. Potapkin, "Interlayer interaction and relative vibrations of bilayer graphene," *Physical Chemistry Chemical Physics*, vol. 13, no. 13, pp. 5687–5695, 2011.

[81] T. Gould, S. Lebègue, and J. F. Dobson, "Dispersion corrections in graphenic systems: a simple and effective model of binding," *Journal of Physics: Condensed Matter*, vol. 25, no. 44, p. 445010, 2013.

[82] S. Zhou, J. Han, S. Dai, J. Sun, and D. J. Srolovitz, "van der waals bilayer energetics: Generalized stacking-fault energy of graphene, boron nitride, and graphene/boron nitride bilayers," *Physical Review B*, vol. 92, no. 15, p. 155438, 2015.

[83] M. M. van Wijk, A. Schuring, M. I. Katsnelson, and A. Fasolino, "Relaxation of moiré patterns for slightly misaligned identical lattices: graphene on graphite," *2D Materials*, vol. 2, no. 3, p. 034010, jul 2015.

[84] S. K. Jain, V. Juričić, and G. T. Barkema, "Structure of twisted and buckled bilayer graphene," *2D Materials*, vol. 4, no. 1, p. 015018, 2016.

[85] N. N. Nam and M. Koshino, "Lattice relaxation and energy band modulation in twisted bilayer graphene," *Physical Review B*, vol. 96, no. 7, p. 075311, 2017.

[86] S. Carr, D. Massatt, S. B. Torrisi, P. Cazeaux, M. Luskin, and E. Kaxiras, "Relaxation and domain formation in incommensurate two-dimensional heterostructures," *Physical Review B*, vol. 98, no. 22, p. 224102, 2018.

[87] J. Lin, W. Fang, W. Zhou, A. R. Lupini, J. C. Idrobo, J. Kong, S. J. Pennycook, and S. T. Pantelides, "Ac/ab stacking boundaries in bilayer graphene," *Nano letters*, vol. 13, no. 7, pp. 3262–3268, 2013.

[88] L. Brown, R. Hovden, P. Huang, M. Wojcik, D. A. Muller, and J. Park, "Twinning and twisting of tri-and bilayer graphene," *Nano letters*, vol. 12, no. 3, pp. 1609–1615, 2012.

[89] J. S. Alden, A. W. Tsen, P. Y. Huang, R. Hovden, L. Brown, J. Park, D. A. Muller, and P. L. McEuen, "Strain solitons and topological defects in bilayer graphene," *Proceedings of the National Academy of Sciences*, vol. 110, no. 28, pp. 11 256–11 260, 2013.

[90] H. Yoo, R. Engelke, S. Carr, S. Fang, K. Zhang, P. Cazeaux, S. H. Sung, R. Hovden, A. W. Tsen, T. Taniguchi *et al.*, "Atomic and electronic reconstruction at the van der waals interface in twisted bilayer graphene," *Nature materials*, vol. 18, no. 5, pp. 448–453, 2019.

[91] S. Dai, Y. Xiang, and D. J. Srolovitz, "Twisted bilayer graphene: Moiré with a twist," *Nano letters*, vol. 16, no. 9, pp. 5923–5927, 2016.

[92] X. Lin, D. Liu, and D. Tománek, "Shear instability in twisted bilayer graphene," *Physical Review B*, vol. 98, no. 19, p. 195432, nov 2018.

[93] M. Koshino, N. F. Yuan, T. Koretsune, M. Ochi, K. Kuroki, and L. Fu, "Maximally localized wannier orbitals and the extended hubbard model for twisted bilayer graphene," *Physical Review X*, vol. 8, no. 3, p. 031087, 2018.

[94] F. Guinea and N. R. Walet, "Continuum models for twisted bilayer graphene: Effect of lattice deformation and hopping parameters," *Physical Review B*, vol. 99, no. 20, p. 205134, 2019.

[95] Y. Jiang, X. Lai, K. Watanabe, T. Taniguchi, K. Haule, J. Mao, and E. Y. Andrei, "Charge order and broken rotational symmetry in magic-angle twisted bilayer graphene," *Nature*, vol. 573, no. 7772, pp. 91–95, 2019.

[96] S. Carr, S. Fang, H. C. Po, A. Vishwanath, and E. Kaxiras, "Derivation of wannier orbitals and minimal-basis tight-binding hamiltonians for twisted bilayer graphene: First-principles approach," *Physical Review Research*, vol. 1, no. 3, p. 033072, 2019.

[97] J. Kang and O. Vafek, "Symmetry, maximally localized wannier states, and a low-energy model for twisted bilayer graphene narrow bands," *Physical Review X*, vol. 8, no. 3, p. 031088, 2018.

[98] X. Y. Xu, K. T. Law, and P. A. Lee, "Kekulé valence bond order in an extended hubbard model on the honeycomb lattice with possible applications to twisted bilayer graphene," *Physical Review B*, vol. 98, no. 12, p. 121406, 2018.

[99] Z.-D. Song and B. A. Bernevig, "Magic-angle twisted bilayer graphene as a topological heavy fermion problem," *Physical review letters*, vol. 129, no. 4, p. 047601, 2022.

[100] B. Tsim, N. N. Nam, and M. Koshino, "Perfect one-dimensional chiral states in biased twisted bilayer graphene," *Physical Review B*, vol. 101, no. 12, p. 125409, 2020.

[101] B. Amorim, A. Cortijo, F. de Juan, A. Grushin, F. Guinea, A. Gutiérrez-Rubio, H. Ochoa, V. Parente, R. Roldán, P. San-Jose, J. Schiefele, M. Sturla, and M. Vozmediano, "Novel effects of strains in graphene and other two dimensional materials," *Physics Reports*, vol. 617, pp. 1–54, mar 2016.

[102] J.-A. Yan, W. Ruan, and M. Chou, "Phonon dispersions and vibrational properties of monolayer, bilayer, and trilayer graphene: Density-functional perturbation theory," *Physical Review B—Condensed Matter and Materials Physics*, vol. 77, no. 12, p. 125401, 2008.

[103] P. Tan, W. Han, W. Zhao, Z. Wu, K. Chang, H. Wang, Y. Wang, N. Bonini, N. Marzari, N. Pugno *et al.*, "The shear mode of multilayer graphene," *Nature materials*, vol. 11, no. 4, pp. 294–300, 2012.

[104] D. Boschetto, L. Malard, C. H. Lui, K. F. Mak, Z. Li, H. Yan, and T. F. Heinz, "Real-time observation of interlayer vibrations in bilayer and few-layer graphene," *Nano letters*, vol. 13, no. 10, pp. 4620–4623, 2013.

[105] G. Pizzi, S. Milana, A. C. Ferrari, N. Marzari, and M. Gibertini, "Shear and breathing modes of layered materials," *ACS nano*, vol. 15, no. 8, pp. 12 509–12 534, 2021.

[106] H.-Q. Song, Z. Liu, and D.-B. Zhang, "Interlayer vibration of twisted bilayer graphene: A first-principles study," *Physics Letters A*, vol. 383, no. 22, pp. 2628–2632, 2019.

[107] P. M. Chaikin, T. C. Lubensky, and T. A. Witten, *Principles of condensed matter physics*. Cambridge university press Cambridge, 1995, vol. 10.

[108] Q. Gao and E. Khalaf, "Symmetry origin of lattice vibration modes in twisted multilayer graphene: Phasons versus moiré phonons," *Physical Review B*, vol. 106, no. 7, p. 075420, 2022.

[109] X. Liu, R. Peng, Z. Sun, and J. Liu, "Moiré phonons in magic-angle twisted bilayer graphene," *Nano letters*, vol. 22, no. 19, pp. 7791–7797, 2022.

[110] R. Samajdar, Y. Teng, and M. S. Scheurer, "Moiré phonons and impact of electronic symmetry breaking in twisted trilayer graphene," *Physical Review B*, vol. 106, no. 20, p. L201403, 2022.

[111] M. Koshino and N. N. T. Nam, "Effective continuum model for relaxed twisted bilayer graphene and moiré electron-phonon interaction," *Physical Review B*, vol. 101, no. 19, p. 195425, May 2020.

[112] H. Ochoa and R. M. Fernandes, "Extended linear-in-t resistivity due to electron-phason scattering in moiré superlattices," *Physical Review B*, vol. 108, no. 7, p. 075168, 2023.

[113] E. C. Regan, D. Wang, C. Jin, M. I. Bakti Utama, B. Gao, X. Wei, S. Zhao, W. Zhao, Z. Zhang, K. Yumigeta *et al.*, "Mott and generalized wigner crystal states in wse2/ws2 moiré superlattices," *Nature*, vol. 579, no. 7799, pp. 359–363, 2020.

[114] Y. Xu, S. Liu, D. A. Rhodes, K. Watanabe, T. Taniguchi, J. Hone, V. Elser, K. F. Mak, and J. Shan, "Correlated insulating states at fractional fillings of moiré superlattices," *Nature*, vol. 587, no. 7833, pp. 214–218, 2020.

[115] T. Li, S. Jiang, B. Shen, Y. Zhang, L. Li, Z. Tao, T. Devakul, K. Watanabe, T. Taniguchi, L. Fu *et al.*, "Quantum anomalous hall effect from intertwined moiré bands," *Nature*, vol. 600, no. 7890, pp. 641–646, 2021.

[116] T. Li, S. Jiang, L. Li, Y. Zhang, K. Kang, J. Zhu, K. Watanabe, T. Taniguchi, D. Chowdhury, L. Fu *et al.*, "Continuous mott transition in semiconductor moiré superlattices," *Nature*, vol. 597, no. 7876, pp. 350–354, 2021.

[117] Y.-M. Xie, C.-P. Zhang, J.-X. Hu, K. F. Mak, and K. T. Law, "Valley-polarized quantum anomalous hall state in moiré mote 2/wse 2 heterobilayers," *Physical Review Letters*, vol. 128, no. 2, p. 026402, 2022.

[118] P. San-Jose, A. Gutiérrez-Rubio, M. Sturla, and F. Guinea, "Spontaneous strains and gap in graphene on boron nitride," *Physical Review B*, vol. 90, no. 7, p. 075428, 2014.

[119] L. J. McGilly, A. Kerelsky, N. R. Finney, K. Shapovalov, E.-M. Shih, A. Ghiotto, Y. Zeng, S. L. Moore, W. Wu, Y. Bai, K. Watanabe, T. Taniguchi, M. Stengel, L. Zhou, J. Hone, X. Zhu, D. N. Basov, C. Dean, C. E. Dreyer, and A. N. Pasupathy, "Visualization of moiré superlattices," *Nature Nanotechnology*, vol. 15, no. 7, pp. 580–584, Jun. 2020.

[120] M. R. Rosenberger, H.-J. Chuang, M. Phillips, V. P. Oleshko, K. M. McCreary, S. V. Sivaram, C. S. Hellberg, and B. T. Jonker, "Twist angle-dependent atomic reconstruction and moiré patterns in transition metal dichalcogenide heterostructures," *ACS nano*, vol. 14, no. 4, pp. 4550–4558, 2020.

[121] V. Enaldiev, V. Zolyomi, C. Yelgel, S. Magorrian, and V. Fal'Ko, "Stacking domains and dislocation networks in marginally twisted bilayers of transition metal dichalcogenides," *Physical review letters*, vol. 124, no. 20, p. 206101, 2020.

[122] I. Maity, P. K. Maiti, H. Krishnamurthy, and M. Jain, "Reconstruction of moiré lattices in twisted transition metal dichalcogenide bilayers," *Physical Review B*, vol. 103, no. 12, p. L121102, 2021.

[123] S. L. Moore, C. J. Ciccarino, D. Halbertal, L. J. McGilly, N. R. Finney, K. Yao, Y. Shao, G. Ni, A. Sternbach, E. J. Telford, B. S. Kim, S. E. Rossi, K. Watanabe, T. Taniguchi, A. N. Pasupathy, C. R. Dean, J. Hone, P. J. Schuck, P. Narang, and D. N. Basov, "Nanoscale lattice dynamics in hexagonal boron nitride moiré superlattices," *Nature Communications*, vol. 12, no. 1, p. 5741, Sep. 2021.

[124] A. A. Balandin, S. Ghosh, W. Bao, I. Calizo, D. Teweldebrhan, F. Miao, and C. N. Lau, "Superior thermal conductivity of single-layer graphene," *Nano letters*, vol. 8, no. 3, pp. 902–907, 2008.

[125] D. Ghosh, I. Calizo, D. Teweldebrhan, E. P. Pokatilov, D. L. Nika, A. A. Balandin, W. Bao, F. Miao, and C. N. Lau, "Extremely high thermal conductivity of graphene: Prospects for thermal management applications in nanoelectronic circuits," *Applied Physics Letters*, vol. 92, no. 15, p. 151911, 2008.

[126] W. Cai, A. L. Moore, Y. Zhu, X. Li, S. Chen, L. Shi, and R. S. Ruoff, "Thermal transport in suspended and supported monolayer graphene grown by chemical vapor deposition," *Nano letters*, vol. 10, no. 5, pp. 1645–1651, 2010.

[127] S. Chen, Q. Wu, C. Mishra, J. Kang, H. Zhang, K. Cho, W. Cai, A. A. Balandin, and R. S. Ruoff, "Thermal conductivity of isotopically modified graphene," *Nature materials*, vol. 11, no. 3, pp. 203–207, 2012.

[128] J. H. Seol, I. Jo, A. L. Moore, L. Lindsay, Z. H. Aitken, M. T. Pettes, X. Li, Z. Yao, R. Huang, D. Broido *et al.*, "Two-dimensional phonon transport in supported graphene," *Science*, vol. 328, no. 5975, pp. 213–216, apr 2010.

[129] S. Ghosh, W. Bao, D. L. Nika, S. Subrina, E. P. Pokatilov, C. N. Lau, and A. A. Balandin, "Dimensional crossover of thermal transport in few-layer graphene," *Nature Materials*, vol. 9, no. 7, pp. 555–558, may 2010.

[130] Z.-X. Guo, D. Zhang, and X.-G. Gong, "Manipulating thermal conductivity through substrate coupling," *Physical Review B*, vol. 84, no. 7, p. 075470, 2011.

[131] L. Lindsay, D. A. Broido, and N. Mingo, "Flexural phonons and thermal transport in multilayer graphene and graphite," *Physical Review B*, vol. 83, no. 23, p. 235428, jun 2011.

[132] A. J. Pak and G. S. Hwang, "Theoretical analysis of thermal transport in graphene supported on hexagonal boron nitride: the importance of strong adhesion due to π-bond polarization," *Physical Review Applied*, vol. 6, no. 3, p. 034015, 2016.

[133] J.-H. Zou and B.-Y. Cao, "Phonon thermal properties of graphene on h-bn from molecular dynamics simulations," *Applied Physics Letters*, vol. 110, no. 10, p. 103106, 2017.

[134] J.-H. Zou, X.-T. Xu, and B.-Y. Cao, "Size-dependent mode contributions to the thermal transport of suspended and supported graphene," *Applied Physics Letters*, vol. 115, no. 12, p. 123105, 2019.

[135] H. Li, H. Ying, X. Chen, D. L. Nika, A. I. Cocemasov, W. Cai, A. A. Balandin, and S. Chen, "Thermal conductivity of twisted bilayer graphene," *Nanoscale*, vol. 6, no. 22, pp. 13 402–13 408, 2014.

[136] S. Han, X. Nie, S. Gu, W. Liu, L. Chen, H. Ying, L. Wang, Z. Cheng, L. Zhao, and S. Chen, "Twist-angle-dependent thermal conduction in single-crystalline bilayer graphene," *Applied Physics Letters*, vol. 118, no. 19, p. 193104, 2021.

[137] C. Li, B. Debnath, X. Tan, S. Su, K. Xu, S. Ge, M. R. Neupane, and R. K. Lake, "Commensurate lattice constant dependent thermal conductivity of misoriented bilayer graphene," *Carbon*, vol. 138, pp. 451–457, 2018.

[138] X. Nie, L. Zhao, S. Deng, Y. Zhang, and Z. Du, "How interlayer twist angles affect in-plane and cross-plane thermal conduction of multilayer graphene: A non-equilibrium molecular dynamics study," *International Journal of Heat and Mass Transfer*, vol. 137, pp. 161–173, 2019.

[139] S. Mandal, I. Maity, A. Das, M. Jain, and P. K. Maiti, "Tunable lattice thermal conductivity of twisted bilayer mos 2," *Physical Chemistry Chemical Physics*, vol. 24, no. 22, pp. 13 860–13 868, 2022.

[140] Y. Cheng, Z. Fan, T. Zhang, M. Nomura, S. Volz, G. Zhu, B. Li, and S. Xiong, "Magic angle in thermal conductivity of twisted bilayer graphene," *Materials Today Physics*, p. 101093, apr 2023.

[141] S. Ahmed, S. Alam, and A. Jain, "Understanding phonon thermal transport in twisted bilayer graphene," *Physical Review B*, vol. 108, no. 23, p. 235202, 2023.

[142] A. Weston, Y. Zou, V. Enaldiev, A. Summerfield, N. Clark, V. Zólyomi, A. Graham, C. Yelgel, S. Magorrian, M. Zhou *et al.*, "Atomic reconstruction in twisted bilayers of transition metal dichalcogenides," *Nature Nanotechnology*, vol. 15, no. 7, pp. 592–597, 2020.

[143] H. Suzuura and T. Ando, "Phonons and electron-phonon scattering in carbon nanotubes," *Physical review B*, vol. 65, no. 23, p. 235412, 2002.

[144] K. Zakharchenko, M. Katsnelson, and A. Fasolino, "Finite temperature lattice properties of graphene beyond the quasiharmonic approximation," *Physical review letters*, vol. 102, no. 4, p. 046808, 2009.

[145] J. Jung, A. M. DaSilva, A. H. MacDonald, and S. Adam, "Origin of band gaps in graphene on hexagonal boron nitride," *Nature communications*, vol. 6, no. 1, p. 6308, 2015.

[146] B. Sachs, T. Wehling, M. Katsnelson, and A. Lichtenstein, "Adhesion and electronic structure of graphene on hexagonal boron nitride substrates," *Physical Review B*, vol. 84, no. 19, p. 195414, 2011.

[147] C. Woods, L. Britnell, A. Eckmann, R. Ma, J. Lu, H. Guo, X. Lin, G. Yu, Y. Cao, R. V. Gorbachev *et al.*, "Commensurate–incommensurate transition in graphene on hexagonal boron nitride," *Nature physics*, vol. 10, no. 6, pp. 451–456, 2014.

[148] H. Ochoa and R. M. Fernandes, "Degradation of phonons in disordered moiré superlattices," *Physical review letters*, vol. 128, no. 6, p. 065901, 2022.

[149] J. Villain, "Commensurate-incommensurate transition of krypton monolayers on graphite: a low temperature theory," *Surface Science*, vol. 97, no. 1, pp. 219–242, 1980.

[150] L. Zhang and Q. Niu, "Chiral phonons at high-symmetry points in monolayer hexagonal lattices," *Physical Review Letters*, vol. 115, no. 11, p. 115502, Sep. 2015.

[151] ——, "Angular momentum of phonons and the einstein–de haas effect," *Physical Review Letters*, vol. 112, no. 8, p. 085503, Feb. 2014.

[152] J. Ziman, *Electrons and Phonons*. Oxford University Press, feb 2001.

[153] R. Prasher, "Thermal boundary resistance and thermal conductivity of multiwalled carbon nanotubes," *Physical Review B*, vol. 77, no. 7, p. 075424, 2008.

[154] J. Heremans and C. Beetz Jr, "Thermal conductivity and thermopower of vapor-grown graphite fibers," *Physical Review B*, vol. 32, no. 4, p. 1981, 1985.

[155] P. Klemens and D. Pedraza, "Thermal conductivity of graphite in the basal plane," *Carbon*, vol. 32, no. 4, pp. 735–741, 1994.

[156] A. Uri, S. Grover, Y. Cao, J. A. Crosse, K. Bagani, D. Rodan-Legrain, Y. Myasoedov, K. Watanabe, T. Taniguchi, P. Moon *et al.*, "Mapping the twist-angle disorder and landau levels in magic-angle graphene," *Nature*, vol. 581, no. 7806, pp. 47–52, 2020.

[157] T. Benschop, T. A. de Jong, P. Stepanov, X. Lu, V. Stalman, S. J. van der Molen, D. K. Efetov, and M. P. Allan, "Measuring local moiré lattice heterogeneity of twisted bilayer graphene," *Physical Review Research*, vol. 3, no. 1, p. 013153, 2021.

[158] K. Yasuda, X. Wang, K. Watanabe, T. Taniguchi, and P. Jarillo-Herrero, "Stacking-engineered ferroelectricity in bilayer boron nitride," *Science*, vol. 372, no. 6549, pp. 1458–1462, 2021.

[159] D. Bennett and B. Remez, "On electrically tunable stacking domains and ferroelectricity in moiré superlattices," *npj 2D Materials and Applications*, vol. 6, no. 1, p. 7, 2022.

[160] A. Ramos-Alonso, B. Remez, D. Bennett, R. M. Fernandes, and H. Ochoa, "Flat and tunable moire phonons in twisted transition-metal dichalcogenides," *arXiv preprint arXiv:2406.18779*, 2024.

[161] F. Baboux, L. Ge, T. Jacqmin, M. Biondi, E. Galopin, A. Lemaître, L. Le Gratiet, I. Sagnes, S. Schmidt, H. E. Türeci, A. Amo, and J. Bloch, "Bosonic condensation and disorder-induced localization in a flat band," *Physical Review Letters*, vol. 116, no. 6, p. 066402, feb 2016.

[162] J. Correa and E. Cisternas, "Ab initio calculations on twisted graphene/hBN: Electronic structure and STM image simulation," *Solid State Communications*, vol. 241, pp. 1–6, Sep. 2016.

[163] S. Mukherjee, A. Spracklen, D. Choudhury, N. Goldman, P. Öhberg, E. Andersson, and R. R. Thomson, "Observation of a localized flat-band state in a photonic lieb lattice," *Physical Review Letters*, vol. 114, no. 24, p. 245504, jun 2015. [Online]. Available: https://ui.adsabs.harvard.edu/abs/2015PhRvL.114x5504M

[164] R. A. Vicencio, C. Cantillano, L. Morales-Inostroza, B. Real, C. Mejía-Cortés, S. Weimann, A. Szameit, and M. I. Molina, "Observation of localized states in lieb photonic lattices," *Physical Review Letters*, vol. 114, no. 24, p. 245503, jun 2015.

List of publication

- Paper I

Moiré phonons in graphene/hexagonal boron nitride moiré superlattice

Lukas P. A. Krisna, and Mikito Koshino

Physical Review B **107**, 115301 (2023)

- Paper II

Low-temperature thermal transport in moiré superlattices

Lukas P. A. Krisna, Takuto Kawakami, and Mikito Koshino

arXiv preprint arXiv:2405.00406

This thesis is mainly based on the publication above.

Acknowledgments

First and foremost, I would like to express my heartfelt gratitude to my supervisor, Prof. Mikito Koshino, for his invaluable advice and unwavering support that goes beyond research, but also on life in general. His expertise and insights have been instrumental in shaping my works and bringing this thesis to fruition. I am truly honored to be one of his students and my time under his supervision is simply irreplaceable.

I would also like to thank the members of my thesis committee, Prof. Hajime Yoshino, Prof. Nayuta Takemori, Prof. Masayuki Ochi, and Prof. Takuto Kawakami, for their thoughtful feedback, constructive criticism, and for taking the time to review this thesis. In particular, I am especially appreciative of Prof. Takuto Kawakami for our productive discussions and for his generous assistance in both technical and non-technical aspects throughout my study.

I would also thank Prof. Young-Woo Son for his insight and guidance during my brief visit to his group. I also extend my thanks to Prof. Tomoki Machida and Prof. Rai Moriya for allowing me to have a hands-on experience in the fabrication of moiré materials in their laboratory. I gained valuable insight from an experimental point of view that is valuable for my research.

I would like to especially thank Dr. Naoto Nakatsuji, who has helped me in various aspects of both study and life since day one of my PhD journey. I also thank the group secretaries, Ms. Mari Homma, Ms. Yuki Harada and Ms. Miho Mitsuya for their support outside research and other endeavors. In particular, I am especially grateful to Ms. Mari Homma, who has also been a mother figure for me and has made sure that I have a comfortable life in Osaka. I am also thankful to Prof. Tadafumi Kishimoto, Prof. Kiyohiro Sugiayama for their role as a mentor and Ms. Mitsuyo Otsuka and Ms. Atsuko Miyajima for their role as secreatries in the Pioneering Quantum Beam Application (PQBA) Program.

I would like to acknowledge the funding and resources provided by the Next Generation Researcher Development Project and the PQBA Program that made

this research possible and for the opportunity to visit Korea Institute for Advanced Study and The Univeresity of Tokyo.

Finally, I would also like to express my deepest gratitude to my family and friends for their love, patience, and encouragement. To my parents, Ignatius Agus Aprijanto and Nuryamah, and to my sisters, Vincentia and Marta, thank you for your endless support and belief in me. To my partner, Fabiola Maria Teresa Retno Kinasih, thank you for your unwavering support, understanding, and standing by me through the highs and lows of this journey despite the distance that separates us. I am also grateful to Dr. Masaru Hitomi and other laboratory members and alumni who I could not mention one by one, for all the stories we shared and made together.